

CURRENT-PHASE RELATIONS OF JOSEPHSON JUNCTIONS WITH  
FERROMAGNETIC BARRIERS

BY

SERGEY MAKSIMOVICH FROLOV

B.S., Moscow Institute of Physics and Technology, 2000

DISSERTATION

Submitted in partial fulfillment of the requirements  
for the degree of Doctor of Philosophy in Physics  
in the Graduate College of the  
University of Illinois at Urbana-Champaign, 2005

Urbana, Illinois

CURRENT-PHASE RELATIONS OF JOSEPHSON JUNCTIONS WITH  
FERROMAGNETIC BARRIERS

Sergey Maksimovich Frolov, Ph.D.  
Department of Physics  
University of Illinois at Urbana-Champaign, 2005  
Dale J. Van Harlingen, Advisor

We have studied Superconductor-Ferromagnet-Superconductor (SFS) Nb-CuNi-Nb Josephson junctions that can transition between the 0 junction and the  $\pi$  junction states with temperature. By direct measurement of the current-phase relation (CPR) we have determined that the critical current of some SFS junctions changes sign as a function of temperature, indicating the  $\pi$  junction behavior. The CPR was determined by incorporating the junction into an rf SQUID geometry coupled to a dc SQUID magnetometer, allowing measurement of the junction phase difference. No evidence for the second-order Josephson tunneling, that was predicted by a number of theories to be observable near the  $0-\pi$  transition temperature, was found in the CPR. In non-uniform  $0-\pi$  SFS junctions with spatial variations in the effective barrier thickness, our data is consistent with spontaneous currents circulating around the  $0-\pi$  boundaries. These spontaneous currents give rise to Shapiro steps in the current-voltage characteristics at half-integer Josephson voltages when the rf-modulation is added to the bias current. The degree of  $0-\pi$  junction non-uniformity was determined from measurements of the critical current vs. applied magnetic flux patterns. Scanning SQUID Microscope imaging of superconducting arrays with SFS junctions revealed spontaneous currents circulating in the arrays in the  $\pi$  junction state below the  $0-\pi$  transition temperature.

# Acknowledgements

I would like to thank Professor Dale Van Harlingen for teaching me everything I know about experimental physics, for introducing me to the fascinating science of superconducting devices and for guiding me through my graduate studies. Dale is an outstanding scientist and mentor, and a wonderful person. Professor Valery Ryazanov was my undergraduate advisor and later became an invaluable collaborator in my graduate work. I thank him for his trust and support, for his expertise and intuition, and for good times in Chernogolovka and Urbana.

I am grateful to the members of the DVH group Kevin Osborn, Joe Hilliard, Martin Stehno, Micah Stoutimore, Madalina Colci, David Caplan, Willie Ong, Francoise Kidwingira, Dan Bahr and Adele Ruosi. I would like to especially thank William Neils a.k.a. “physicist formerly known as Bill”, Tony Bonetti and Trevis Crane for their patience in training me and helping me with some of the world’s most ridiculous experimental problems. I also thank students from the Institute of Solid State Physics in Chernogolovka Alexey Feofanov and Vitaliy Bolginov who I collaborated with in studying SFS Josephson junctions.

It is difficult to appreciate enough the contribution of Vladimir Oboznov, a technology expert who fabricated the state-of-the-art samples that allowed us to perform many novel and important experiments on SFS junctions. In Urbana, we are lucky to have Tony Banks as a supervisor of the microfabrication facility and a walking

encyclopedia on fabrication technology.

I thank some of the teachers whom I was fortunate to learn from in the classroom: Mrs. A.V. Gluschenko, Mr. S.V. Sokirko, Mrs. L. Tarasova, Mrs. T.A. Fedulkina, Mrs. N.E. Talaeva, Mrs. O.N. Soboleva, Mrs. T.M. Solomasova, Mrs. V.I. Zhurina, Mrs. M.A. Ismailova, Mrs. V. P. Saliy, Mrs. N.A. Babich, Ms. E.Yu. Kassidi, Mrs. Y.V. Lyamina, Dr. N.G. Chernaya, Dr. T.V. Klochkova, Dr. V.T. Rykov, Dr. N.H. Agakhanov, Dr. V.V. Mozhaev, Dr. A.S. Dyakov, Professor G.N. Yakovlev, Dr. G.V. Kolmakov, Dr. N.M. Trukhan, Professor F.F. Kamenets, Professor Yu.V. Sidorov, Dr. E.V. Voronov, Dr. S.N. Burmistrov, Dr. M.R. Trunin, Dr. V.N. Zverev, and Professor A.J. Leggett.

My family played a crucial role by stimulating me to learn, work and go forward. For that I thank my wife Olya, my parents Nina and Maksim, my grandparents Irina, Roma, Mikhail and Tasya, and my great-grandparents Tatyana and Vladimir.

I was doing my first current-phase relation measurements in the Summer of 2003 feeling that my thesis was going to be an exercise with a predetermined answer. Then came the Spring of 2004, when the group in Chernogolovka discovered another  $0-\pi$  transition at smaller barrier thicknesses, and the group from Grenoble reported half-integer Shapiro steps in SFS junctions. These experiments literally turned the picture upside down, brought back the question of second-order Josephson tunneling and allowed us to explore the beautiful physics of  $0-\pi$  junctions. I therefore feel justified to thank nature for being more complex than we anticipated, and for willing to play our game even after centuries of interrogation.

This work was supported by the National Science Foundation grant EIA-01-21568, the U.S. Civilian Research and Development Foundation grant RP1-2413-CG-02. We also acknowledge extensive use of the Microfabrication Facility of the Frederick Seitz Materials Research Laboratory at the University of Illinois at Urbana-Champaign.

# Table of Contents

<b>Chapter 1</b>	<b>Josephson Current-Phase Relation.....</b>	<b>1</b>
1.1	The Josephson effects . . . . .	1
1.2	Negative critical currents - $\pi$ junctions . . . . .	7
1.3	Non-sinusoidal current-phase relations . . . . .	16
<b>Chapter 2</b>	<b><math>\pi</math> Junctions in Multiply-Connected Geometries.....</b>	<b>21</b>
2.1	$\pi$ junction in an rf SQUID . . . . .	21
2.2	$\pi$ junction in a dc SQUID . . . . .	27
2.3	Arrays of $\pi$ junctions . . . . .	33
<b>Chapter 3</b>	<b>Proximity Effect in Ferromagnets.....</b>	<b>38</b>
3.1	Order parameter oscillations in a ferromagnet . . . . .	38
3.2	SFS Josephson junctions . . . . .	44
<b>Chapter 4</b>	<b>Fabrication and Characterization of SFS Junctions.....</b>	<b>50</b>
4.1	Magnetism of CuNi thin films . . . . .	50
4.2	Fabrication procedures . . . . .	54
4.3	Transport measurements procedure . . . . .	58
4.4	Critical current vs. barrier thickness . . . . .	61
4.5	Critical current vs. temperature . . . . .	64
<b>Chapter 5</b>	<b>Phase-Sensitive Experiments on Uniform SFS Junctions .</b>	<b>69</b>
5.1	Measurement technique . . . . .	71
5.2	Current-phase relation data and analysis . . . . .	79
5.3	Effects of residual magnetic field . . . . .	84
<b>Chapter 6</b>	<b>Experiments on Non-Uniform SFS <math>0-\pi</math> Junctions.....</b>	<b>89</b>
6.1	Diffraction patterns of $0-\pi$ junctions . . . . .	89
6.2	Spontaneous currents in $0-\pi$ junctions . . . . .	101
6.3	Half-integer Shapiro steps in $0-\pi$ junctions . . . . .	108
<b>Chapter 7</b>	<b>Search for <math>\sin(2\phi)</math> Current-Phase Relation.....</b>	<b>114</b>

<b>Chapter 8 Experiments on Arrays of SFS Junctions</b> .....	<b>120</b>
8.1 Imaging arrays with a scanning SQUID microscope .....	121
8.2 Spontaneous currents in SFS $\pi$ junction arrays .....	127
<b>References</b> .....	<b>136</b>
<b>Author's Biography</b> .....	<b>142</b>

# CURRENT-PHASE RELATIONS OF JOSEPHSON JUNCTIONS WITH FERROMAGNETIC BARRIERS

Sergey Maksimovich Frolov, Ph.D.

Department of Physics

University of Illinois at Urbana-Champaign, 2005

Dale J. Van Harlingen, Advisor

We have studied Superconductor-Ferromagnet-Superconductor (SFS) Nb-CuNi-Nb Josephson junctions that can transition between the 0 junction and the  $\pi$  junction states with temperature. By direct measurement of the current-phase relation (CPR) we have determined that the critical current of some SFS junctions changes sign as a function of temperature, indicating the  $\pi$  junction behavior. The CPR was determined by incorporating the junction into an rf SQUID geometry coupled to a dc SQUID magnetometer, allowing measurement of the junction phase difference. No evidence for the second-order Josephson tunneling, that was predicted by a number of theories to be observable near the 0- $\pi$  transition temperature, was found in the CPR. In non-uniform 0- $\pi$  SFS junctions with spatial variations in the effective barrier thickness, our data is consistent with spontaneous currents circulating around the 0- $\pi$  boundaries. These spontaneous currents give rise to Shapiro steps in the current-voltage characteristics at half-integer Josephson voltages when the rf-modulation is added to the bias current. The degree of 0- $\pi$  junction non-uniformity was determined from measurements of the critical current vs. applied magnetic flux patterns. Scanning SQUID Microscope imaging of superconducting arrays with SFS junctions revealed spontaneous currents circulating in the arrays in the  $\pi$  junction state below the 0- $\pi$  transition temperature.

# Chapter 1

## Josephson Current-Phase Relation

### 1.1 The Josephson effects

The superconducting state of matter was originally identified through the total loss of electrical resistance by certain metals (Hg, Pb, Nb, Al) cooled to sufficiently low temperatures ( $\sim 1 - 10$  K) [1]. The analogy can be drawn to the frictionless flow of liquid, the phenomenon known as the superfluidity. In  ${}^4\text{He}$ , below the “lambda temperature”, which is approximately 2.17 K at the atmospheric pressure, the Bose-Einstein condensation takes place: an anomalously large number of molecules occupy the ground state and do not participate in the energy exchange with the environment. The difference from the case of metals is that helium liquid consists of diatomic molecules, which are bosons, but the electrical current in metals is created by electrons, which are fermions. Fermions cannot undergo the Bose-Einstein condensation due to the Pauli exclusion principle. Instead, at zero temperature electrons occupy all available states up to the Fermi energy, which is determined by the density of conduction electrons.

However, two electrons in a metal can couple via a mechanism known as the

Cooper pairing. An electron moving through a lattice of ions creates vibrations (phonons), which can be absorbed by another electron. The interaction that arises as a result can be attractive provided the electron-phonon coupling is strong enough. Cooper pairs are bosons, they may form a condensate that possesses the property of superconductivity. The total energy of the condensate is minimized if electrons in the states with opposite momentum  $\mathbf{k}$  pair:  $(\mathbf{k}, -\mathbf{k})$ . The pairing state can be spin singlet or spin triplet.

The microscopic mechanism of superconductivity was described by the Bardeen-Cooper-Schrieffer (BCS) theory [2]. Besides the BCS theory, there exist several theories that illuminate various aspects of superconductivity: the electrodynamic properties of superconductors are well described by the London theory [3], and the Ginzburg-Landau (GL) theory deals with thermodynamics, effects of geometry and many other problems on a phenomenological level [4]. Here, we shall only discuss the notion of a macroscopic superconducting wavefunction, which is a useful concept for illustrating the Josephson effect.

Cooper pairing leads to a non-zero correlator between the wavefunctions of electrons in the states with opposite momentum. For the case of singlet pairing, this correlator is  $\langle \Psi_{\downarrow}(\mathbf{k})\Psi_{\uparrow}(-\mathbf{k}) \rangle$ . Because the wavefunctions of many Cooper pairs overlap (the typical coherence length  $\xi_0 \sim 10^{-8} - 10^{-6}$  m), it is possible to integrate the Cooper pair correlator over all Cooper pair states to get a macroscopic wavefunction, also called the superconducting order parameter:

$$\Psi(\mathbf{r}) = \Psi_0(\mathbf{r})e^{i\varphi(\mathbf{r})}. \quad (1.1)$$

In general, the order parameter also depends on  $\mathbf{k}$ , as is the case in high- $T_c$  cuprates, certain heavy-fermion and organic materials. The order parameter indeed behaves in many ways like the macroscopic wavefunction of the condensate. For exam-

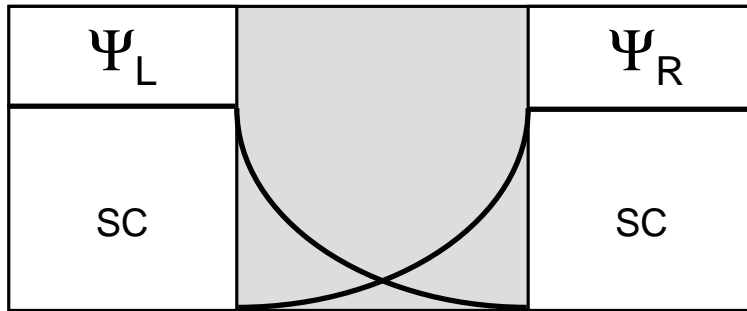


**Figure 1.1:** Two superconductors with wavefunctions  $\Psi_L$  and  $\Psi_R$  are placed in the vicinity of each other, so that the evanescent tails of the wavefunctions overlap.

ple, the order parameter satisfies the conditions of continuity and single-valuedness.

In the bulk of a superconductor, the amplitude of the order parameter  $\Psi_0$  is a constant determined by the density of states. It can also vary if material is inhomogeneous or if magnetic fields are present. The phase of the order parameter  $\varphi$  is a gauge covariant quantity, therefore it can have an arbitrary value in a given piece of superconductor. However, gradients in phase are observable, because they give rise to currents or to non-zero circulation of the vector potential around a closed path (magnetic flux).

If a finite phase difference  $\phi$  is somehow maintained between the two closely spaced but spatially separated pieces of superconductor, a supercurrent may flow between them. By supercurrent we mean the current that does not produce dissipation, i.e. flows without resistance. This effect was derived by Josephson from the BCS theory. Even though only single electron tunneling is taken into account in the calculation, the supercurrent can be intuitively understood in terms of the Cooper pair tunneling through a barrier separating one superconductor from the other. If the tunneling barrier is not too high, the wavefunction of the superconductor on the left overlaps with the wavefunction of the superconductor on the right [5], as shown in Figure 1.1.

If the coupling between the two superconductors affects their states, the supercon-

ductors are considered *strongly linked*. Examples of strong links are superconductors connected by a wide superconducting bridge, or separated by a thin tunneling barrier. If the wavefunctions of the superconductors are unperturbed by the tunneling barrier, the superconductors are considered *weakly linked*. If the phase in one of the superconductors is rotated by  $2\pi$ , the physical state of the weak link, and hence the supercurrent, should not change. In other words, the dependence of the supercurrent on the phase difference between the superconductors must be periodic with a period of  $2\pi/n$ . In contrast, if the two superconductors are strongly linked, winding of phase in one of them by  $2\pi$  leads to an increase in supercurrent [6].

The flow of supercurrent through a weak link is called the *dc Josephson effect* [7]. Each weak link is characterized by its current-phase relation (CPR):

$$I_s = CPR(\phi), \quad (1.2)$$

where  $I_s$  is the supercurrent and  $\phi$  is the phase difference between the two superconductors. In this Chapter we only consider weak links with uniform tunneling barriers. The most general conditions that the CPR must satisfy regardless of the weak link geometry and material properties are the following [8]:

1. As was already discussed, because the weak link returns to the same physical state if  $\phi$  is changed by  $2\pi$ , the CPR must be a periodic function with a period of  $2\pi/n$ :

$$CPR(\phi) = CPR(\phi + 2\pi). \quad (1.3)$$

2. Supercurrent is an odd function of the phase difference. In the absence of factors that break time-reversal symmetry, a change in the sign of the phase difference should lead to a change in the direction of supercurrent:

$$CPR(-\phi) = -CPR(\phi). \quad (1.4)$$

3. If the phase difference between the two superconductors is zero, no supercurrent should flow:

$$CPR(0) = CPR(2\pi n) = 0. \quad (1.5)$$

4. From 1 and 2 it follows that the supercurrent must also be zero for a phase difference of  $\pi$ :

$$CPR(\pi) = CPR(\pi n) = 0. \quad (1.6)$$

In his original calculation, Josephson demonstrated that the CPR of a tunneling junction has a simple sinusoidal form:

$$I_s(\phi) = I_c \sin(\phi). \quad (1.7)$$

The coefficient  $I_c$  is the critical current. It corresponds to a maximum supercurrent that can flow through a weak link, and is reached at  $\phi = \pi/2$  for the CPR given by the Equation (1.7). The critical currents of weak links are typically much lower than the critical currents of bulk superconductors. The sinusoidal CPR is very common and as far as experiments can tell holds rather well not only for tunnel junctions, but also for Superconductor-Normal metal-Superconductor (SNS) junctions. However, there are no *a priori* reasons why the CPR should be sinusoidal. In general, the CPR can be described by a series:

$$I_s(\phi) = \sum_{n=1}^{\infty} I_c^n \sin(n\phi). \quad (1.8)$$

If the CPR has higher harmonics with  $n > 1$ , the critical current is not necessarily reached at  $\phi = \pi/2$ . The coefficients  $I_c^n$  are not related to the critical current in a straightforward way, they only have the meaning of the amplitudes of various harmonics in the CPR. Special situations for which deviations of the CPR from the sinusoidal form have been predicted or observed will be discussed later in this Chapter.

If a phase difference across the Josephson junction changes with time, a voltage is developed between the two superconductors. This phenomenon is called the *ac Josephson effect* [7]. Experimentally, a state with time-dependent phase can be created by either passing a current exceeding the critical current through a junction, or by applying an ac current to a junction. The ac Josephson effect can also be motivated by simple quantum mechanical considerations. The voltage  $V$  across the junction corresponds to the energy difference of  $2eV$  between the Cooper pairs in the weakly linked superconductors. It then follows from the time-dependent perturbation theory that the overlap term of the wavefunction is of the form:

$$\Psi^T(\phi(t)) = \Psi^T(\phi(0)) e^{-i\frac{2eV}{\hbar}t}, \quad (1.9)$$

from which follows the second Josephson equation for the rate of change of the Josephson phase difference:

$$\frac{d\phi}{dt} = \frac{2eV}{\hbar}. \quad (1.10)$$

At this point we can calculate the energy of a weak link at a phase difference  $\phi$ . Suppose that initially the weak link is at a phase difference  $\phi = 0$ . The work done by an external battery in order to bring the phase difference to a finite value  $\phi$  in time  $T$  is:

$$E(\phi) = \int_0^T IV dt = \int_0^T I_c \sin \phi \frac{\hbar}{2e} \frac{d\phi}{dt} dt = \frac{\hbar I_c}{2e} (1 - \cos \phi), \quad (1.11)$$

or, in terms of the Josephson energy  $E_J = \hbar I_c / 2e$ :

$$E(\phi) = E_J (1 - \cos \phi). \quad (1.12)$$

## 1.2 Negative critical currents - $\pi$ junctions

An interesting case of a current-phase relation is a sinusoidal dependence with a negative critical current:

$$I_s(\phi) = -I_c \sin(\phi) = |I_c| \sin(\phi + \pi). \quad (1.13)$$

The sign of the critical current is an indicator of the direction in which the supercurrent flows if a small ( $< \pi$ ) and positive phase difference is applied to the junction. The definition of the critical current given earlier can thus be expanded to include its sign. If  $I_c < 0$ , the supercurrent is opposite to the direction of the phase gradient across the junction for small phase gradients.

Junctions with the CPR given by the Equation (1.13) were first proposed theoretically by Bulaevskii, Kuzii and Sobyenin [9]. They considered a tunnel junction with magnetic impurities in the barrier. Electrons may tunnel through magnetic impurities without the conservation of spin. If the spin of an electron coincides with the spin of an impurity that it tunnels through, an electron may be forced to flip its spin by the Pauli exclusion principle. A perturbation theory calculation by Kulik [10] demonstrated that if the spin-flip tunneling is taken into account, the current-phase relation is given by:

$$I_s(\phi) = \frac{\pi \Delta}{2 R_N} \frac{\langle |T_N|^2 \rangle - \langle |T_{SF}|^2 \rangle}{\langle |T_N|^2 \rangle + \langle |T_{SF}|^2 \rangle} \sin \phi, \quad (1.14)$$

where  $\Delta$  is the gap parameter,  $R_N$  is the normal state resistance of the junction,  $T_N$  is the matrix element of the tunneling processes that conserve spin and  $T_{SF}$  is the matrix element of the spin-flip electron tunneling. If  $T_{SF} = 0$ , the Equation (1.14) reduces to the Ambegaokar-Baratoff CPR:  $I_s = (\pi\Delta)/(2R_N) \sin \phi$  [11]. As can be seen from (1.14), spin flip tunneling has a negative contribution to the critical current. In order to conserve parity, the amplitude of the order parameter must be inverted if the spin

of one of the electrons is flipped. If spin-flip tunneling could be made dominant over the spin-conserving tunneling, so that  $T_{SF} > T_N$ , the supercurrent of the junction would become negative. In practice, the observation of negative critical currents due to spin flip tunneling is complicated because scattering from magnetic impurities causes the loss of coherence in Cooper pairs [12], leading to a strong suppression of the Josephson effect. Due to this, negative currents in Josephson junctions with magnetic impurities in the barriers have not been achieved.

It may be possible to create a negative critical current junction based on the spin-flip tunneling through a quantum dot (S-dot-S junctions) [13; 14]. The spin-flip tunneling is predicted to dominate the Josephson current when the spin on the quantum dot is non-zero (Figure 1.2). In S-dot-S junctions, changes in the sign of the critical current could be observed as a function of the quantum dot gate voltage, which controls the occupancy of a quantum dot. Due to this gating capability, one has more control over the magnetic state of the barrier in a S-dot-S junction compared to a magnetically doped SIS junction. However, the magnitude of the Josephson current is small in S-dot-S structures due to a small number of available tunneling channels. In addition, a low superconductor/quantum dot interface resistance is desired in order to yield measurable supercurrents.

Another way to achieve negative critical currents is to use a ferromagnetic material for the Josephson junction barriers [15]. The exchange interaction lifts the degeneracy of electron energies in spin singlet Cooper pairs. Cooper pairs can compensate the depairing effect of the exchange energy by adjusting the kinetic energies of electrons. As a result, Cooper pairs acquire a non-zero center-of-mass momentum, which means that the order parameter becomes a plane wave with momentum and oscillates in space. This state is similar to the state proposed by Larkin and Ovchinnikov [16] and by Fulde and Ferrel [17] (LOFF state) for bulk superconductors with uniform

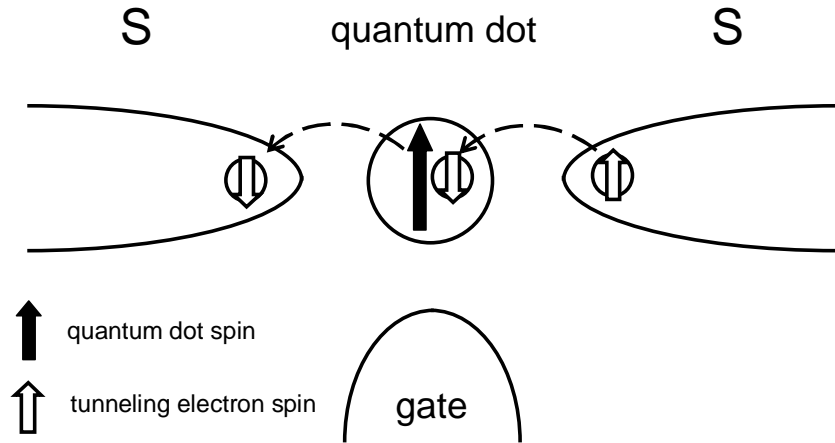


**Figure 1.2:** Electron tunneling between the two superconductors through a quantum dot. The spin induced on a quantum dot from the gate causes the tunneling electron to flip its spin.

exchange interaction.

In Superconductor-Ferromagnet-Superconductor (SFS) junctions with barrier thicknesses around  $1/2$  of the order parameter oscillation period, the amplitudes of the order parameter are opposite in the junction electrodes, which corresponds to a negative critical current. Experiments done in Chernogolovka demonstrated this effect for the first time [18]. Josephson junctions with ferromagnetic barriers are studied in the present thesis, and will be discussed in detail in subsequent Chapters.

In mesoscopic SNS junctions the sign of the critical current can be switched by creating a non-equilibrium distribution of electrons in the barrier [20]. In superconductors the energy gap  $\Delta$  is developed around the Fermi surface for single electron excitations (quasiparticles). The normal barrier of an SNS junction can be viewed as a potential well for single electrons, since  $\Delta = 0$  in the normal metal. Electrons in the barrier form bound states with discrete energies. The supercurrent can flow between the superconductors by means of electrons in these quantized levels due to a process known as the Andreev reflection [21]. When  $\phi = 0$  levels that carry opposite current are degenerate. At  $\phi \neq 0$  the degeneracy is lifted. Levels with critical

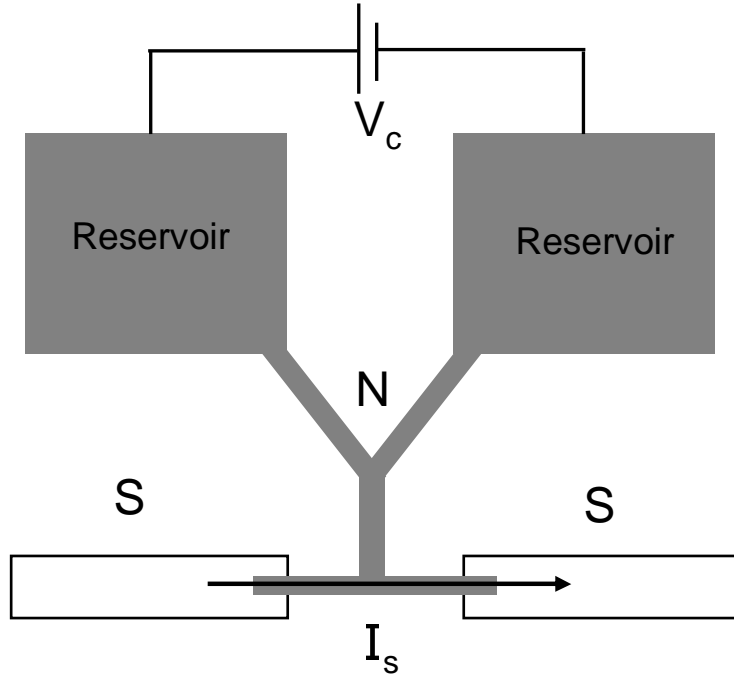


**Figure 1.3:** Mesoscopic SNS junction with a control channel.

currents of alternating signs are adjacent in energy, with the lowest level typically carrying the positive critical current, unless exotic factors like exchange interaction or unconventional Cooper pairing are present. In an SNS junction with a control channel shown in Figure 1.3, a non-equilibrium distribution of electrons can be created in the barrier. By applying voltage to the control channel, the Fermi level in the barrier can be made higher than the lowest Andreev level (see Figure 1.4). Single electron excitations will then occupy the second Andreev level, switching the sign of the critical current [22; 23]. The normal material needs to be clean enough to reduce electron recombination into the equilibrium distribution. Hybrid devices that involve mesoscopic SFS junctions with voltage controlled barriers were also proposed [24]. In these systems, the modulation of the Josephson effect due to the ferromagnetic exchange interaction is combined with the ability to manipulate the population of Andreev levels by voltage in order to achieve additional control over the critical current.

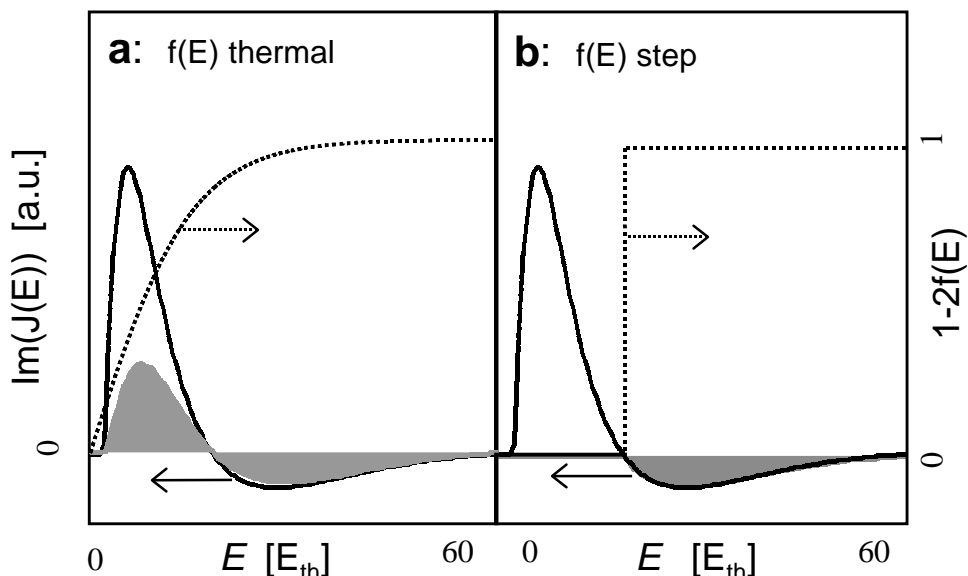


**Figure 1.4:** Supercurrent spectrum  $J(E)$  of a mesoscopic SNS junction and non-equilibrium occupation  $f(E)$  created by the control voltage at finite temperature (panel (a)) and at zero temperature (panel (b)). Energy is given in the units of Thouless energy  $E_{th} = \hbar D/d^2$ , where  $d$  is the thickness of the barrier, and  $D$  is the diffusion constant. Adapted from [19].

So far we discussed how barrier properties can influence the sign of the critical current. It is also possible to make a junction with negative critical current if the superconductor electrodes have unconventional d-wave order parameter symmetry. In high temperature superconductors [25] the order parameter is not isotropic, it depends on the momentum of electrons  $\mathbf{k}$  in the following way:

$$\Delta(k_x, k_y) = \Delta_0(\cos k_x a - \cos k_y a), \quad (1.15)$$

where  $a$  is the lattice constant. The order parameter described by the Equation (1.15) is shown in Figure 1.5. The OP does not depend on  $k_z$  due to the cylindrical symmetry of the Fermi surface in these materials. For more information on the order parameter symmetry in high-temperature superconductors see Van Harlingen [26] and Tsuei and Kirtley [27].

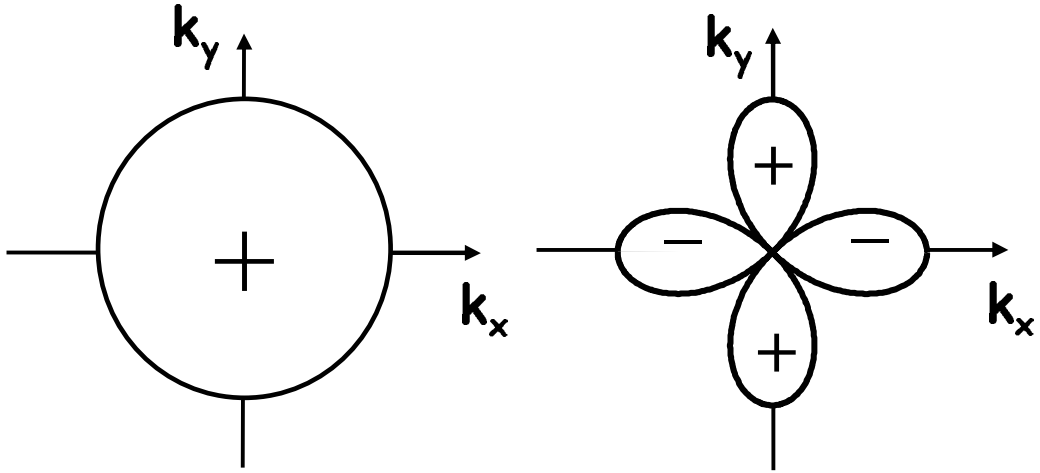


**Figure 1.5:** isotropic s-wave and anisotropic d-wave order parameters in k-space.

We shall now consider a symmetric grain boundary d-wave - d-wave Josephson junction with the crystal axes rotated against each other in the superconducting banks of the junction (see Figure 1.6). At certain misorientation angles  $\alpha$  of the crystal axes, Andreev bound states of zero energy carrying negative supercurrents can be formed due to a sign mismatch of the order parameters in the junction electrodes [28; 29]. Negative critical currents were claimed in a number of experiments [30; 31], but the conditions for obtaining negative critical current junctions consistently are not clear at the present time. Josephson junctions with rotated order parameters are fabricated on bicrystal substrates. High-temperature superconductors form grain boundary tunneling barriers along the crystal mismatch lines [32]. Such grain boundary Josephson junctions are highly faceted (see Figure 1.6), which results in a spread in the preferred tunneling directions along the junctions. Because negative supercurrent bound states are supposed to be the lowest energy only in certain ranges of the order parameter misorientation angles  $\alpha$ , small (submicron) grain-boundary junctions with only a few facets should exhibit negative critical currents with higher, but still finite, probability.

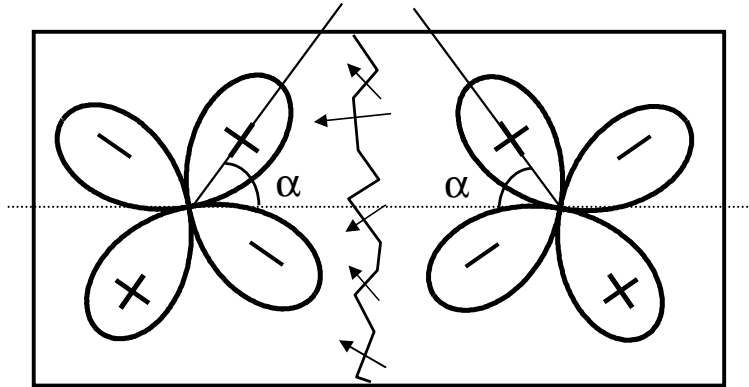


**Figure 1.6:** A grain boundary d-wave - d-wave junction. Order parameters are symmetrically rotated by an angle  $\alpha$ . The grain boundary is faceted.

The energy of a Josephson junction with a CPR (1.13) is

$$E(\phi) = |E_J|(1 + \cos \phi) = |E_J|(1 - \cos(\phi + \pi)). \quad (1.16)$$

The energy minimum is reached at the phase-difference of  $\pi$ . Owing to this property, junctions with negative critical currents were named  $\pi$  junctions [9]. Figure 1.7 explains the difference in the CPR and in the Josephson energy-phase relation between a  $\pi$  junction and a conventional 0 junction. Now suppose that the electrodes of a  $\pi$  junction are shorted together to form a superconducting loop of geometric inductance  $L$ . In the absence of externally applied magnetic flux, a  $\pi$  junction cannot be in the state with  $\phi = \pi$ , because the phase change around the loop should be equal to  $2\pi n$ . It will be shown in Chapter 2 that if  $2\pi I_c L > \Phi_0$ , where  $\Phi_0 = h/2e$  is the quantum of magnetic flux in superconductors, the state with  $\phi = 0$  across the junction is not the lowest energy state. Any other phase difference corresponds to a supercurrent through the junction and around the loop. If  $2\pi I_c L < \Phi_0$ , the phase difference across the  $\pi$  junction is zero, because it costs more energy to generate a current in the loop than to keep the  $\pi$  junction in its highest energy state with  $\phi = 0$ .

In the original paper [9]  $\pi$  junction was defined as a junction with a phase difference  $\phi = \pi$  in the ground state. According to such definition, SNS junctions with

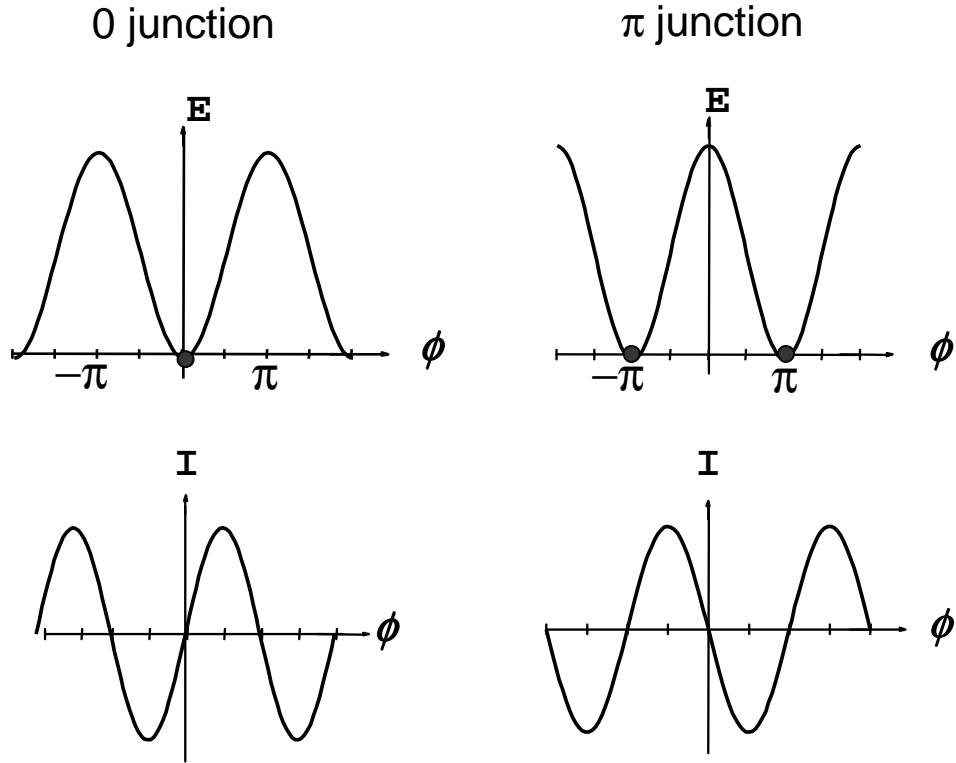


**Figure 1.7:** Difference in the CPR and in the Josephson energy-phase relation between a  $\pi$  junction and a conventional 0 junction. The  $\pi$  junction energy has a minimum at  $\phi = \pi$ .

controllable barriers [22] described above are not  $\pi$  junctions, because the sign of the critical current in their case is switched by creating a non-equilibrium distribution of electrons, i.e. negative critical currents are not the ground state property of these devices. Nevertheless, controllable SNS junctions do have negative critical currents, and do behave like  $\pi$  junctions in many experiments [33]. We shall therefore define a  $\pi$  junction more generally as a Josephson junction with a negative critical current.

A number of devices also behave like  $\pi$  junctions in certain experiments, but are not  $\pi$  junctions, because their critical currents are not negative and their lowest energy states are not at  $\phi = \pi$ . One noteworthy example is a superconducting loop that incorporates a corner of a crystal with the d-wave symmetry of the order parameter [34], shown in Figure 1.8. This loop contains two junctions fabricated on two

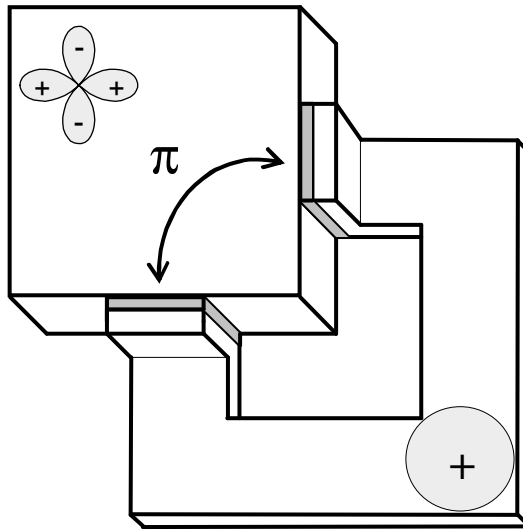


**Figure 1.8:** A two junction loop containing a corner of a superconducting crystal with the d-wave order parameter symmetry. Along the closed path in the loop, a phase shift of  $\pi$  occurs in the d-wave crystal.

orthogonal faces of the d-wave crystal shorted by a superconductor of conventional isotropic order parameter symmetry. Due to a phase shift of  $\pi$  between the preferred directions of tunneling into a d-wave crystal in the two Josephson junctions, spontaneous currents circulate in this loop much like in a  $\pi$  junction loop. However, both junctions in the d-wave corner loop are the usual 0-Josephson junctions with positive critical currents and the CPR of the form (1.7). If the loop inductance is small, generation of spontaneous currents costs too much energy. In that case, in order to satisfy the fluxoid quantization condition, one of the junctions prefers to maintain a phase difference  $\phi = \pi$  as opposed to being in its' ground state with  $\phi = 0$ .

Josephson effects were also observed in weak links formed by the superfluid  $^3\text{He}$  [35]. Two containers with superfluid  $^3\text{He}$  were connected by an array of nanoscale constrictions through which a superfluid could flow. Superfluid condensates in separate reservoirs had definite phases, in which case a weak link between the two superfluids could be characterized by a superfluid current-phase relation [36]. A metastable

state with a phase difference  $\phi = \pi$  between the two reservoirs was reported [37; 38]. However, the state with  $\phi = 0$  was still a local minimum. For this reason this system also cannot be called a  $\pi$  junction, in which the energy has a maximum at  $\phi = 0$  (see Figure 1.7). A metastable state with  $\phi = \pi$  could be an indication of higher harmonics in the CPR [35; 39].

### 1.3 Non-sinusoidal current-phase relations

It turns out that the sinusoidal CPR (1.7) is the most common in nature, it accurately describes Josephson junctions made from many different materials using a wide range of fabrication technologies. Naturally, the question of when this simple dependence breaks down has received a lot of attention. Most of the work has been theoretical, since experimentally it is difficult both to prepare a junction with a non-sinusoidal CPR and to measure CPR with enough precision. Thorough reviews of weak links with predicted non-sinusoidal current-phase relations were performed by Likharev [8] and more recently by Golubov et al. [40]. We shall discuss only a few typical reasons for the deviations from a sinusoidal CPR.

Sinusoidal CPR is expected to hold exactly for SIS tunnel junctions [7; 40]. In other Josephson structures, like SNS junctions, point contacts and microbridges, energy spectrum of the electrons in the barrier, spatial distributions of the order parameter, effects of the junction geometry etc. influence the shape of the CPR, sometimes changing the CPR period, or shifting the maximal supercurrent from  $\phi_{max} = \pi/2$ , or even making the CPR a multivalued function. Typically, in dirty and wide junctions, in junctions with spatially inhomogeneous barriers, and close to  $T_c$  of the superconductor, where energy levels are broadened, the CPR is still sinusoidal, because the peculiarities associated with a specific barrier type are averaged out.

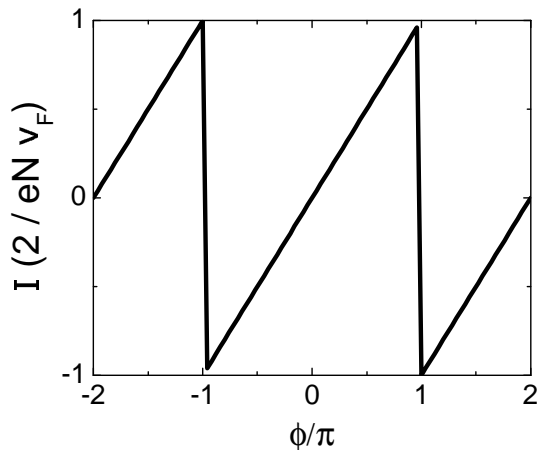


**Figure 1.9:** Current-phase relation of an SNS junction in the clean limit at zero temperature has a saw-tooth shape.

In uniform clean SNS junctions ( $l \gg \xi_0, \xi_N, d$ ) at low temperatures  $T \ll T_c$ , the energies of the subgap Andreev levels ( $E_n \ll \Delta$ ) depend linearly on the phase difference across the junction [41]:

$$E_n = \frac{\hbar v_F}{d} \pi \left( n + \frac{1}{2} - \frac{\phi}{2} \right). \quad (1.17)$$

In junctions with thick enough barriers ( $\xi_N \ll d \ll \xi_0$ , where  $\xi_N$  and  $\xi_0$  are the normal metal and the superconductor coherence lengths), summed over all energy levels, this energy-phase relation results in a “saw-tooth” shaped current-phase relation. The current-phase relation for the case when only tunneling normal to the SN interface is allowed is given by [42; 43]:

$$I_s(\phi) = eNv_F \frac{\phi}{2}. \quad (1.18)$$

This dependence is valid for  $-\pi < \phi < \pi$ , outside this interval the CPR is repeated periodically. In the Equation (1.18),  $N$  is the number of conducting channels defined by how many Fermi wavelengths can fit in the junction width,  $v_F$  is the Fermi velocity. The saw-tooth CPR is presented in Figure 1.9.

In point contacts, large supercurrents flow through a small area, typically smaller than the mean free path  $l$ . The CPR at arbitrary temperature and for arbitrary barrier transparency of a point contact with a single conduction channel is given by [44]:

$$I_s(\phi) = \frac{\pi\Delta}{2eR_N} \frac{\sin(\phi)}{\sqrt{1 - \bar{D}\sin^2\frac{\phi}{2}}} \times \tanh\left[\frac{\Delta}{2T}\sqrt{1 - \bar{D}\sin^2\frac{\phi}{2}}\right], \quad (1.19)$$

where  $R_N$  is the resistance of a point contact in the normal state,  $\bar{D}$  is the point contact transmission probability averaged over tunneling angles. If  $\bar{D} \ll 1$  or at temperatures close to  $T_c$ , the CPR given by (1.19) is sinusoidal. At low temperatures and in clean junctions with  $\bar{D} \sim 1$ , the CPR is half periodic:  $I_s(\phi) \propto \sin(\phi/2)$ . Generally, at  $\bar{D} > 0$  or at  $T < T_c$  the Equation (1.19) yields a CPR in which a maximal supercurrent corresponds to a phase difference  $\phi_{max} > \pi/2$  (Figure 1.10). Deviations from sinusoidal CPR were reported in point contacts [45], and in atomic-size controllable quantum point contacts [46].

Universal to SIS, SNS and SS'S junctions and microbridges are the effects of depairing by supercurrent. Depairing effects occur in structures with high current concentration due to sample geometry, barrier transparency or other factors. Large supercurrents may lead to a suppression of superconductivity in the barrier or in the superconducting electrodes of a junction. For small values of  $\phi$ , which correspond to small supercurrents  $I \ll I_c$ , the superconductivity is weakly suppressed in the barrier. The CPR follows the dependence calculated without taking the depairing effects into account. At higher phase differences, larger currents flow through the junction, the CPR becomes affected by the depairing. The critical current as well as the phase difference  $\phi_{max}$  at which the critical current is reached are decreased. If the CPR was supposed to be sinusoidal before taking depairing into account,  $\phi_{max}$  will become less than  $\pi/2$  due to depairing. However, in point contacts described by the Equation

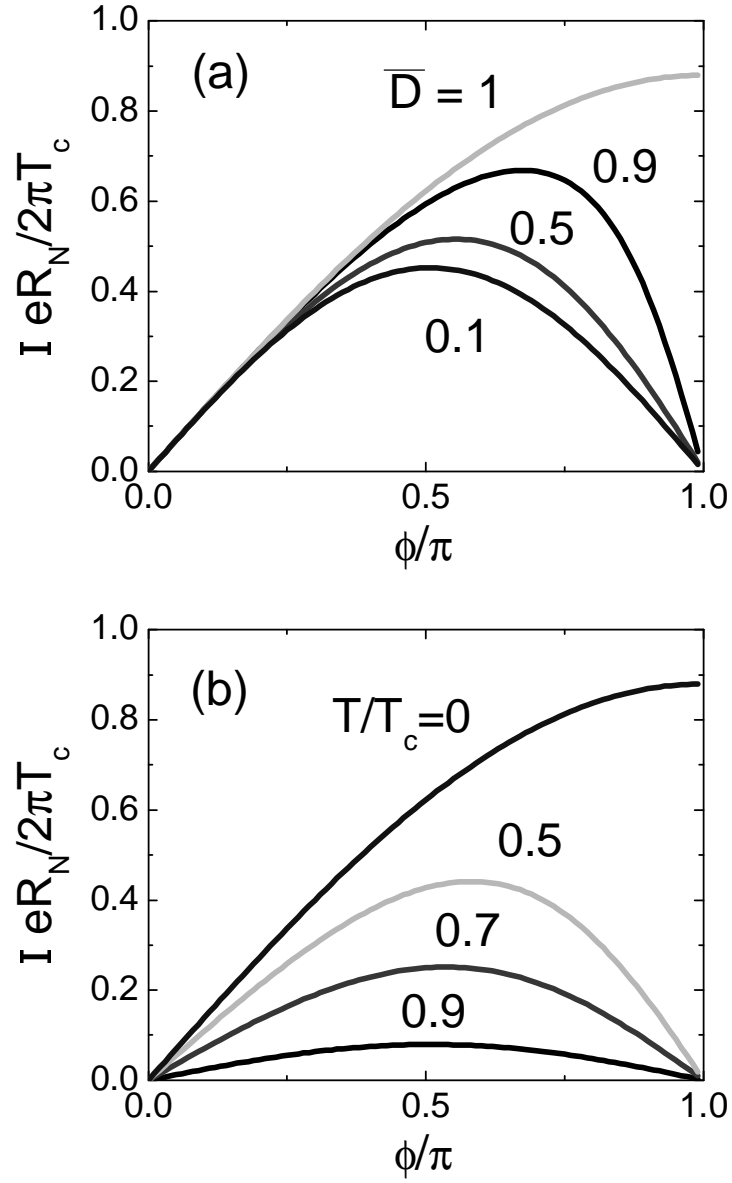


**Figure 1.10:** Current-phase relation of a point contact calculated using the equation (1.19) (a) for various barrier transmission parameters  $\bar{D}$ , and (b) for various temperatures.

(1.19), the CPR may actually become more sinusoidal due to depairing effects [47].

Josephson tunneling of the second order in perturbation theory contributes a half-periodic phase term to the Josephson energy of the junction, and may result in a CPR proportional to  $\sin(2\phi)$ . Physically, the second order tunneling corresponds to the tunneling of two Cooper pairs simultaneously. This effect is typically much smaller than the regular first order Josephson tunneling. However, in SNS and SFS  $\pi$  junctions first order terms cancel at the transition between 0 and  $\pi$  states [18; 22]. A number of theories propose that a second-order component in the CPR can be observed in these systems close to a 0- $\pi$  transition [24; 39; 48–54]. We summarize the work done towards the observation of the  $\sin(2\phi)$  current-phase relation close to 0- $\pi$  transitions in Chapter 7.

# Chapter 2

## $\pi$ Junctions in Multiply-Connected Geometries

In order to measure the current-phase relation, a Josephson junction should be placed in a superconducting loop. Flux quantization in superconducting loops provides a way to measure the phase difference across the junction by monitoring the flux induced in the loop. If a  $\pi$  junction is placed in a superconducting loop, a supercurrent may circulate around the loop in the absence of applied fields or trapped magnetic flux. In this Chapter we shall analyze under which conditions spontaneous currents occur in superconducting loops with one or more  $\pi$  junctions, and how does the difference in the current-phase relations of 0 and  $\pi$  junctions manifest itself in the characteristics of 0 or  $\pi$  junction-based SQUIDs.

### 2.1 $\pi$ junction in an rf SQUID

A superconducting loop that contains one Josephson junction is often referred to as an rf SQUID (Superconducting Quantum Interference Device). An rf SQUID of geometric inductance  $L$  that contains a  $\pi$  junction is schematically shown in Figure

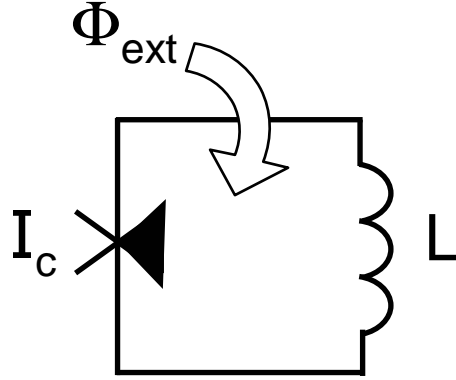


**Figure 2.1:** A  $\pi$  junction rf SQUID is a superconducting loop of inductance  $L$  with a  $\pi$  junction of critical current  $I_c$ . External magnetic flux  $\Phi_{ext}$  can be applied to the loop.

2.1. If the thickness of a superconducting filament that forms an rf SQUID loop is much greater than the London penetration depth  $\lambda$ , no current flows in the center of a filament. For a closed path going through the center of a superconducting filament, we can then write down the condition for the quantization of magnetic flux in the loop which is derived from the continuity of the order parameter:

$$2\pi \frac{\Phi_{ind} - \Phi_{ext}}{\Phi_0} + \phi = 2\pi n, \quad (2.1)$$

where  $\phi$  is the phase drop across the junction,  $\Phi_{ind} = LJ$  is the magnetic flux created by the current  $J$  circulating in the loop and  $\Phi_{ext}$  is the magnetic flux applied to the loop externally.

Using the inverse current-phase relation

$$\phi = \arcsin\left(\frac{J}{I_c}\right), \quad (2.2)$$

we can re-write the Equation (2.1) in terms of the phase drops  $\phi_{ext} = 2\pi\Phi_{ext}/\Phi_0$  and  $\phi_{ind} = 2\pi\Phi_{ind}/\Phi_0$  for  $n = 0$ :

$$\phi_{ext} = \phi_{ind} + \arcsin\left(\frac{\phi_{ind}}{\beta_L}\right) = 0. \quad (2.3)$$

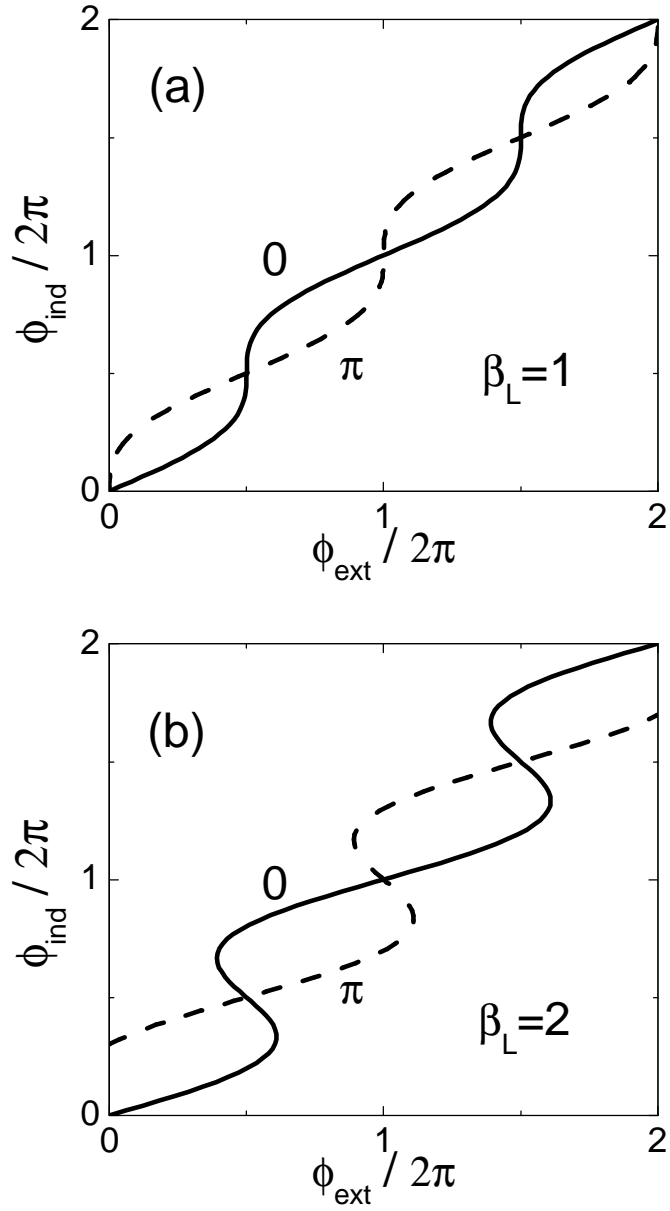


**Figure 2.2:** Magnetic flux induced in an rf SQUID with a 0 junction (solid line) and a  $\pi$  junction (dashed line) as a function of applied magnetic flux for (a) a nearly hysteretic rf SQUID with  $\beta_L = 1$  and (b) a hysteretic rf SQUID with  $\beta_L = 2$ .

where  $\beta_L$  is given by:

$$\beta_L = 2\pi \frac{LI_c}{\Phi_0}. \quad (2.4)$$

Because the critical current of a  $\pi$  junction is negative,  $\beta_L$  of an rf SQUID with a  $\pi$  junction is also negative. Figure 2.2 illustrates the difference between an rf SQUID based on a  $\pi$  junction and a conventional rf SQUID with a 0 junction. For  $0 < \phi_{ext} < \pi$ , the regular junction reduces the induced flux compared to the applied magnetic flux, whereas the  $\pi$  junction increases the induced flux. Parameter  $\beta_L$  is a measure of hysteresis of an rf SQUID. For  $\beta_L < 1$ , an rf SQUID is non-hysteretic,  $\phi_{ind}$  is a single-valued function of  $\phi_{ext}$  (Figure 2.2(a)). For  $\beta_L > 1$ , more than one value of  $\phi_{ind}$  corresponds to certain values of  $\phi_{ext}$ , the rf SQUID becomes hysteretic (Figure 2.2(b)). rf SQUIDs with SFS  $\pi$  junctions were studied in both the non-hysteretic [55] and the hysteretic [56] regimes.

The energy of an rf SQUID is the sum of the Josephson energy stored in the junction and the magnetic field energy of the circulating current  $J$ :

$$E = |E_J| \left( 1 - \frac{\beta_L}{|\beta_L|} \cos \phi \right) + \frac{LJ^2}{2} \propto |\beta_L| \left( 1 - \frac{\beta_L}{|\beta_L|} \cos \phi \right) + \frac{(\phi - \phi_{ext})^2}{2}, \quad (2.5)$$

The energy for  $\phi_{ext} = 0$  and  $\beta_L = 0, -0.5, -1, -1.5, \dots, -5$  as a function of the junction phase difference  $\phi$  is plotted in Figure 2.3(a). The energy has only one minimum at  $\phi = 0$  for  $|\beta_L| < 1$ . For  $|\beta_L| > 1$  the energy has a local maximum at  $\phi = 0$  and two symmetric side minima at  $\phi \neq 0$ . This means that the lowest energy state of an rf SQUID is the state with finite current flowing through the junction. As  $|\beta_L|$  is increased, the positions of the side minima approach  $\phi = \pm\pi$  asymptotically (see Figure 2.3(b)). In an rf SQUID with a 0 junction, a minimum at  $\phi = 0$  is present at all values of  $\beta_L$ , and the next closest minimum only occurs at  $\phi \sim 2\pi$  for large values of  $\beta_L$ . The potential with doubly degenerate minima makes  $\pi$  junction-based

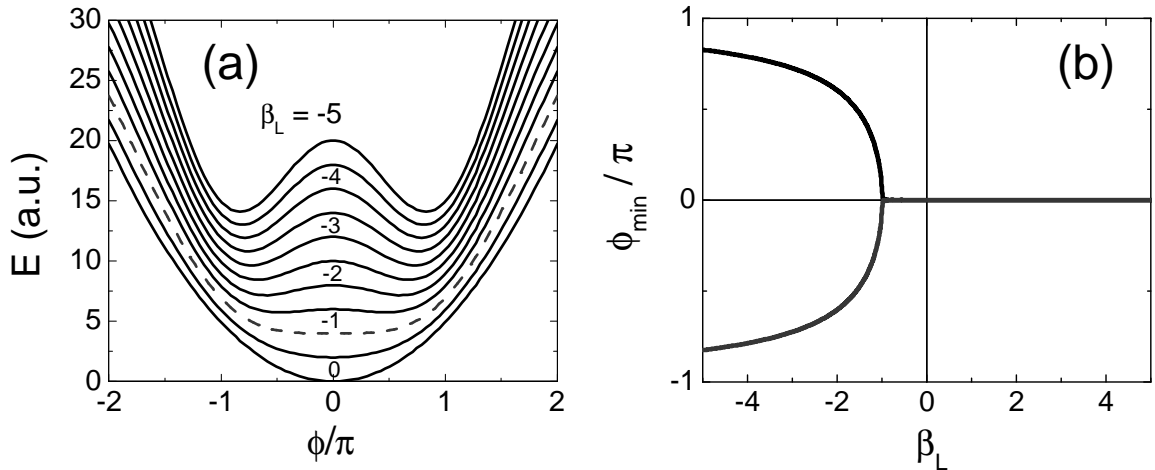


**Figure 2.3:** (a) Energy as a function of the junction phase difference for an rf SQUID with a  $\pi$  junction for various values of  $\beta_L$ . Curves are offset vertically for clarity. (b) Positions of energy minima as a function of  $\beta_L$ .

rf SQUIDS attractive as both classical and quantum logic elements [57–60]. The two logic states of a “ $\pi$ -bit” are the states with left and right spontaneously circulating currents.

According to the Equation (2.1), in the absence of applied magnetic flux the phase difference across the junction in an rf SQUID is proportional to the spontaneous magnetic flux in the loop. The magnitude of the spontaneous magnetic flux can be calculated if the rf SQUID energy given by the Equation (2.5) is minimized with respect to  $\phi$ . The spontaneous flux as a function of  $|\beta_L|$  is plotted in Figure 2.4(a). It onsets at  $|\beta_L|=1$  and approaches  $\Phi_0/2$  when  $|\beta_L|$  is large. The spontaneous circulating current is proportional to  $\Phi_{ind}/L$  and is plotted in Figure 2.4(b). It has a maximum at  $|\beta_L| > 1$  and is equal to zero when  $|\beta_L| \rightarrow \infty$ . Spontaneous flux in  $\pi$  junction SQUIDS as a function of  $\beta_L$  was directly measured in experiments on SNS and SFS  $\pi$  junctions [33; 56]. In these experiments, the change in  $\beta_L$  was due to the change in the critical current, which was adjusted by means of control voltage in the case of SNS  $\pi$  junctions (Figure 1.3) and by means of temperature in the case of SFS  $\pi$  junctions. An experiment in which the geometric inductance of the loop  $L$  is varied

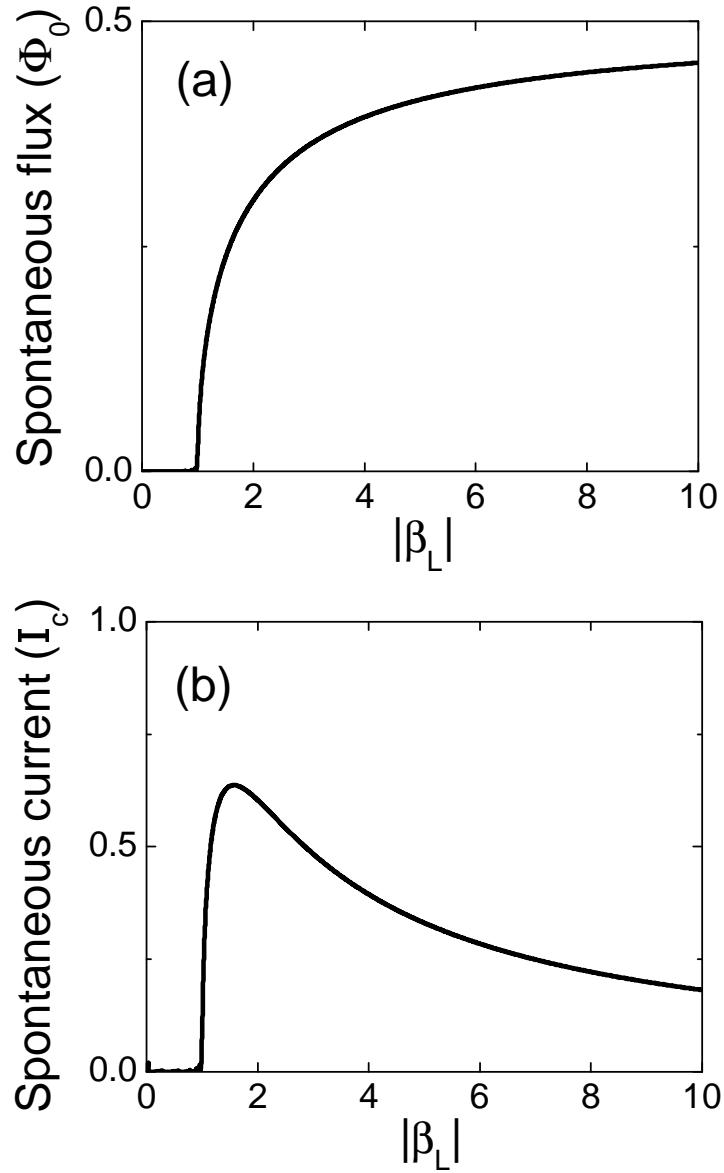


**Figure 2.4:** (a) Spontaneous flux in a  $\pi$  junction rf SQUID as a function of  $\beta_L$  (b) Spontaneous current circulating in a  $\pi$  junction rf SQUID as a function of  $\beta_L$ .

to produce a change in  $\beta_L$  is proposed in Chapter 5.

## 2.2 $\pi$ junction in a dc SQUID

A dc SQUID is a superconducting loop that contains two Josephson junctions. The phase quantization condition for a dc SQUID is:

$$2\pi \frac{\Phi_{ind} - \Phi_{ext}}{\Phi_0} + \phi_1 - \phi_2 = 2\pi n, \quad (2.6)$$

where  $\phi_1$  and  $\phi_2$  are the phase drops across the dc SQUID junctions. In the supercurrent state of a dc SQUID, the current  $I$  passed through a SQUID divides between the junctions 1 and 2:

$$I = I_{c1} \sin \phi_1 + I_{c2} \sin \phi_2, \quad (2.7)$$

The maximum supercurrent that can flow through a dc SQUID is  $I_{c1} + I_{c2}$ . Applied magnetic flux  $\Phi_{ext}$  depletes phases  $\phi_1$  and  $\phi_2$  causing interference between currents through the junctions 1 and 2. For a symmetric dc SQUID with  $I_{c1} = I_{c2} = I_c$  and no geometric inductance ( $L=0$ ), the SQUID critical current as a function of the applied magnetic flux  $\Phi_{ext}$  is [61]

$$I_c^{00} = 2I_c \left| \cos \left( \frac{\pi \Phi_{ext}}{\Phi_0} \right) \right|. \quad (2.8)$$

If one of the junctions in the symmetric dc SQUID loop is a  $\pi$  junction ( $0-\pi$  SQUID), so that  $I_{c1} = -I_{c2} = I_c$ , the critical current is given by

$$I_c^{0\pi} = 2I_c \left| \sin \left( \frac{\pi \Phi_{ext}}{\Phi_0} \right) \right|. \quad (2.9)$$

Figure 2.5 shows that the critical current vs. applied magnetic flux interference patterns of a  $0-\pi$  SQUID are shifted by  $1/2$  of a flux quantum  $\Phi_0$  from those of a  $0-0$  SQUID. The critical current of a  $0-\pi$  SQUID has a minimum in zero applied magnetic

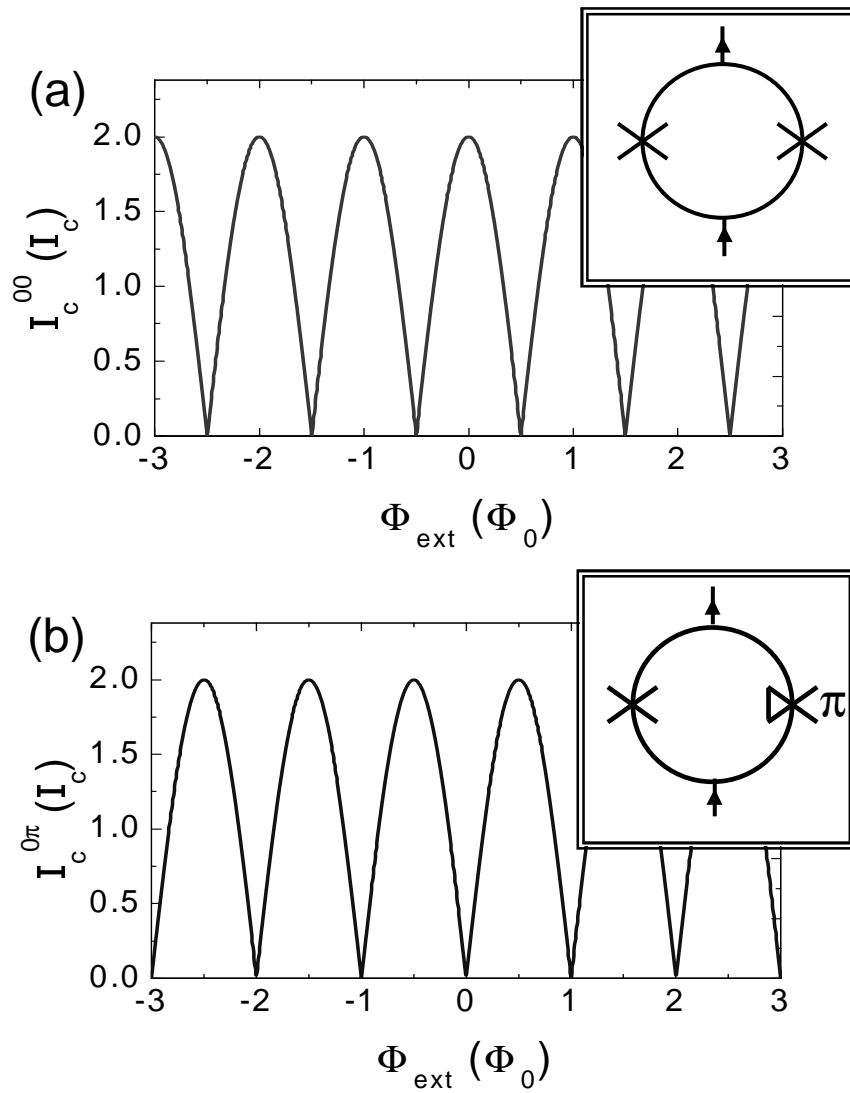


**Figure 2.5:** Critical current vs. applied magnetic flux interference patterns for (a) a symmetric 0-0 dc SQUID and (b) a symmetric 0- $\pi$  SQUID calculated for zero geometric inductance  $L=0$ .

flux. This can be understood as follows. Critical currents of the junctions in a 0- $\pi$  SQUID are equal in magnitude and opposite in sign. In the limit of zero inductance, the phases across both junctions should be the same. Therefore, currents through 0 and  $\pi$  junctions interfere destructively in zero applied field. Experimentally, half-periodic shifts in the interference patterns of dc SQUIDs can be used as the evidence of the  $\pi$  junction state. Interference patterns showing half a flux quantum shifts were measured in dc SQUIDs made with SNS [33] and SFS [62]  $\pi$  junctions.

The energy of a dc SQUID is a sum of the Josephson energies of the junctions and the magnetic field energy of the current  $J$  circulating in the loop:

$$E = |E_{J1}| \left( 1 - \frac{\beta_1}{|\beta_1|} \cos \phi_1 \right) + |E_{J2}| \left( 1 - \frac{\beta_2}{|\beta_2|} \cos \phi_2 \right) + \frac{LJ^2}{2}, \quad (2.10)$$

where  $\beta_{1,2} = 2\pi I_{c1,2}L/\Phi_0$ . The current circulating in the dc SQUID loop is equal to

$$J = \frac{\phi_2 - \phi_1 + \phi_{ext}}{2\pi L} \Phi_0, \quad (2.11)$$

In the absence of applied magnetic flux,  $J = 0$  for a 0-0 SQUID. In a 0- $\pi$  SQUID the situation is different. Both 0 junction and  $\pi$  junction cannot be in their lowest energy states at the same time. Energy considerations then dictate whether or not spontaneous current circulates in the dc SQUID. If the difference in the Josephson energies of 0 and  $\pi$  junctions is greater than the energy required to generate spontaneous current, the junction with higher Josephson energy will remain in its lowest energy state, while the other junction will be in its highest energy state. For example, if  $I_{c0} \gg I_{c\pi}$ , both junction phases will be equal to zero:  $\phi_0 = \phi_\pi = 0$ . In the opposite case when  $I_{c0} \ll I_{c\pi}$ ,  $\phi_0 = \phi_\pi = \pi$ . In the intermediate regime, where the values of both critical currents are comparable, it is advantageous to deplete the phases of the junctions, which means that the spontaneous current will circulate in the SQUID.

Figure 2.6 shows that the energy of a symmetric 0-0 SQUID of finite inductance is minimized in zero field when both junctions are at a phase difference of 0 *modulo*  $2\pi$ .

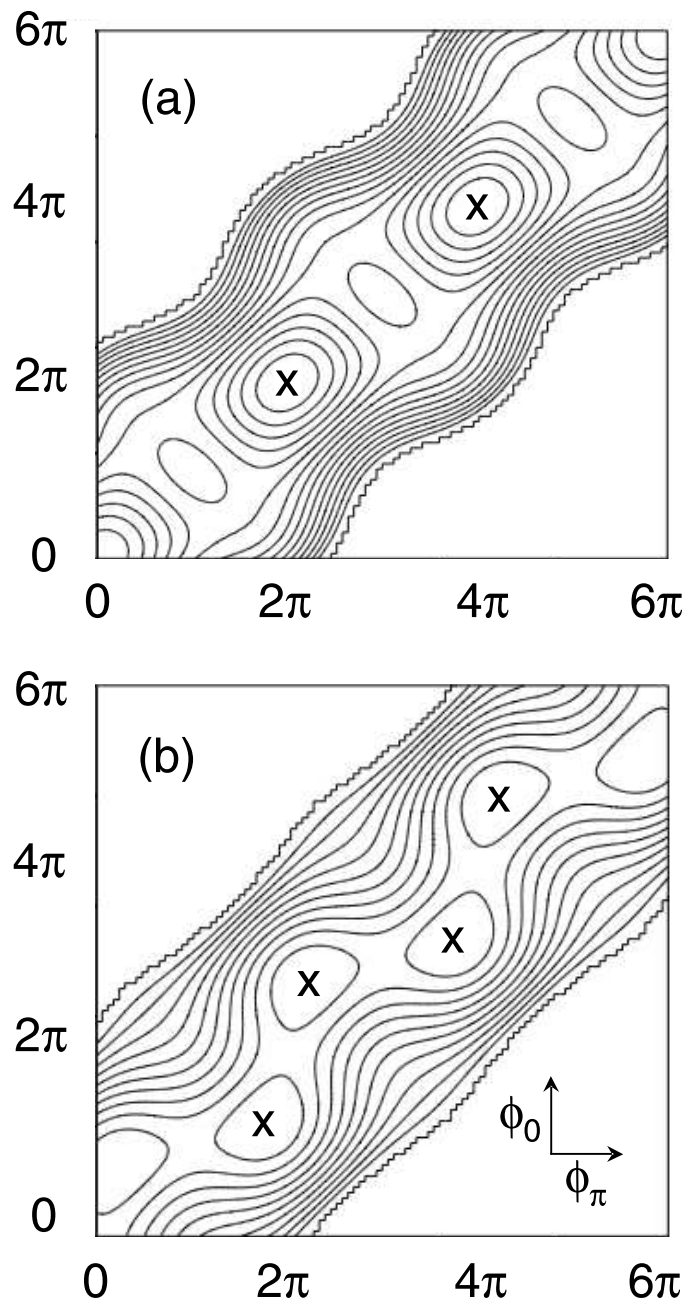


**Figure 2.6:** Contour plots of energy as a function of dc SQUID junction phases for (a) a 0-0 SQUID and (b) a 0- $\pi$  SQUID.  $\beta=3$  and the applied magnetic flux is zero. Energy minima are marked with “x”.

In a symmetric  $0-\pi$  SQUID, the energy is minimized when  $\phi_0 \neq \phi_\pi$ , which according to (2.11) corresponds to a non-zero spontaneous circulating current  $J$ .

To study the conditions for the onset of spontaneous currents in  $0-\pi$  SQUIDs we need to determine in what range of parameters does the  $0-\pi$  SQUID energy have minima at  $\phi_0 \neq \phi_\pi \text{ modulo } 2\pi$ . We look for zeroes of the derivatives of the dc SQUID energy with respect to  $\phi_0$  and  $\phi_\pi$ :

$$\begin{aligned}\frac{dE}{d\phi_0} &\propto \beta_0 \sin \phi_0 + \phi_0 - \phi_\pi = 0 \\ \frac{dE}{d\phi_\pi} &\propto -|\beta_\pi| \sin \phi_\pi + \phi_\pi - \phi_0 = 0\end{aligned}\tag{2.12}$$

Here we use

$$\begin{aligned}\beta_0 &= 2\pi \frac{I_{c0} L}{\Phi_0} \\ \beta_\pi &= 2\pi \frac{I_{c\pi} L}{\Phi_0}\end{aligned}\tag{2.13}$$

If the dc SQUID bias current is zero, currents flowing through both junctions in the dc SQUID are equal:

$$\beta_0 \sin \phi_0 = |\beta_\pi| \sin \phi_\pi.\tag{2.14}$$

At the onset of spontaneous currents the phase differences  $\phi_0$  and  $\phi_\pi$  are close to either 0 or  $\pi$ , therefore the sine function can be linearized:

$$\begin{aligned}\sin \phi_0 &= \phi_0, \quad \sin \phi_\pi = \phi_\pi & \phi_0, \phi_\pi \rightarrow 0 \\ \sin \phi_0 &= -\phi_0, \quad \sin \phi_\pi = -\phi_\pi & \phi_0, \phi_\pi \rightarrow \pi\end{aligned}\tag{2.15}$$

Substituting (2.14) into the system of Equations (2.12) and after linearization (2.15) we get the following conditions for the onset of spontaneous currents:

$$|\beta_\pi| = \frac{\beta_0}{1 + \beta_0}, \quad \phi_0, \phi_\pi \rightarrow 0$$

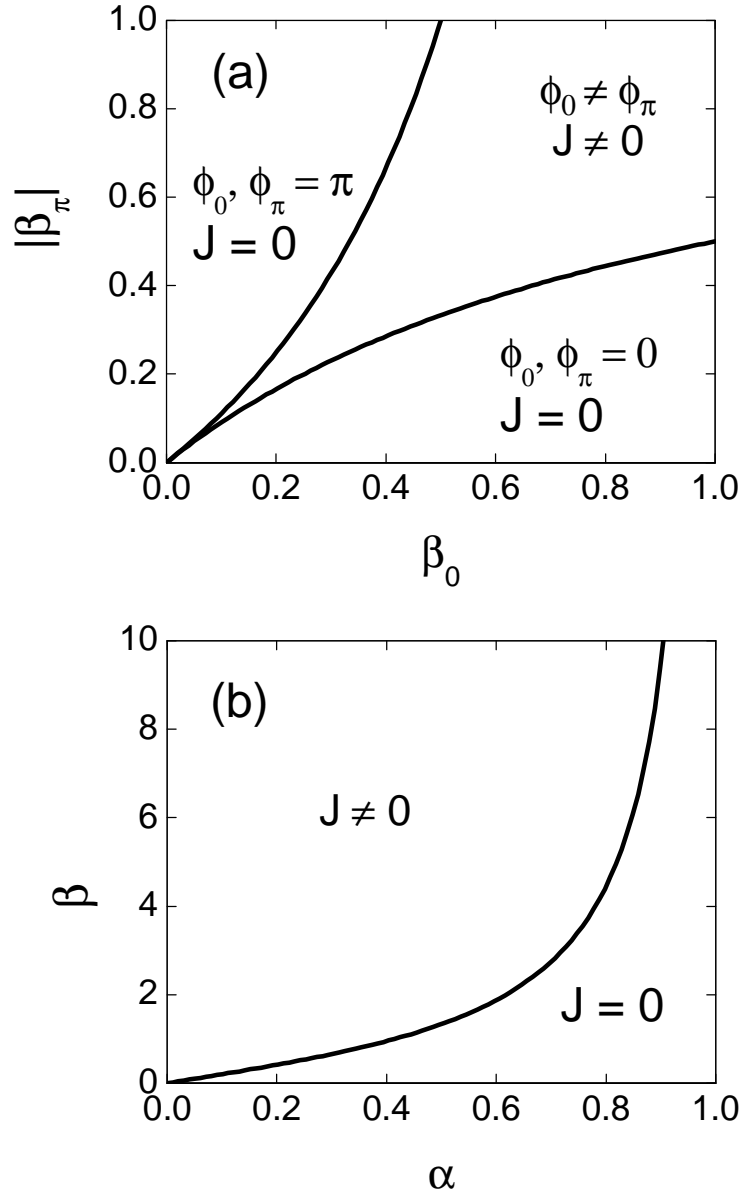


**Figure 2.7:** Phase diagram of spontaneous currents in a 0- $\pi$  SQUID in the  $\beta_0$ - $|\beta_\pi|$  representation [panel (a)] and in the  $\alpha$ - $\beta$  representation [panel (b)].

$$\beta_0 = \frac{|\beta_\pi|}{1 + |\beta_\pi|}, \quad \phi_0, \phi_\pi \rightarrow \pi \quad (2.16)$$

or, in terms of the dc SQUID inductance parameter  $\beta = (\beta_0 + |\beta_\pi|)/2$  and the asymmetry parameter  $\alpha = |\beta_0 - |\beta_\pi||/(\beta_0 + |\beta_\pi|)$ :

$$\beta = \frac{2\alpha}{1 - \alpha^2}. \quad (2.17)$$

The regimes of equal phases and of spontaneous currents for  $0-\pi$  SQUIDs are demonstrated in Figure 2.7(a). Regions with  $\phi_0 = \phi_\pi = 0$  and  $\phi_0 = \phi_\pi = \pi$  are separated by a region in which spontaneous currents circulate in  $0-\pi$  SQUIDs, and the junction phases are not equal. The spontaneous currents onset along the lines defined by the Equations (2.16). In Figure 2.7(b) regimes of zero spontaneous currents and of finite spontaneous currents are presented in the  $\alpha - \beta$  space. Such graphs can be called the spontaneous current phase diagrams. In contrast to rf SQUIDs, spontaneous currents exist in dc  $0-\pi$  SQUIDs for arbitrarily small  $\beta$ , provided the critical current asymmetry  $\alpha$  is small enough according to (2.17). Experimentally, spontaneous currents were directly observed in dc SQUIDs made of two controllable mesoscopic SNS junctions (Figure 1.3) [19]. Spontaneous currents appeared at a finite control voltage applied to one of the junctions, and disappeared at a higher control voltage. It is likely that the SQUID was crossing the region of spontaneous currents, going from the state with both junction phases at 0 to the state with both junction phases at  $\pi$ .

## 2.3 Arrays of $\pi$ junctions

Arrays of connected superconducting loops that incorporate  $\pi$  junctions exhibit more complicated behavior than single loops with  $\pi$  junctions. Many different spontaneous

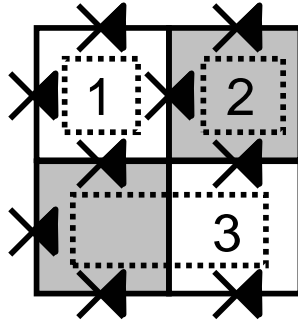


**Figure 2.8:** Diagram of a  $2 \times 2$  square array. Loop 1 contains 4  $\pi$ -junctions, loop 2 contains 3  $\pi$ -junctions, loop 3 contains two array cells and a total of 5  $\pi$ -junctions. Frustrated cells are shaded.

current configurations are permitted by the fluxoid quantization rules. Currents in the adjacent array cells interact with each other, lifting the degeneracy of the array states.

In Figure 2.8 a diagram of a  $2 \times 2$  square array with different numbers of  $\pi$  junctions in the individual cells is demonstrated. Cells with odd numbers of  $\pi$  junctions are called *frustrated*, cells with even numbers of  $\pi$  junctions are *unfrustrated*. The array in Figure 2.8 is *checkerboard frustrated*, because nearest neighbors of each frustrated cell are unfrustrated, and *vice versa*. Below we shall consider fully-frustrated square arrays with 3  $\pi$ -junctions in each cell. Other array types will be discussed in Chapter 8 in connection with the experimental study of arrays.

It is easy to demonstrate that in a single superconducting loop of inductance  $L$  with 3 identical  $\pi$  junctions of the critical current  $I_c$  the onset of spontaneous currents is at  $\beta_L = 2\pi I_c L / \Phi_0 = 3$ . A larger geometric inductance is required to onset the spontaneous currents in a loop with 3 identical junctions compared to an rf SQUID. For  $\beta_L < 3$  the energy is minimized when two of the junctions are in the state with the phase difference of  $\pi$ , and the third junction is in the state with zero phase difference. The case of identical junctions is difficult to realize in practice. In experiments, critical currents of all junctions in the array are different. The onset of spontaneous currents

will then be determined by the junction with the smallest critical current  $I_c^{min}$ . All other junctions in the loop will increase the effective inductance of the loop by the amount of their net Josephson inductance  $L_J$ , determined from the energy required to pass a current through a Josephson junction. As a result, in an asymmetric loop with 3  $\pi$ -junctions the onset of spontaneous currents is at  $\beta_L = 2\pi I_c^{min}(L + L_J)/\Phi_0 = 1$ , meaning that a smaller geometric inductance  $L$  is required for the onset of spontaneous current compared to an rf SQUID with a  $\pi$  junction  $I_c^{min}$ .

In an array of 3-junction loops, the conditions for the onset of spontaneous currents are more complicated, because the adjacent cells also add to the effective inductance. Besides, loops containing more than one elementary cell of the array have higher geometric inductances, and may onset spontaneous currents at even lower values of the critical currents (see loop 3 in Figure 2.8). In general, very little cell inductance is required for spontaneous currents to appear in large arrays. For now we assume that spontaneous currents circulate in the arrays at any  $\beta_L$ .

The energy diagrams of spontaneous current configurations in the arrays can be obtained by numerical simulations [63]. In the simulations, the phase differences across the junctions of the arrays are initialized randomly. The Josephson equations are then iterated until phases reach equilibrium values corresponding to one of the allowed configurations. Energy for each configuration can be calculated from the equilibrium phases. Using this method the ground state and the higher energy metastable states of an array can be determined.

Figure 2.9 shows the results of numerical simulations for  $2 \times 2$  square arrays with 3 junctions per cell. In panel (a) all junctions are in the 0 state. There are no circulating currents in the ground state at zero applied magnetic flux. If the applied magnetic flux is half a flux quantum per cell, screening currents circulate in the array. The flux generated by currents is aligned antiferromagnetically, meaning that the currents in

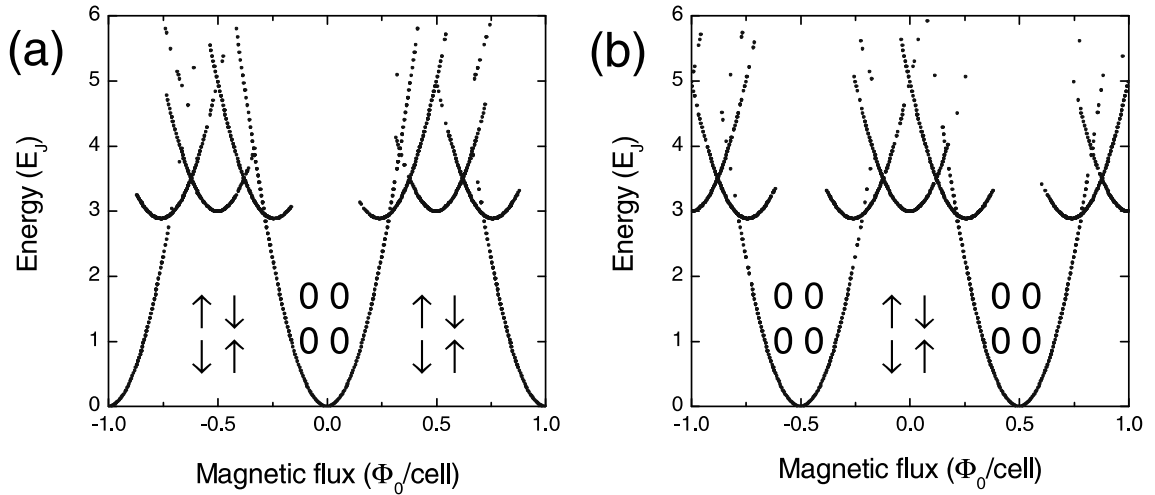


**Figure 2.9:** Energy vs. applied magnetic flux for  $2 \times 2$  square arrays with (a) 3 0-junctions per cell (b) 3  $\pi$ -junctions per cell. Spontaneous current configurations at  $\Phi=0, 0.5 \Phi_0$  and  $-0.5 \Phi_0$  are shown by diagrams.  $\beta_L = 0.1$

the nearest neighbor cells circulate in the opposite directions. Different branches of the energy vs. flux plot correspond to different states of the array, with the lowest branch being the ground state. For a 0-junction array in zero applied magnetic flux the first excited state is a state with an additional flux quantum in one of the cells. In a symmetric  $2 \times 2$  array the first excited state has a degeneracy of 8.

If 0 junctions are replaced with  $\pi$  junctions, the energy diagram is shifted by  $0.5 \Phi_0$  (Figure 2.9(b)). The ground state at zero applied magnetic flux becomes the state with the antiferromagnetic alignment of currents. These currents circulate spontaneously, since there is no external magnetic flux to screen. At  $\Phi = 0.5 \Phi_0$  the applied magnetic flux compensates the phase shift of  $\pi$  due to  $\pi$  junctions. This satisfies the fluxoid quantization condition in each cell, therefore no spontaneous currents circulate in the ground state.

In larger arrays the energy diagrams become more complicated, each additional cell adding a branch to the array energy diagram. Figure 2.10 shows the energy vs. magnetic flux diagram for a  $6 \times 6$  fully-frustrated array. The ground state of the array

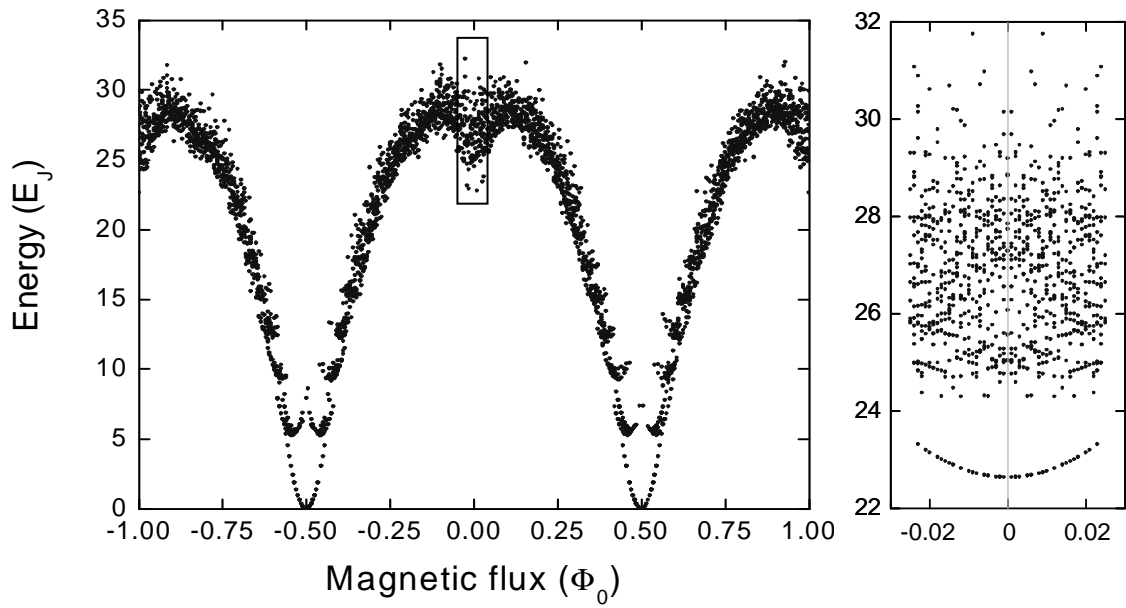


**Figure 2.10:** Energy vs. applied magnetic flux for a fully-frustrated  $6 \times 6$  square array with  $\beta_L = 0.1$ .

at zero applied magnetic flux has spontaneous currents in the antiferromagnetic order. The excited states with one or more of the spontaneous currents flipped compared to the ground state configuration form a band of closely spaced states. This excited band is separated from the ground state by a small gap which is illustrated in the right panel of Figure 2.10.

# Chapter 3

## Proximity Effect in Ferromagnets

### 3.1 Order parameter oscillations in a ferromagnet

If a superconductor (S) is placed in contact with a normal metal (N), superconducting correlations between electrons can be observed in the normal metal at distances on the order of a normal metal coherence length  $\xi_N$  away from the superconductor. At the same time, unpaired electrons with subgap energies penetrate the superconductor as far as the superconducting coherence length  $\xi_0$  away from the SN-interface. Superconducting correlations induced in the normal material and the quasiparticle poisoning of the superconductor are called the proximity effects. Due to the proximity effects, the superconducting transition temperature of a thin superconducting film, with thickness on the order of a superconducting coherence length  $\xi_0$ , in contact with a normal layer can be decreased or fully suppressed. Josephson effects in SNS junctions can be explained in terms of the exchange of superconducting correlations between the two superconductors separated by a metallic barrier in the proximity regime.

Typically, the order parameter induced in the normal layer decays monotonically

as a function of distance  $x$  from the superconductor-normal metal boundary:

$$\Psi(x) = \Psi(0)e^{-\frac{x}{\xi_N}}, \quad (3.1)$$

where  $\Psi(0)$  is the magnitude of the order parameter at the SN-boundary.

If a normal metal is ferromagnetic, the situation changes qualitatively. Instead of a monotonic decay, the order parameter oscillates in space [15]. A simple description of this phenomenon was given by Demler, Arnold and Beasley [64]. Consider a Cooper pair entering a ferromagnet from a spin-singlet superconductor. For now we assume that both the ferromagnet and the superconductor are clean, so that  $\mathbf{k}$  is a good quantum number. The ferromagnetic exchange field  $H$  splits the energies of spin-up and spin-down electrons in a Cooper pair by the amount  $2E_{ex} = 2\mu_B H$ . To conserve the total energy, electrons adjust their kinetic energies (Figure 3.1(a)). Both electrons shift their quasimomenta by  $\Delta p = E_{ex}/\hbar v_F$ . The resulting center of mass momentum of the Cooper pair is  $Q = 2E_{ex}/\hbar v_F$ . In a superconductor, the wavefunction of a Cooper pair with momentum  $Q$  is a plane wave:

$$\Psi(x) = \Psi(0)e^{-iQx}. \quad (3.2)$$

In a normal metal it becomes an evanescent plane wave:

$$\Psi(x) = \Psi(0)e^{-\frac{x}{\xi_N}} e^{-iQx}. \quad (3.3)$$

Cooper pairs with antisymmetric spin configurations obtain the center of mass momentum of the opposite sign,  $-Q$ , as illustrated in the lower panel of Figure 3.1(b). The order parameter is the average over all Cooper pair configurations:

$$\Psi(x) = \Psi(0)e^{-\frac{x}{\xi_N}} \frac{e^{-iQx} + e^{+iQx}}{2} = \Psi(0)e^{-\frac{x}{\xi_N}} \cos(Qx). \quad (3.4)$$

This simple form of the order parameter in a ferromagnet only includes electrons that enter the ferromagnet with momenta normal to the SF-interface. Integration over

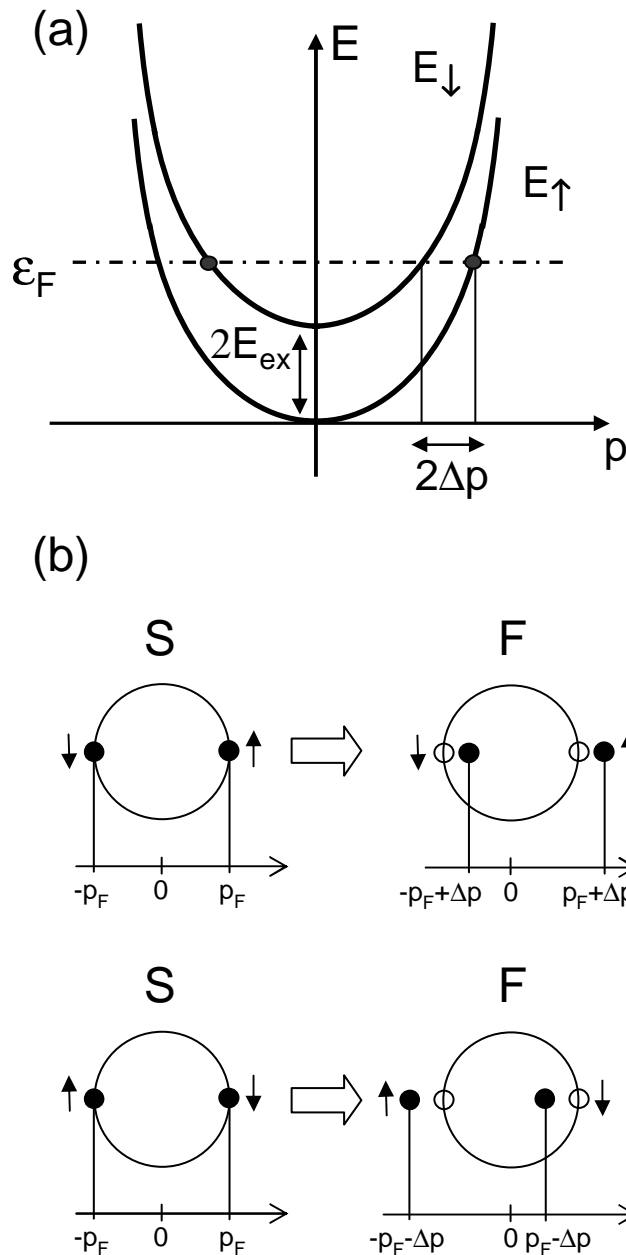


**Figure 3.1:** (a) Energy bands of spin-up and spin-down electrons are depleted by the exchange field, this forces electrons to adjust their momenta (b) As Cooper pairs travel from the superconductor S into the ferromagnet F, their center of mass momenta are shifted in the positive or in the negative direction depending on the spin configuration. Adapted from [64].

all possible momenta of electrons renormalizes the expression for the order parameter, but does not change the oscillation period [64]. The difference in the proximity-induced order parameters in SN and SF structures is illustrated in Figure 3.2. In the case of a normal metal, the phase of the order parameter remains constant. In a ferromagnet, the phase jumps by  $\pi$  after every half period of the order parameter oscillation.

In the most experimentally relevant case of a diffusive ferromagnet, the qualitative picture discussed above holds quite well. The decay and the oscillations of the order parameter can be expressed using the complex ferromagnetic coherence length  $\xi_F$ :

$$\Psi(x) = \Psi(0)e^{-x/\xi_F} + c.c., \quad (3.5)$$

$$\xi_F = \sqrt{\frac{\hbar D}{2(\pi k_B T + iE_{ex})}}, \quad (3.6)$$

where  $D$  is the diffusion constant. The decay length  $\xi_{F1}$  and the oscillation period  $2\pi\xi_{F2}$  are related to the coherence length  $\xi_F$  as follows:

$$\frac{1}{\xi_F} = \frac{1}{\xi_{F1}} + i\frac{1}{\xi_{F2}}. \quad (3.7)$$

According to (3.6) and (3.7),  $\xi_{F1}$  and  $\xi_{F2}$  are given by [18]:

$$\xi_{F1,F2} = \left\{ \frac{\hbar D}{[(\pi k_B T)^2 + E_{ex}^2]^{1/2} \pm \pi k_B T} \right\}^{1/2}. \quad (3.8)$$

We can see that at finite temperatures  $\xi_{F1}$  and  $\xi_{F2}$  are not equal. They become equal at zero temperature or when the exchange energy  $E_{ex}$  is much greater than the thermal energy  $k_B T$ . The temperature dependences of  $\xi_{F1}$  and  $\xi_{F2}$  calculated from the Equations (3.8) for  $E_{ex} = 50$  K are shown in Figure 3.3.

The effects of the oscillations of the order parameter in SF structures can be observed in a number of experiments. The quasiparticle density of states at the Fermi

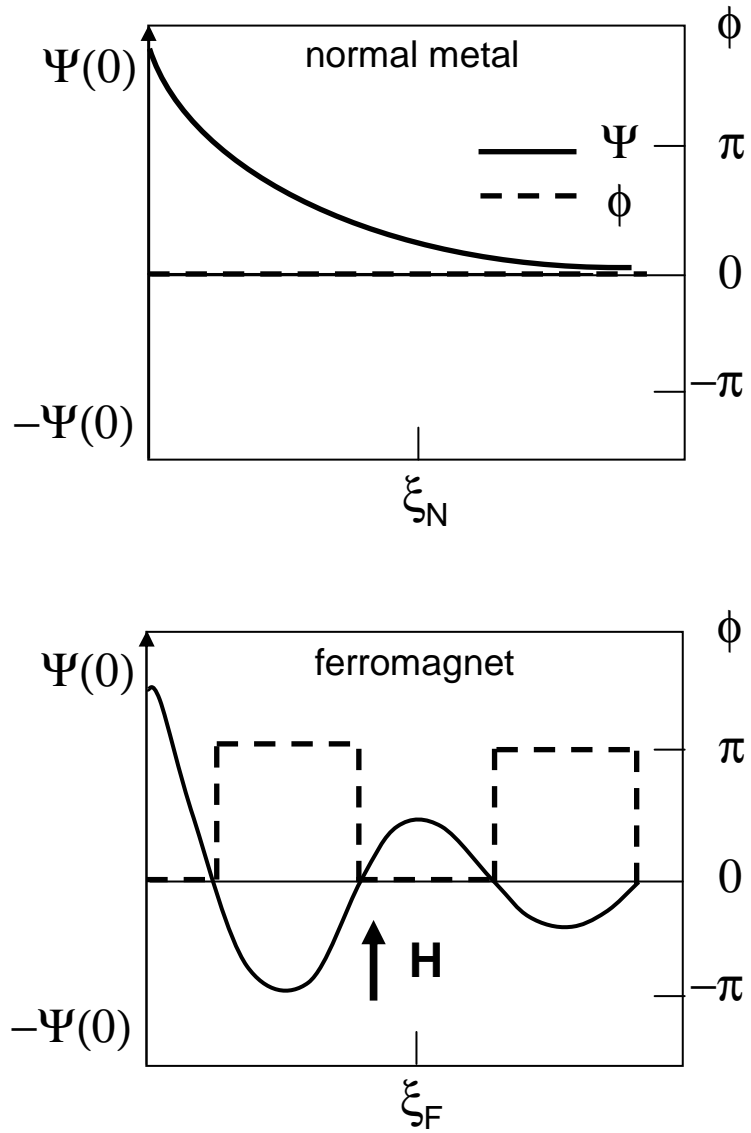


**Figure 3.2:** The order parameter in the normal metal decays monotonically, while its phase remains zero. In a ferromagnet, the order parameter oscillates, and its phase jumps between 0 and  $\pi$ .

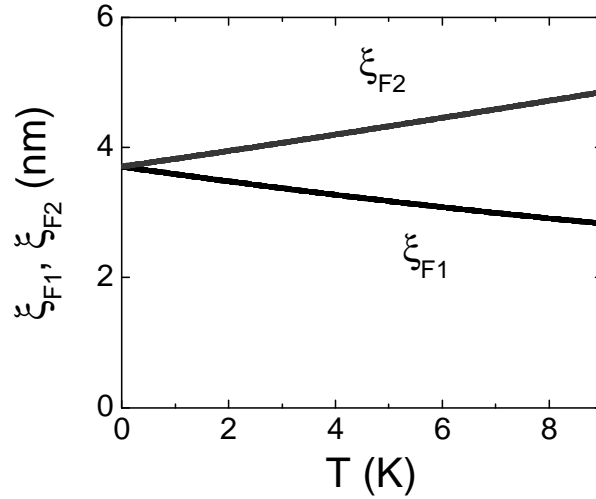


**Figure 3.3:** Temperature dependence of the decay length  $\xi_{F1}$  and the oscillation length  $\xi_{F2}$  calculated from (3.8) using  $E_{ex}=50$  K.

level was predicted to oscillate in a ferromagnet in proximity with a superconductor, enhancing at thicknesses where superconducting correlations are suppressed [65]. This effect was observed in the measurements of the tunneling spectra of S/F/I/N *Al/Al<sub>2</sub>O<sub>3</sub>/PdNi/Nb* tunnel junctions performed at temperatures above the  $T_c$  of aluminum [66]. In addition, the magnitude of the exchange energy can be extracted from the tunneling spectra of SFIN junctions [67]. In thin SF bilayers and FSF trilayers, a non-monotonic dependence of the superconducting transition temperature  $T_c$  on the F-layer thickness was predicted [68] and observed [69; 70]. A simple explanation of this effect can be given based on the boundary conditions for the order parameter in a ferromagnet [70]. The amplitude of the order parameter at the superconductor-ferromagnet boundary is affected by the condition that the derivative of the order parameter on the ferromagnet-vacuum boundary must be zero. If the ferromagnetic layer thickness is 1/4 of the oscillation period, the order parameter must be zero at the SF interface. In thin superconducting films, this significantly reduces the Ginzburg-Landau free energy, which determines the transition temperature  $T_c$ .

## 3.2 SFS Josephson junctions

Oscillations of the order parameter can also influence the Josephson effect in SFS junctions. As a function of the barrier thickness, the Josephson critical current oscillates, reaching zero and changing sign at a number of barrier thickness values [71–73].

Oscillations of the critical current in SFS junctions were first predicted by Buzdin, Bulaevskii and Panjukov in the clean limit [15] using the Eilenberger equations [74]. Later, Buzdin and Kupriyanov showed, by means of solving the Usadel equations [75], that the critical current should also oscillate in diffusive junctions [76]. The formal treatment of the proximity effect in SF structures involving the Usadel, Eilenberger, Bogoliubov-de Gennes and Ginzburg-Landau equations is presented in the reviews by Buzdin [77] and Golubov et al. [40]. Here we shall only discuss the qualitative picture of the Josephson effect in SFS junctions in terms of the overlap of the oscillating wavefunctions.

We consider an SFS junction of barrier thickness  $d$  shown in Figure 3.4. A finite phase difference  $\phi$  is maintained between the two superconductors so that  $\Psi(-d/2) = \Psi_0$ , and  $\Psi(d/2) = e^{i\phi}\Psi_0$ , where  $\Psi_0$  is the magnitude of the order parameter in the bulk of the superconductor away from the junction. The order parameter in the barrier can be represented as a sum of decaying oscillations from the left and from the right superconductor-ferromagnet interfaces:

$$\Psi(x) = A \exp\left(-\frac{x+d/2}{\xi_{F1}}\right) \cos\left(\frac{x+d/2}{\xi_{F2}}\right) + B e^{i\phi} \exp\left(\frac{x-d/2}{\xi_{F1}}\right) \cos\left(\frac{x-d/2}{\xi_{F2}}\right) \quad (3.9)$$

If the barrier is thick enough, so that  $d \gg \xi_{F1}$ , we can put  $A = B = \Psi_0$ . Substituting the OP in this form into the expression for the quantum mechanical current in zero vector potential:  $J \sim \Psi \nabla \Psi^* - \Psi^* \nabla \Psi$ , and taking  $x = d/2$ , we obtain the

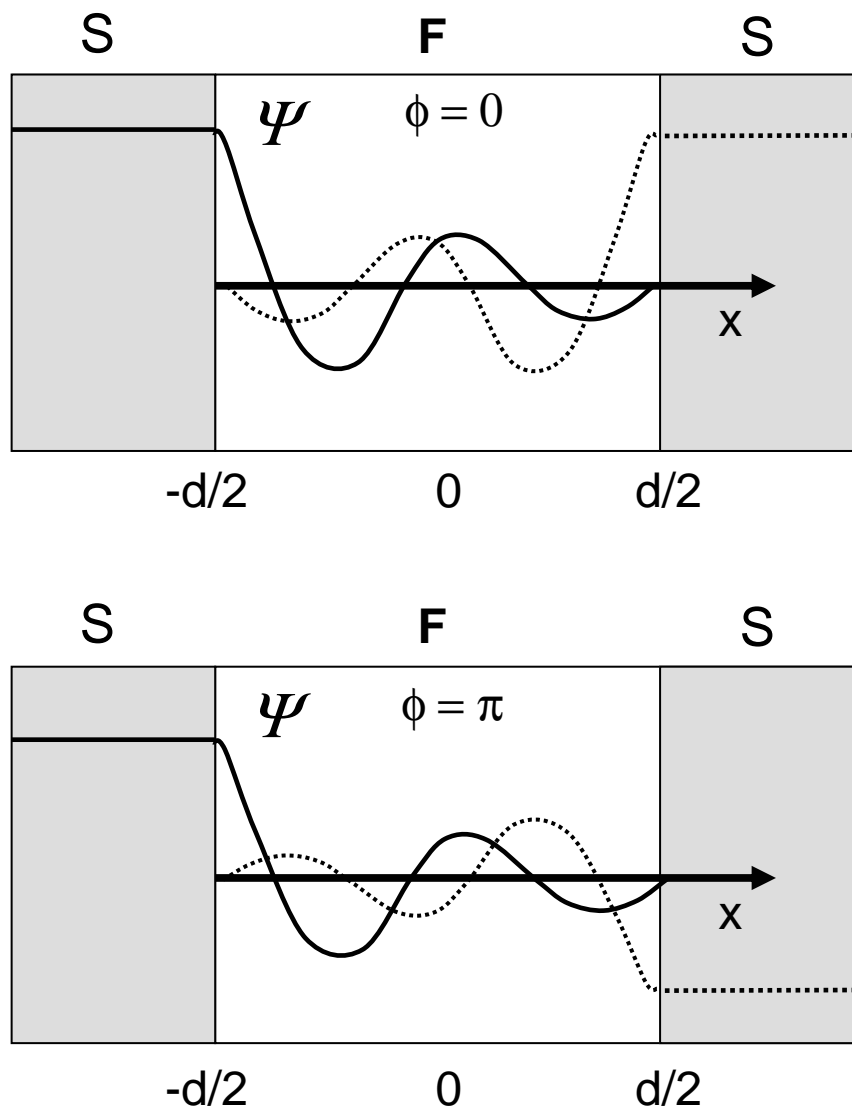


**Figure 3.4:** SFS junction showing a superposition of the oscillating order parameters from the left and from the right SF boundaries for the phase differences of 0 and  $\pi$ .

following current-phase relation:

$$J(d) \propto \sin \phi \left[ \cos \left( \frac{d}{\xi_{F2}} \right) + \frac{\xi_{F1}}{\xi_{F2}} \sin \left( \frac{d}{\xi_{F2}} \right) \right] \exp \left( -\frac{d}{\xi_{F1}} \right), \quad (3.10)$$

If  $d \lesssim \xi_{F1,2}$ , tails of the wavefunctions from the left and from the right overlap significantly, and the coefficients A and B are given by [78]:

$$\begin{aligned} A &= \Psi_0 \frac{e^{i\phi} \exp \left( -\frac{d}{\xi_{F1}} \right) \cos \left( \frac{d}{\xi_{F2}} \right) - 1}{\exp \left( -\frac{2d}{\xi_{F1}} \right) \cos^2 \left( \frac{d}{\xi_{F2}} \right) - 1} \\ B &= \Psi_0 \frac{\exp \left( -\frac{d}{\xi_{F1}} \right) \cos \left( \frac{d}{\xi_{F2}} \right) - e^{i\phi}}{\exp \left( -\frac{2d}{\xi_{F1}} \right) \cos^2 \left( \frac{d}{\xi_{F2}} \right) - 1} \end{aligned} \quad (3.11)$$

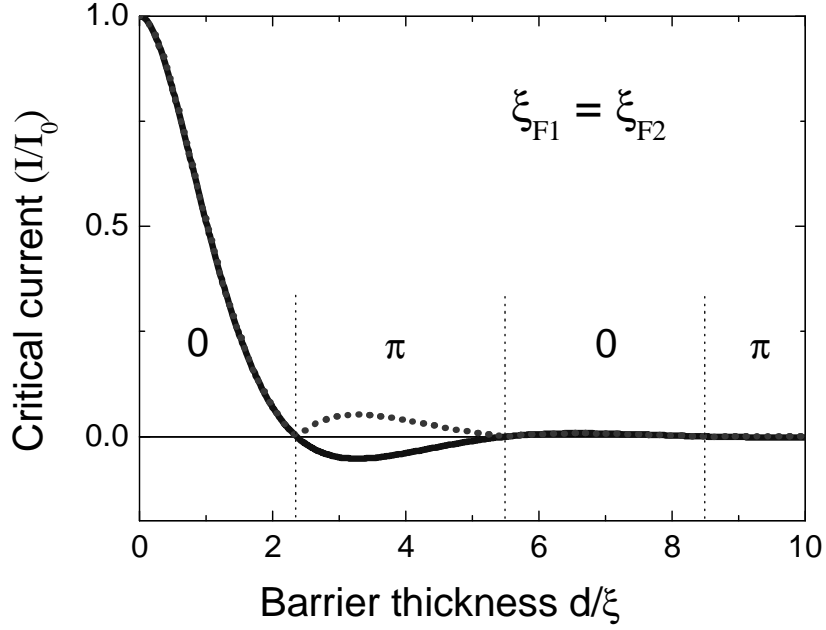
The current-phase relation in this case is of the form:

$$J(d) \propto \sin \phi \frac{\cos \left( \frac{d}{\xi_{F2}} \right) \sinh \left( \frac{d}{\xi_{F1}} \right) + \frac{\xi_{F1}}{\xi_{F2}} \sin \left( \frac{d}{\xi_{F2}} \right) \cosh \left( \frac{d}{\xi_{F1}} \right)}{\cos^2 \left( \frac{d}{\xi_{F2}} \right) \sinh^2 \left( \frac{d}{\xi_{F1}} \right) + \sin^2 \left( \frac{d}{\xi_{F2}} \right) \cosh^2 \left( \frac{d}{\xi_{F1}} \right)}, \quad (3.12)$$

It is easy to verify that (3.12) becomes (3.10) for  $d \gg \xi_{F1}$ . The thickness dependence of the critical current (3.10) for  $\xi_{F1} = \xi_{F2}$  is plotted in Figure 3.5. Conventional transport measurements of the Josephson junction current-voltage (IV) characteristics only reveal the absolute value of the critical current. Figure 3.5 shows that  $|I_c(d)|$  exhibits nodes at a number of thicknesses. In fact, at each node the critical current changes sign, and the junction undergoes a transition between the 0 junction and the  $\pi$  junction states.

To illustrate transitions between the 0 junction and the  $\pi$  junction states it is helpful to consider the Ginzburg-Landau free energy of the order parameter in the junction barrier:

$$F_{GL} \propto \int_{-\frac{d}{2}}^{\frac{d}{2}} \left[ \Psi^2 + \frac{d^2 \Psi}{dx^2} \right] dx. \quad (3.13)$$



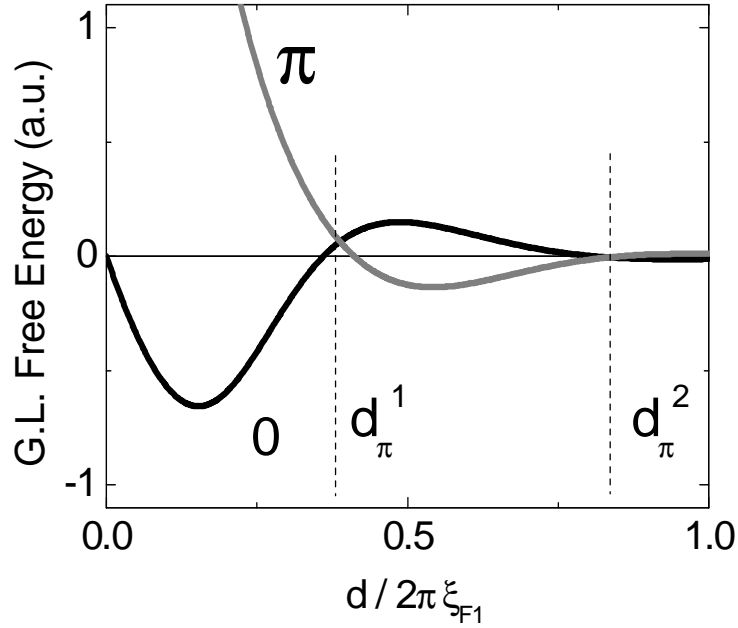
**Figure 3.5:** Thickness dependence (solid line) of the critical current of SFS junctions with  $\xi_{F1} = \xi_{F2}$ . Dashed line indicates the absolute value of the critical current.

Figure 3.6 shows the Ginzburg-Landau free energy for SFS junctions with  $\xi_{F1} = \xi_{F2}$  for phase differences  $\phi = 0$  and  $\phi = \pi$  as a function of barrier thickness  $d$  [78]. The state with  $\phi = 0$  becomes the high energy state for  $d_{\pi}^1 < d < d_{\pi}^2$ , meaning that the junction is in the  $\pi$  junction state.

The Josephson energy  $E_J$  (1.12) is related to the junction free energies at 0 and  $\pi$  phase differences  $F_{GL}^0 = F_{GL}(\phi = 0)$  and  $F_{GL}^{\pi} = F_{GL}(\phi = \pi)$  as follows:

$$E_J = \frac{F_{GL}^0 - F_{GL}^{\pi}}{2}. \quad (3.14)$$

Therefore,  $E_J > 0$  for  $d < d_{\pi}^1$ , and  $E_J < 0$  for  $d_{\pi}^1 < d < d_{\pi}^2$ . At  $d = d_{\pi}^{1,2,3,\dots}$  the Josephson energies and the critical currents of the junctions are zero. It should be stressed that calculations of the Ginzburg-Landau free energy done using the simplified wavefunction (3.4) only give the approximate results for  $d_{\pi}^1$  and other nodes of the  $I_c(d)$  dependence. A more accurate approach is to look for numerical solutions of the Eilenberger or the Usadel equations.



**Figure 3.6:** Ginzburg-Landau free energy of states with the phase differences of 0 and  $\pi$  as a function of the barrier thickness for SFS junctions with  $\xi_{F1} = \xi_{F2}$ . Adapted from [18].

Buzdin and Kupriyanov predicted that in junctions with  $d$  close to a thickness of a node  $d_{\pi}^n$ , transitions from the 0 junction to the  $\pi$  junction state can be observed as a function of temperature [76]. According to the Equation (3.8), the coherence lengths  $\xi_{F1}$  and  $\xi_{F2}$  vary with temperature. It is possible to go from the 0 state to the  $\pi$  state in a single junction by changing the period of the order parameter oscillation. Figure 3.7 shows that a diffusive SFS junction with barrier thickness  $d$  close to  $d_{\pi}^1$  could be a  $\pi$  junction at low temperatures, and a 0 junction at high temperatures. This effect should be maximized if  $E_{ex} \sim T_c$  (3.6). The temperature dependent transitions between the 0 and the  $\pi$  states were observed in the experiments by Ryazanov et al. [18] and by Sellier et al. [73] in  $Nb/CuNi/Nb$  junctions. The CuNi alloys had  $T_{Curie} \approx 30 - 60$  K.

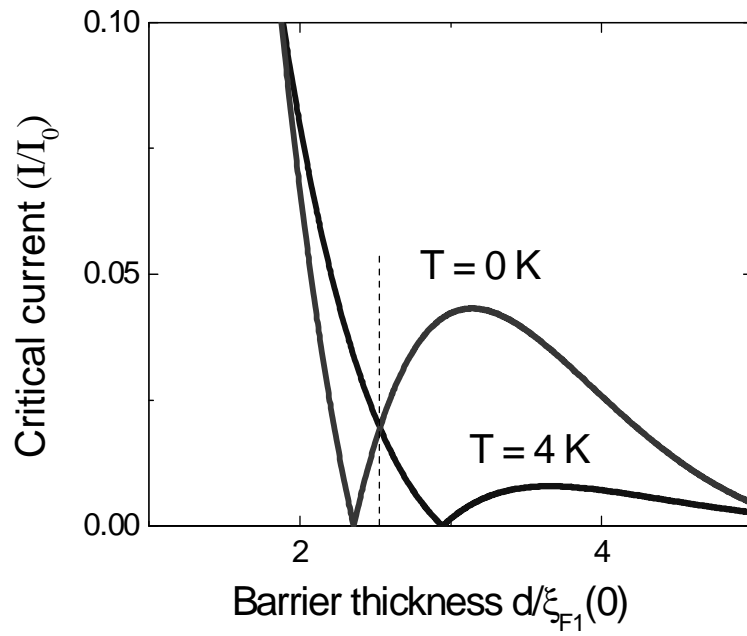


**Figure 3.7:** Thickness dependence of the critical current of SFS junctions at  $T=0$  K and at  $T=4$  K. Junction with thickness marked by a dashed line would be a  $\pi$  junction at zero temperature for  $T < T_\pi$  and a 0 junction at 4 K for  $T > T_\pi$ .

# Chapter 4

## Fabrication and Characterization of SFS Junctions

### 4.1 Magnetism of CuNi thin films

Crucial to the successful experimental observation [18] of the predicted oscillations of the Josephson critical current [15] as a function of barrier thickness in SFS junctions was the choice of a proper ferromagnetic material for the junction barrier. The best known ferromagnets are transition group metals Fe, Co and Ni. The exchange energies in pure transition metal ferromagnets range from 627 K for Ni to 1043 K for Fe, which correspond to the periods of the order parameter oscillations less than 1 nm. It is experimentally challenging to map out oscillations with such small periods, because roughness on the atomic scale can average out the effects of the oscillations. Also, it is difficult to grow continuous thin films of such a small thickness. However, several experiments recently attempted to look at the oscillations of the Josephson effect in SNFNS structures, in which a pure transition metal ferromagnet (Ni or Co) was sandwiched between the two normal metal spacers to form a tunneling barrier

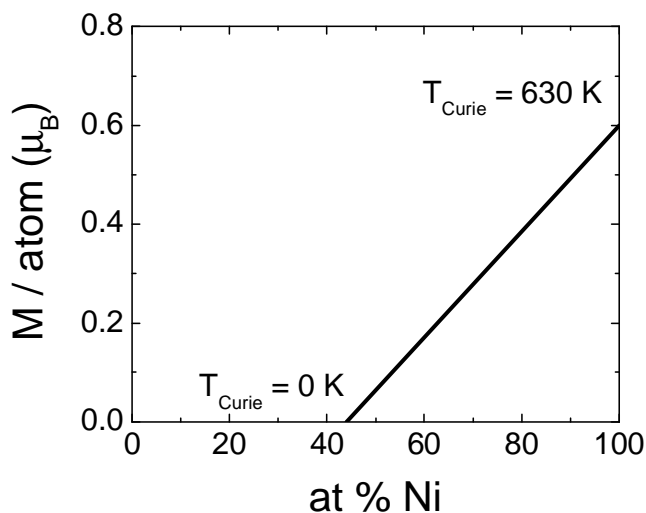


**Figure 4.1:** The spontaneous magnetic moment per atom in CuNi alloys as a function of Ni concentration.

[79; 80]. In this case the total barrier thickness becomes of order 10 nm. Both experiments showed that the critical currents are non-monotonic as a function of the ferromagnetic interlayer thickness, but the resolution was no more than 2-4 data points per oscillation period.

It is possible to lower the exchange energy by diluting a pure ferromagnet with a diamagnetic or a paramagnetic metal. So far, experiments in which Ni was alloyed with either diamagnetic Cu [18] or paramagnetic Pd [72] demonstrated transitions between 0 junction and  $\pi$  junction states in SFS junctions. Work in this thesis was done on Nb/CuNi/Nb Josephson junctions, therefore we shall briefly discuss ferromagnetism in CuNi alloys.

The ferromagnetism of Ni, Co and Fe is due to the exchange interaction between electrons in the partially filled 3d band hybridized with the 4s band. The bottom of the spin-up 3d subband is lower in energy than the bottom of the spin-down 3d subband, which results in unequal populations of these subbands, and gives the net magnetization. Cu and Ni are next to each other in the periodic table. The 3d

band of Cu is fully filled, therefore Cu is not a ferromagnet. Assuming that the band structures of Cu and Ni are the same, adding Cu to pure Ni fills up the 3d band, reducing the spin polarization and lowering the effective exchange interaction. Ferromagnetism is fully suppressed when 44 atomic % of Ni remain. Figure 4.1 shows the magnetic moment per atom in CuNi alloys as a function of Ni concentration. In pure nickel, each atom contributes  $0.6 \mu_B$  to the magnetization. The magnetization per atom drops linearly at a rate of  $0.01 \mu_B/\text{at.}\%$  Ni. The Curie temperature also changes linearly from  $\approx 630\text{K}$  at 100 % Ni to zero at 44 % Ni.

Copper and Nickel are known to form uniform alloys. As far as thin film deposition is concerned, Cu and Ni sputter at the same rate and with the same anisotropy. This means that the composition of a thin film of CuNi coincides with the composition of a bulk CuNi target that was used for the film deposition. We performed the Auger analysis to compare the compositions of thin CuNi films relative to the targets from which they were sputtered and found no evidence for differences in Ni concentration. It should be said that the Auger spectroscopy, just like any other spectroscopy, has a limited applicability in determining the composition of alloys of similar elements, because peaks of the elements that are close in the periodic table strongly overlap. However, spectroscopy can be very effective, with error  $< 1\%$ , in comparing the compositions of the two different sources of the same alloy. Cu and Ni also don't alloy with Nb, which means that the interfaces in Nb/CuNi/Nb sandwiches are sharp and the mutual diffusion region is narrow.

Spatial non-uniformities in composition on the scale of tens or hundreds of atoms may occur depending on the film growth conditions. If the films are deposited at elevated temperatures, atoms of Ni are mobile when they hit the substrate, and may prefer to cluster together, creating small regions of higher Curie temperatures. Figure 4.2 shows the residual magnetization of a 100 nm  $\text{Cu}_{0.49}\text{Ni}_{0.51}$  film as a function of

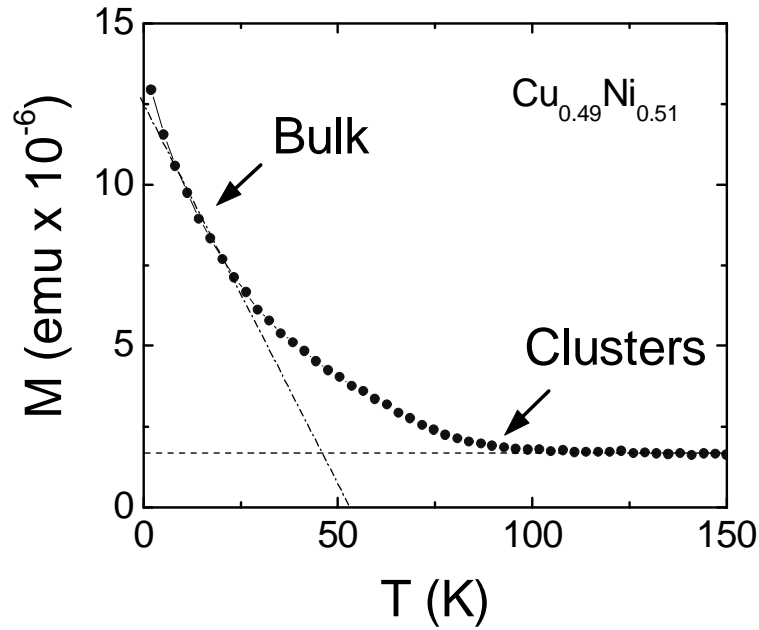


**Figure 4.2:** Residual magnetization of a  $\text{Cu}_{0.49}\text{Ni}_{0.51}$  film.

temperature. The magnetization decays rapidly as the temperature is increased from 2 K, but remains finite and small up to room temperature. Such behavior can be explained by the presence of Ni-rich clusters. The initial decay of magnetization corresponds to the ferromagnetic transition of the bulk of the film. The long tail in magnetization is due to clusters of Ni, for which  $T_{Curie}$  can be as high as 630 K, which is the Curie temperature of pure Ni. Some of the films that we made did not have any measurable residual magnetization at high temperatures, suggesting a more uniform composition.

The residual magnetization measurements were performed in a commercial Quantum Design Magnetic Properties Measurement (MPMS) system. This is an automated system with a 1 Tesla magnet which uses a SQUID coupled to a gradiometer coil to measure the absolute magnetic moment. The CuNi films were first cooled to the base temperature of  $\approx 2$  K. Next, the magnetic field was ramped up to 2000 Oe above the saturation field of the sample and then ramped down to zero. After this

procedure the ferromagnetic sample possesses residual magnetization. The decay of the residual magnetization was then monitored as a function of temperature. The Curie temperature for this film is estimated to be 40-60 K from this measurement. The temperature range of the magnetization decay is rather broad in the CuNi alloys, therefore other methods, such as neutron scattering, should be used in order to determine the Curie temperature with higher accuracy.

## 4.2 Fabrication procedures

Samples studied in this thesis were prepared in two laboratories - in the group of Professor Valery Ryazanov at the Institute of Solid State Physics in Chernologovka, Russia and in the group of Professor Dale Van Harlingen at the University of Illinois. In the process used in Chernogolovka, each layer of a SFS structure required a separate lithography (*layer-by-layer* technology), whereas in Urbana the SFS structure was deposited as a single trilayer without breaking the vacuum (*trilayer* technology). The differences in fabrication technologies and materials are outlined below and sketched in Figure 4.3.

In the *layer-by-layer* technology, junctions were prepared on a single crystal 15 mm square Si substrate coated with 100 nm of rf-sputtered  $Al_2O_3$ . The base Nb layer of thickness 110 nm was dc magnetron sputtered in  $6 \times 10^{-3}$  mbar of Ar. The Nb sputtering rate was 30 Å/s. Such a high sputtering rate ensures that the superconducting transition temperature  $T_c$  is close to that of the bulk, since fewer impurities get incorporated into the film. Both in films prepared in Russia and in Urbana the  $T_c$  was close to 9.1 K. The base superconducting electrode of the junction was then defined by light-field optical lithography and chemical etching of the Nb film in a mixture of hydrofluoric and nitric acids.

The ferromagnetic barrier of an SFS junction was a  $Cu_{0.47}Ni_{0.53}$  film rf-sputtered at a rate of 3 Å/s in  $4 \times 10^{-2}$  mbar of Ar. The base niobium film was rf-sputter cleaned before the deposition of CuNi. The thickness of the CuNi films varied between 8 and 27 nm. A layer of 20 – 30 nm of pure Cu was deposited on top of CuNi in order to protect CuNi during subsequent processing. A light-field photolithographic step followed by chemical etching in diluted  $FeCl_3$  shaped a  $75 \mu\text{m} \times 75 \mu\text{m}$  square CuNi/Cu barrier on top of the base Nb.

The junction area was defined by a window in an insulating SiO film. First, a square ranging from  $4 \mu\text{m} \times 4 \mu\text{m}$  to  $50 \mu\text{m} \times 50 \mu\text{m}$  in area was patterned by dark-field lithography on top of the CuNi/Cu barrier. Then, a 170-nm thick film of SiO was thermally evaporated. After this, liftoff in acetone was performed.

The junction was completed by dark field optical lithography, dc magnetron deposition of a 240-nm thick wiring Nb layer, and liftoff in acetone. The surface of CuNi/Cu film was sputter cleaned before the deposition of the top Nb wiring layer. Sputter cleaning removed approximately 10 nm of the protective Cu layer.

In the *trilayer* technology, the substrate was a 10 mm square cut from a single crystal Si wafer with 10000 Å of thermal oxide on top. After ion-mill cleaning of the substrate surface, a trilayer consisting of 100 nm of Nb, 10-30 nm of  $Cu_{0.50}Ni_{0.50}$  and 50 nm of Nb was dc sputtered in 15 mTorr of Ar. The niobium sputtering rate was 25 Å/s at a dc magnetron power of 150 W, and the CuNi sputtering rate was 2.5 Å/s at a power of 12 W. Note that no protective Cu layer is required in this technology. Then two photolithographic steps follow. The first one is used to define the junction area by etching the trilayer down to the base Nb layer in the entire wafer apart from where the junctions should be. The second lithographic step is to shape the base Nb layer. The photoresist used was AZ 5214 EIR.

First, light field optical lithography is used to define the photoresist squares rang-

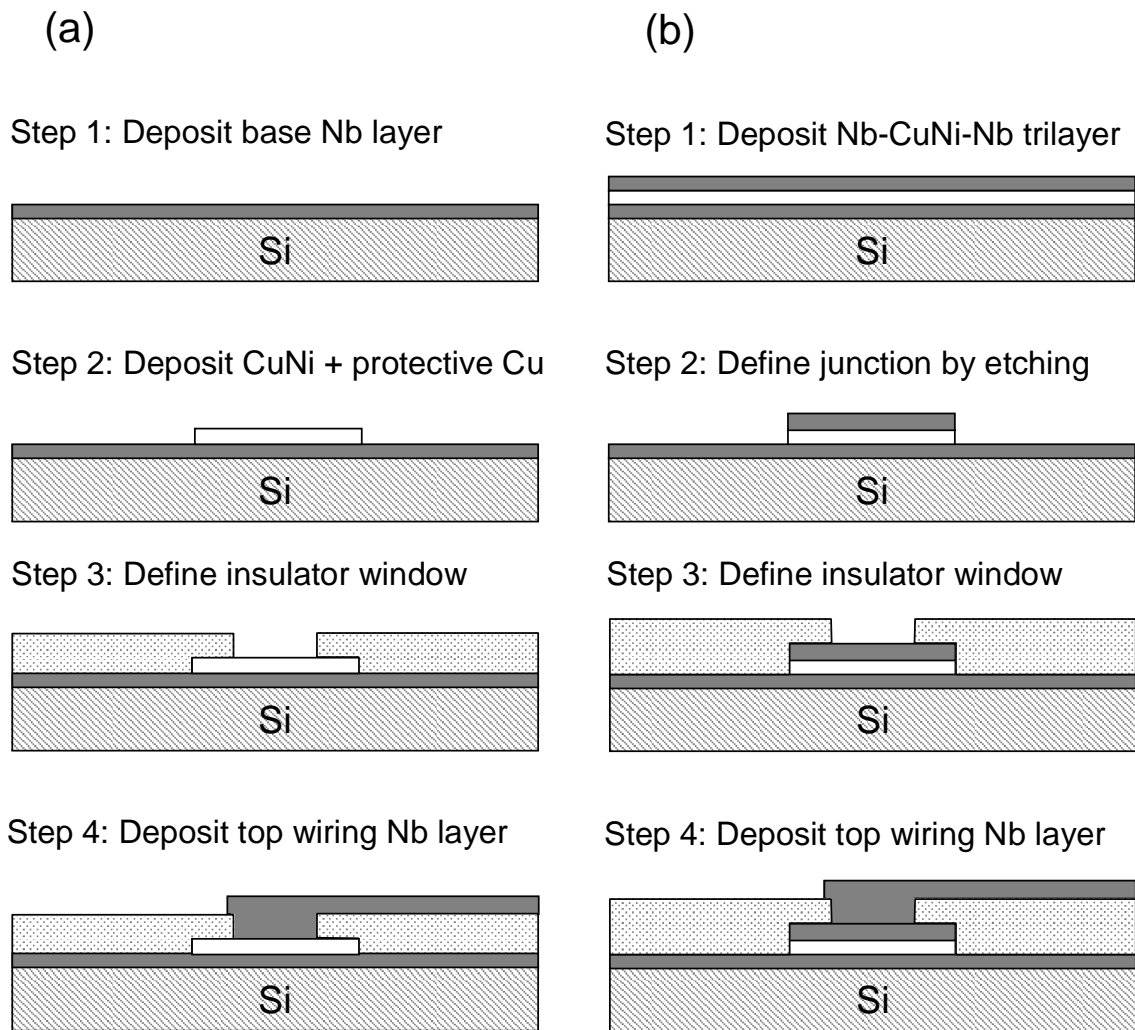


**Figure 4.3:** Sketch of (a) a layer-by-layer fabrication technology used in Chernogolovka (b) a trilayer technology used in Urbana.

ing from  $6\ \mu\text{m} \times 6\ \mu\text{m}$  to  $20\ \mu\text{m} \times 20\ \mu\text{m}$  in area on top of the Nb/CuNi/Nb trilayer. Then the top Nb layer of the trilayer is etched using Reactive Ion Etching (RIE) at 60 W in  $SF_6$  with 5 % oxygen. Since RIE does not etch CuNi, a step of ion milling at a rate of  $\approx 7\ \text{\AA}/\text{s}$  was performed to mill through the CuNi layer. At this point in the process, the entire surface of the substrate was covered with the base Nb film and the intact trilayer only remained in the junction areas. Then the second light field lithographic step was done to define the shape of the base Nb layer, after which the base Nb film was etched by RIE.

Next, the sample was patterned for liftoff to create a layer of insulation between the base and the top wiring Nb layers, which is a 150 nm thick film of  $SiO_2$  deposited by rf-sputtering. Windows of area  $4\ \mu\text{m} \times 4\ \mu\text{m}$  aligned with the trilayer islands in a dark field process were defined by the liftoff of the  $SiO_2$  film. A 100 nm thick top wiring Nb electrode was defined after a fourth step of optical lithography by dc magnetron sputtering and liftoff.

Both technologies described here can be used not only for fabrication of single SFS junctions for transport measurements, but also for fabrication of structures with one or more SFS junctions in multiply-connected geometries for phase-sensitive measurements. Phase-sensitive experiments require that the Josephson junction be a part of a superconducting loop. In order to create a superconducting loop, the base and the top superconducting electrodes in our fabrication processes can be designed to overlap. A window in the insulator must be placed in the overlap area to connect the layers.

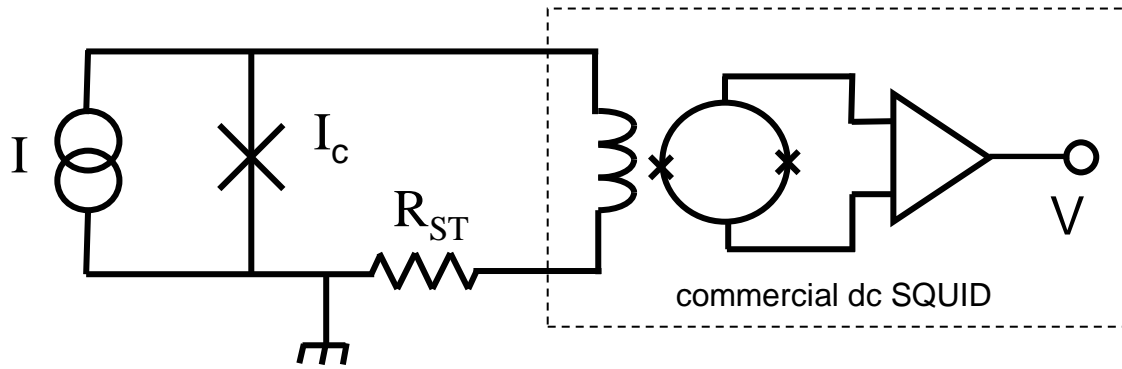


**Figure 4.4:** Diagram of a current-voltage characteristic measurement with a dc SQUID potentiometer.

### 4.3 Transport measurements procedure

The critical current of a Josephson junction can be deduced from its current-voltage characteristic (IV). IV characteristics can be measured by passing a current through the junction and measuring the voltage between the superconducting electrodes in the so-called transport measurement. The voltage across the junction is zero until the critical current is exceeded. Thermal noise may cause premature switching into the finite voltage state, for this reason the IV characteristic at finite temperature is rounded close to the switching point. The critical current can be recovered from a thermally rounded IV by proper fitting.

The characteristic voltages to be measured are given by the product of the critical current and the normal state resistance of the junction:  $V_c = I_c R_N$ . In SFS junctions that we study, the normal state resistance is roughly given by the resistance of the ferromagnetic interlayer and is in the range  $10 - 100 \mu\Omega$ , and the critical current varies from under  $1 \mu\text{A}$  to  $1000 \mu\text{A}$ . This gives  $V_c$  of  $10^{-11} - 10^{-7} \text{ V}$ . Therefore a voltmeter with picovolt resolution is required to measure the IVs.

The method that we use to measure such small voltages is based on the ability of SQUIDs to detect very small changes in magnetic flux on the order of  $10^{-5} - 10^{-8} \Phi_0$ .

A diagram of a SQUID potentiometer is presented in Figure 4.4. An SFS junction of critical current  $I_c$  is connected in parallel with a temperature-independent standard resistor  $R_{ST} \approx 10 \text{ m}\Omega$ . If the junction is in the supercurrent state, all the current applied from the current source  $I$  flows through the junction. When  $I > I_c$ , part of the current flows through  $R_{ST}$  so that the voltages across the resistor and the junction are equal. In the limit  $R_{ST} \gg R_N$ , the current flowing through  $R_{ST}$  is small, and it can be assumed that the current flowing through the junction is equal to  $I$ . In this limit, the small current flowing through  $R_{ST}$  is proportional to the voltage drop across the junction. This current can be detected by a dc SQUID inductively coupled to the loop containing  $R_{ST}$ . We used a commercial Quantum Design dc SQUID as a current detector mutual inductance  $\approx 0.2 \mu\text{A}/\Phi_0$ , meaning that  $0.2 \mu\text{A}$  of current through the SQUID input inductance generate 1 flux quantum in the SQUID loop. The dc SQUID is operated in a feedback mode, in which the magnetic flux in the SQUID loop is compensated by the current applied to the modulation coil (not shown in the diagram). The output voltage of the SQUID is proportional to the current required to zero the flux in the SQUID loop with a transfer function of  $0.6 - 0.8 \text{ V}/\Phi_0$ .

In order to minimize the stray resistance in the potentiometer loop, superconducting Nb/Ti wire is used to connect the sample to the brass foil standard resistor and to the terminals of a dc SQUID input coil. The resistivity of dirty brass saturates below  $T \approx 20 \text{ K}$ , which makes brass a suitable material for standard resistors. Press-on indium contacts are used to connect the wires to the sample pads. Measurements were performed in a  $^4\text{He}$  cryostat. The  $^4\text{He}$  bath could be pumped to reach a base temperature of 1.2 K. The sample was mounted on a Cu block with a heater inside a vacuum can, which allowed us to change the temperature above that of the helium bath. The dc SQUID sensor was placed outside the vacuum can in the helium bath, to insure the stability of the SQUID when the temperature of the sample is changed

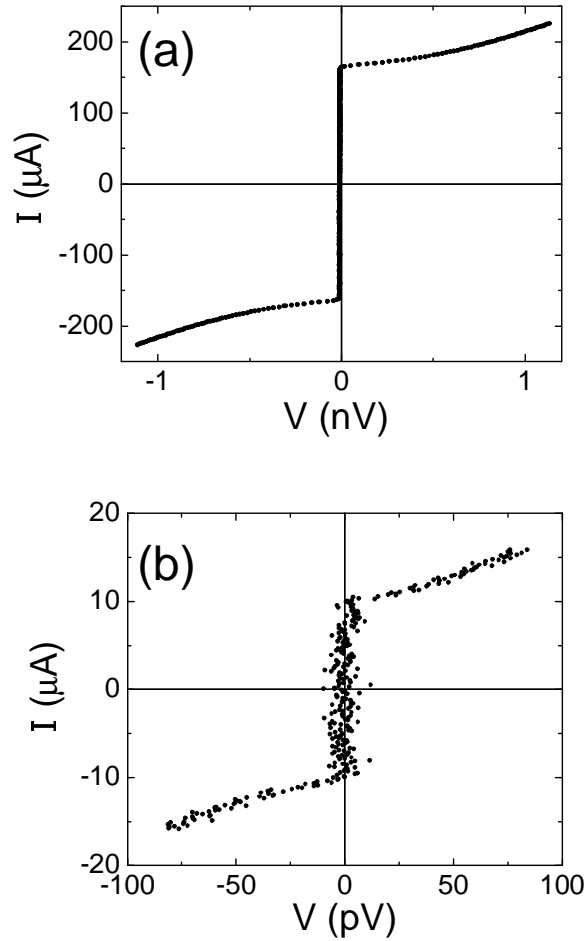


**Figure 4.5:** Current-voltage characteristics measured with a SQUID potentiometer of (a) a junction prepared using the trilayer technology with barrier thickness  $d \approx 17$  nm at  $T = 4.2$  K and (b) a junction prepared via a layer-by-layer technology with barrier thickness  $d \approx 22$  nm at  $T = 1.4$  K.

inside the vacuum can.

Typical IVs obtained with a SQUID potentiometer are presented in Figure 4.5. Panel (a) shows an IV of a  $10\ \mu\text{m} \times 10\ \mu\text{m}$  SFS junction prepared via the trilayer technology with barrier thickness  $d \approx 17\ \text{nm}$  at  $T = 4.2\ \text{K}$ . The characteristic voltage is on the order of  $1\ \text{nV}$  and the critical current  $I_c \approx 175\ \mu\text{A}$ . Panel (b) shows an IV of a layer-by-layer  $50\ \mu\text{m} \times 50\ \mu\text{m}$  SFS junction with  $d \approx 22\ \text{nm}$  at  $T = 1.4\ \text{K}$ . The critical current is on the order of  $10\ \mu\text{A}$ , and the characteristic voltage is  $100\ \text{pV}$ . This graph shows that the resolution of our SQUID potentiometer is on the order of  $10\ \text{pV}$ , as deduced from the voltage noise in the supercurrent state of the junction. The minimum critical current that can be resolved in this setup is  $\approx 0.5 - 1\ \mu\text{A}$ .

## 4.4 Critical current vs. barrier thickness

The barrier thickness dependence of the critical current can be mapped out by measuring IVs of many SFS junctions with different barrier thicknesses at a fixed temperature. Figure 4.6 shows the dependence of the critical current density, which is the critical current divided by the area of the junction, on the barrier thickness for junctions prepared using the layer-by-layer and the trilayer technologies.

In Figure 4.6(a) the barrier thickness dependence of the critical current density at  $T = 4.2\ \text{K}$  is demonstrated for junctions fabricated using the layer-by-layer technology with  $\text{Cu}_{0.47}\text{Ni}_{0.53}$  barriers. This data was obtained in the group of Professor Ryazanov in Chernogolovka. On a logarithmic scale, the data exhibits two sharp dips at thicknesses  $11\ \text{nm}$  and  $22\ \text{nm}$ . At  $d = 11\ \text{nm}$  the transition from the  $0$  state to the  $\pi$  state occurs as the thickness is increased. A thickness of  $d = 22\ \text{nm}$  marks the transition back to the  $0$  state. We shall call  $d = 11\ \text{nm}$  and  $d = 22\ \text{nm}$  the first and the second nodes of  $J_c(d)$ .

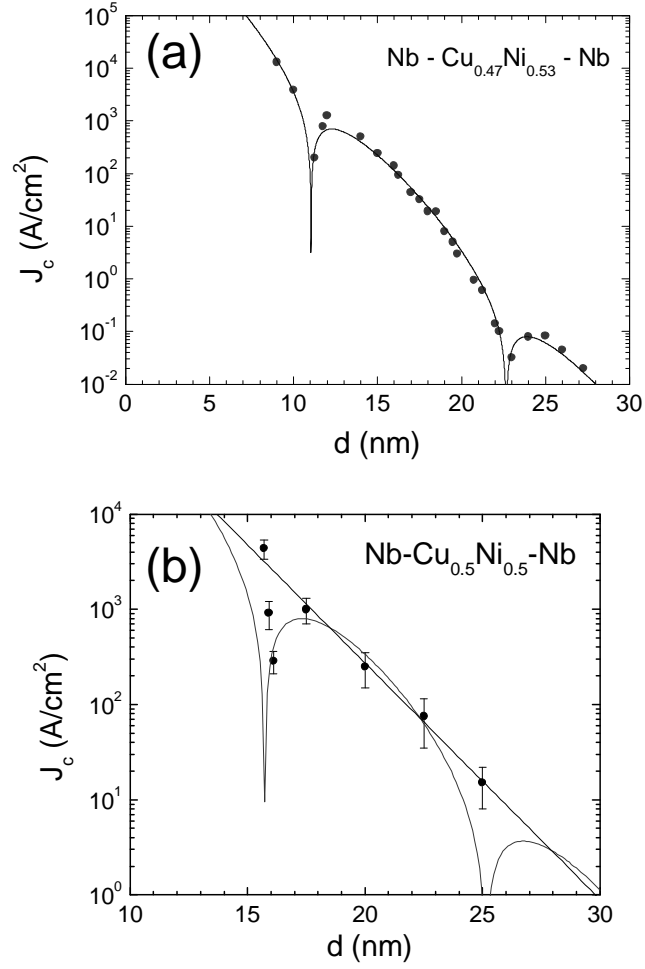


**Figure 4.6:** Critical current density as a function of the ferromagnetic barrier thickness in SFS junctions prepared via (a) the layer-by-layer technology and (b) the trilayer technology. Both sets of data are fitted using the Equation 3.10. Panel (b) also shows the fit to the regular exponential decay (straight line).

The solid line in Figure 4.6(a) is the fit of the data to the Equation (3.10). From this fit the junction parameters can be extracted. The characteristic lengths of the order parameter decay  $\xi_{F1} = 1.3$  nm, and of the order parameter oscillation  $\xi_{F2} = 3.7$  nm. Such a large discrepancy between the two values cannot be accounted for only by the effect of temperature described by the Equation (3.8). Some inelastic scattering must be assumed to explain why  $\xi_{F1}$  is smaller than  $\xi_{F2}$ . Spin-orbit scattering provides one source of such inelastic processes, but it is not believed to be strong in dilute CuNi alloys. Another possible scattering mechanism is the spin-flip scattering on Ni rich clusters that were discussed earlier in this Chapter.

The critical current density at zero barrier thickness deduced from the fit is  $J_c(d=0) = 10^6$  A/cm<sup>2</sup>, and is somewhat smaller than that for the bulk Nb. This could be attributed to the reduced interface transparency in the junctions made via the layer-by-layer technology, where each layer of the junction is deposited in a separate vacuum cycle, allowing for surface contamination. However, the lower value for  $J_c(0)$  deduced from the fit can also be caused by many other factors. In thin polycrystalline superconductors, the critical current density may be lower. The presence of a 10 nm normal layer of Cu on top of CuNi in the layer-by-layer junctions may result in a small suppression of  $J_c(0)$ . The fit also requires an offset in the barrier thickness  $d_0 = 4$  nm. The nature of this offset is not clear. Effectively, it means that there exists a 4 nm thick magnetically “dead” layer with exchange energy  $E_{ex} = 0$ . It is possible that the diffusion of Ni into Nb leads to a reduced magnetism in the vicinity of the SF interface. It is also a possibility that the exchange interaction is suppressed in thinner ferromagnetic films due to the band nature of the exchange interaction or other factors.

Figure 4.6(b) shows the thickness dependence of the critical current for trilayer SFS junctions fabricated in Urbana. This data has one node at  $d = 16$  nm. The

order parameter decay length extracted from the exponential fit is  $\xi_{F1} = 1.75$  nm. The estimated oscillation length  $\xi_{F2} = 3$  nm and the critical current density at zero thickness  $J_c(d = 0) = 2 \times 10^7$  A/cm<sup>2</sup>. More samples are required in order to do a more accurate analysis.

The results obtained from both technologies are similar. Therefore, it is unclear at the moment if the trilayer technology has higher potential for possible applications of  $\pi$  junctions, for which higher  $I_c R_N$  products are desired. In particular, the maximal  $J_c$  in the  $\pi$  state is  $\approx 1000$  A/cm<sup>2</sup> in both technologies. Both results also agree with the thickness dependence obtained in the experiments by Sellier et al. [73] on SFS junctions with  $Cu_{0.52}Ni_{0.52}$  barriers and Nb as a superconductor.

## 4.5 Critical current vs. temperature

For barrier thicknesses at least 1-2 nm away from any nodes, the critical currents of our SFS junctions increase monotonically as the temperature is lowered. If the barrier thickness is chosen close to a node of the  $I_c(d)$  dependence, temperature can drive transitions between the 0 junction and the  $\pi$  junction states. For this case, the temperature dependence of the critical current is shown in Figure 4.7. The critical current becomes non-monotonic as a function of temperature. As the temperature is lowered from  $T_c$ ,  $I_c$  may exhibit a maximum and start to decrease. There may exist a temperature  $T_\pi < T_c$  at which the critical current  $I_c$  reaches zero. The temperature  $T_\pi$  marks the transition between 0 and  $\pi$  states.

For junctions prepared near the first node of  $I_c(d)$ , the critical current density changes by 100 A/cm<sup>2</sup> per 1 K change in temperature. Near the second node, this rate is much lower, on the order of 0.1 A/cm<sup>2</sup> per 1 K. It is not possible to observe two temperature driven 0- $\pi$  transitions in one junction. The change in the effective

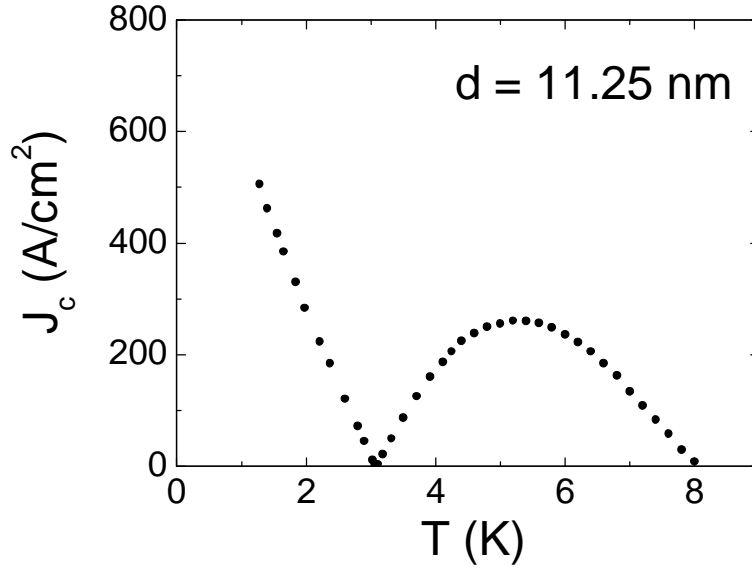


**Figure 4.7:** Critical current density vs. temperature for a Nb/Cu<sub>0.47</sub>Ni<sub>0.53</sub>/Nb SFS junction exhibiting a transition from the 0 state at higher temperatures to the  $\pi$  state below  $T_\pi \approx 3.2$  K. Data obtained in the group of Prof. Ryazanov.

barrier thickness due to the change in the order parameter oscillation period in the temperature interval from 0 to 10 K is on the order of 1 nm, whereas a change in thickness on the order of 10 nm separates the nodes of the  $I_c(d)$  dependence (see Figure 4.6).

Remarkably, the  $\pi$  state of an SFS Josephson junction was first identified through the transport measurements of the temperature dependence of the critical current [18]. Even though this type of measurements does not reveal the sign of the critical current, the existence of a node at  $T_\pi$  in the  $I_c(T)$  dependence is a strong indication of the  $\pi$  state, since it cannot be simply explained by any other factors. Junctions exhibiting nodes in the  $I_c(T)$  dependence that are studied in this thesis in Chapters 5, 6 and 8 were fabricated in Chernogolovka using a layer-by-layer technology.

Behavior similar to that shown in Figure 4.7 was observed in SFS junctions with spatial non-uniformities in the barriers. The critical current may also reach zero in these junctions, however not at the temperature of a 0- $\pi$  transition. In non-

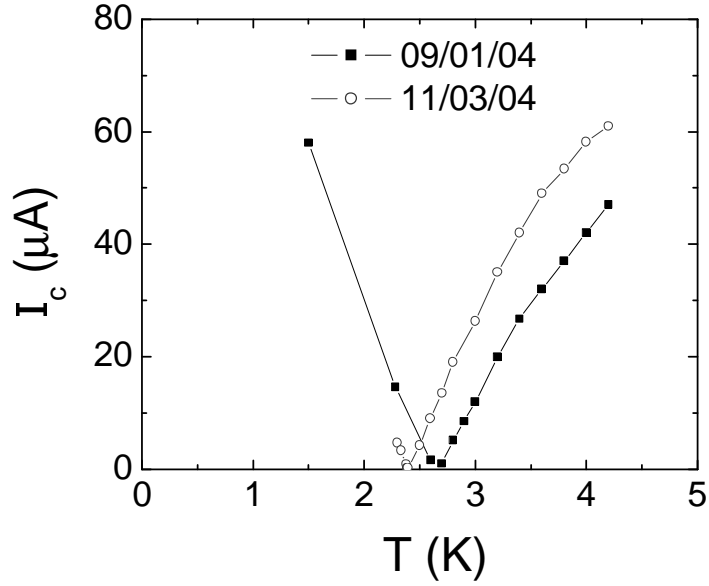


**Figure 4.8:** Critical current vs. temperature for a  $4\mu\text{m} \times 4\mu\text{m}$  Nb/Cu<sub>0.47</sub>Ni<sub>0.53</sub>/Nb SFS junction with  $d = 11$  nm. As a result of room temperature annealing, the curve is shifted by  $\approx 0.25$  K to lower temperatures in a measurement done 2 months later.

uniform junctions fabricated close to a node of  $I_c(d)$ , parts of the junctions transition into  $\pi$  state at different temperatures. The average critical current density in  $0-\pi$  junctions reaches zero at a temperature at which the critical current of the  $0$  region in the junction is canceled by the opposite sign critical current of the  $\pi$  region. The temperature evolution of  $0-\pi$  junctions is discussed in detail in Chapter 6.

Materials properties of CuNi barriers have an intriguing influence on the temperature dependence of the critical current. If an SFS junction is annealed at an elevated temperature, the zero of the critical current shifts to a lower temperature. This indicates that annealing lowers the exchange interaction in the ferromagnet. The most likely explanation of this behavior is the diffusion of Ni atoms. As was noted earlier in this Chapter, Ni atoms have a tendency to cluster. As more and more atoms of Ni form clusters, the bulk exchange interaction of CuNi decreases. The diffusion rate is increased at higher temperatures, this is why annealing plays a role.

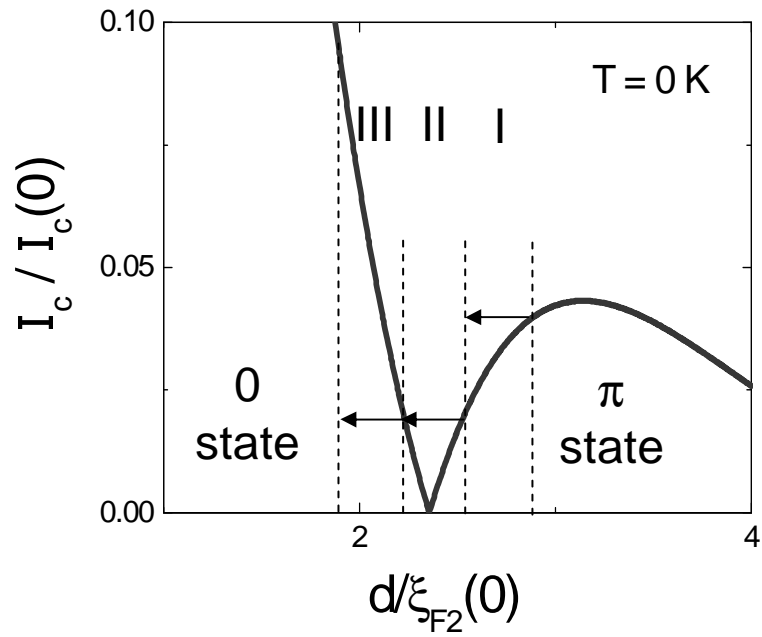


**Figure 4.9:** Diagram of the critical current of an SFS junction as a function of the effective barrier thickness. Annealing increases the order parameter oscillation length  $\xi_{F2}$ , at the same time decreasing the effective thickness. Three situations are shown: I) the critical current at zero temperature decreases after annealing II) the critical current remains the same after annealing III) the critical current increases after annealing.

In junctions near the first node of the  $I_c(d)$  dependence, it is possible to observe the effects of diffusion that occur even at room temperature. Figure 4.8 shows two  $I_c(T)$  curves from the same SFS junction measured approximately two months apart. The temperature of zero critical current has shifted by  $\approx 0.25$  K, an average rate of 4 mK / day. In other junctions, an average rate of change in  $T_\pi$  was observed to be as high as 10 mK / day. The zero of the critical current always shifts to lower temperatures and will become unaccessible experimentally with time. It should be noted that junctions fabricated near the second node of  $I_c(d)$  are less susceptible to room temperature annealing, and the value of  $T_\pi$  may remain virtually unchanged for years unless the sample is heated. The effects of annealing were seen in junctions fabricated both in Urbana and in Chernogolovka. The substantial impact of room temperature annealing on the critical current of SFS junctions near the first node of  $I_c(d)$  could be related to the ferromagnetic barrier non-uniformities described in Chapter 6.

Annealing can be used as a crude test of the  $\pi$  junction state. Figure 4.9 illustrates the effect of annealing in the critical current vs. effective barrier thickness  $d/\xi_{F2}(0)$  diagram. If the critical current at a given temperature was reduced by annealing, the junction was in the  $\pi$  state before annealing. If the critical current was increased, the junction could either be in the 0 state or the annealing was done for too long and the junction has surpassed the entire node region, in which the critical current density is suppressed due to the oscillations of the order parameter.

## Chapter 5

# Phase-Sensitive Experiments on Uniform SFS Junctions

In Chapter 1 we defined the sign of the critical current with respect to the direction of supercurrent for a small and positive phase difference across the junction. This means that in order to determine the sign of the critical current, which is essential for the confirmation of a  $\pi$  junction state, one is required to measure and control the superconducting phase. Transport measurements described in the previous Chapter do not contain information about the phase difference, therefore the sign of the critical current cannot be determined from a measurement such as the measurement of a current-voltage characteristic. A natural way to achieve controllable phase bias is to incorporate a junction to be tested in a superconducting loop. In this case, the phase drop across a Josephson junction is related to the magnetic flux in the loop by the fluxoid quantization condition. By changing the magnetic flux in the superconducting loop one can change the Josephson phase (see Chapter 2.1), and by measuring the magnetic flux threading the superconducting loop one can determine the Josephson phase difference. Measurements that reveal the information about the

superconducting phase are known as “phase-sensitive”.

Measurement of the current-phase relation is phase-sensitive by definition. But there are also other types of experiments that can be categorized as phase-sensitive. For example, the observation of spontaneous magnetic flux in superconducting loops with Josephson junctions or shifts in the critical current vs. applied magnetic flux patterns can serve as an indication of a phase shift of  $\pi$  due to either an unconventional symmetry of the order parameter [26], or due to  $\pi$  junctions (see Chapter 2).

In this thesis, we discuss experiments aimed both at the determination of the current-phase relation of SFS junctions and at the observation of spontaneous flux in superconducting loops containing SFS junctions in the  $\pi$  state. The goal of this work is to determine the sign of the critical current in the  $\pi$  junction regime, and to search for secondary Josephson tunneling, that should, according to a number of theoretical predictions, dominate the current-phase relation close to the transitions between 0 and  $\pi$  junction states. Measurements presented in this Chapter are done on SFS junctions with uniform barriers. In uniform junctions, measurement of the current-phase relation contains information about the local character of the CPR, including the possible higher harmonics. However, spatial variations in the barrier thickness, composition or interface transparency may lead to a partial transition of an SFS junction into a  $\pi$  junction state. The interpretation of the current-phase relation measurement for such 0- $\pi$  junctions is not straightforward, because signals of higher order periodicity, which mimic a local  $\sin(2\phi)$  component in the CPR, may appear in the data due to a mixing of current-phase relations of 0 and  $\pi$  regions within the junction. Non-uniform SFS junctions are discussed in the next Chapter.

## 5.1 Measurement technique

The first direct measurements of the current-phase relation were done by Jackel, Buhrman and Webb [81] and Waldram and Lumley [82], who used the dc technique, and by Rifkin and Deaver [45] who implemented the rf technique that was proposed earlier by Silver and Zimmerman [83].

Measurements done using the dc technique consist of monitoring the magnetic flux induced in an rf SQUID as a function of the applied magnetic flux. This method was explicitly used by Jackel et al. [81]. They used a fitting procedure in order to subtract a linear response due to an inductance of the loop. Our own technique is also a modification of this approach. Experiments by Waldram and Lumley [82] were performed in the feedback mode in which the applied magnetic flux  $\Phi_{ex}$  was compensating the magnetic flux induced in the rf SQUID loop by the Josephson junction bias current  $I$  using a separate SQUID as a null-detector. With the detector SQUID at zero, the current-phase relation was simply given by  $I = I(2\pi\Phi_{ex}/\Phi_0)$ .

In the rf technique the rf SQUID is coupled to a tank LC-circuit which is excited at an rf frequency. The dynamic inductance of the rf SQUID is then recorded as a function of the applied magnetic flux. The current-phase relation can be extracted from this type of data after a mathematical transformation. This technique has recently been extensively reviewed by Golubov, Kupriyanov and Il'ichev [40]. It appears to the present author to be less straightforward and less elegant than the dc technique.

A diagram illustrating the principle of our current-phase relation experiment is shown in Figure 5.1. A current  $I$  applied to the superconducting loop containing a Josephson junction splits between the junction and the inductor  $L$ . If a sample is designed in such a way that the geometric inductance  $\ell$  in the junction arm is small,

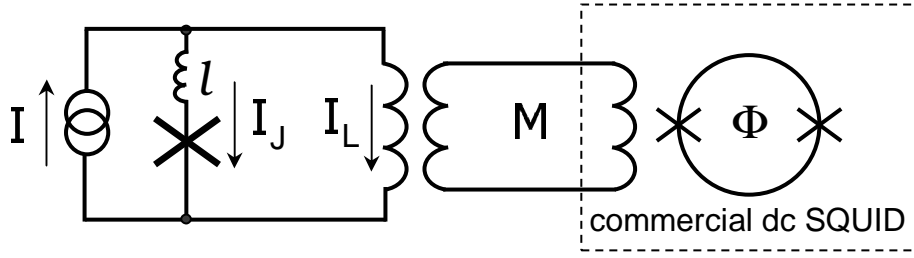


**Figure 5.1:** A diagram of the measurement of the current-phase relation.

$\ell \ll L$ , the superconducting phase drop across the inductor  $L$  is equal to the phase drop across the junction. In this limit, the bias current  $I$  splits according to:

$$I = I_L + CPR \left( \frac{2\pi I_L L}{\Phi_0} \right) = \frac{\Phi}{L} + CPR \left( \frac{2\pi \Phi}{\Phi_0} \right), \quad (5.1)$$

where  $\Phi$  is the flux induced in the superconducting loop by the current  $I_L$ . Flux  $\Phi$  can be monitored by a dc SQUID detector coupled to the inductor  $L$  via a mutual inductance  $M$ . From the measurement of  $I(\Phi)$ , the  $CPR(\Phi)$  can be extracted.

Schematically, this measurement setup is very similar to the SQUID potentiometer circuit that we used for transport measurements (see Figure 4.4). Both measurements use a commercial Quantum Design dc SQUID. The main difference is that the standard resistor is absent in the setup shown in Figure 5.1, since the superconducting coherence around the loop is essential for the measurement of the current-phase relation. There are also differences in the sample geometry. The design and the micrographs of the actual sample that was used to do the current-phase relation measurements in SFS junctions near the second node of  $I_c(d)$  with  $d = d_\pi^2 = 22$  nm are shown in Figure 5.2.

The device consists of two superconducting loops that share a  $50 \times 50 \mu\text{m}^2$  SFS Josephson junction (Figure 5.2(a)). The upper loop is used to couple magnetic flux from the lower loop into the dc SQUID detector. In order to do that, a 30-turn superconducting coil is glued on top of the flux transformer which is shaped in the

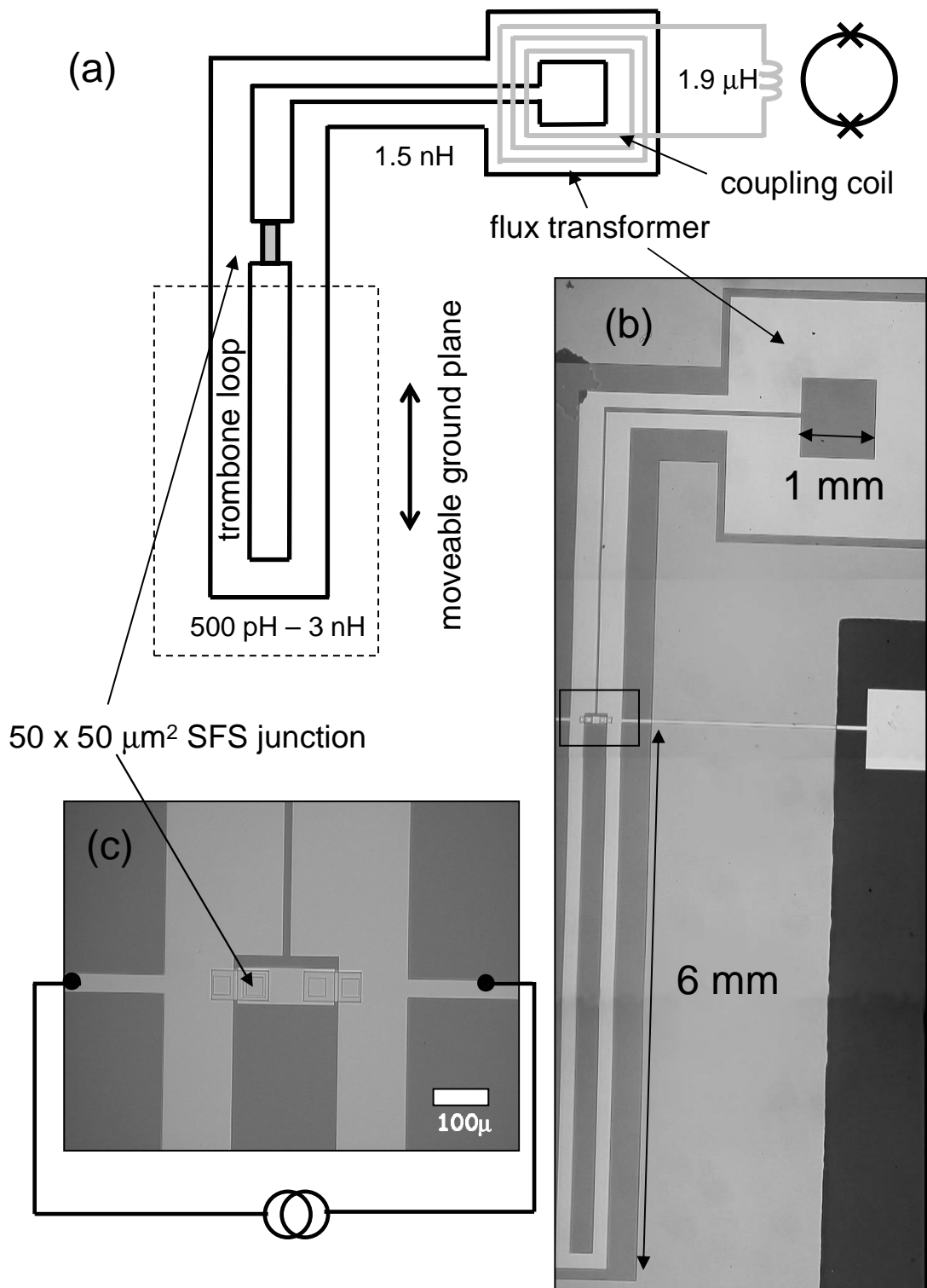


**Figure 5.2:** (a) Design of a sample that was used for the measurement of the current-phase relation and the micrographs of (b) the entire sample and (c) of the junction area.

form of a  $1 \text{ mm}^2$  planar washer. This coupling coil connects to the input terminals of the dc SQUID sensor. The number of turns in the coupling coil was determined from the matching condition of the inductance of the planar washer flux transformer  $L_W = 1.2 \text{ nH}$  and the inductance of the dc SQUID input coil  $L_S = 1.9 \text{ } \mu\text{H}$ . The optimal inductance of the coupling coil  $L_C$  is then given by the geometric mean  $L_C = \sqrt{L_W L_S} \approx 47 \text{ nH}$ .

The inductance of the lower loop can be adjusted *in situ* by moving the superconducting ground plane shield over it. In order to have the ability to change the inductance substantially, at least by an order of magnitude, the lower loop is extended to  $6 \text{ mm}$  in length. As a result, the inductance of this loop can be varied in the range  $\approx 500 \text{ pH} - 3 \text{ nH}$ . The spacing between the superconducting shield and the loop was estimated to be  $10 \text{ } \mu\text{m}$ .

Owing to the moving shield, this setup was nicknamed “the trombone”, it was originally proposed for studying spontaneous magnetic flux in loops containing the corners of the d-wave crystals [84]. As was shown in Chapter 2, in a superconducting loop with a  $\pi$  junction, spontaneous currents onset when the loop inductance parameter  $\beta_L$  exceeds the  $\beta_L = 1$  threshold. By moving the ground plane towards the fully open position (Figure 5.2(a)), one can in principle observe spontaneous currents turning on as the lower loop crosses the  $\beta_L = 1$  point. For this sample, the  $I_c$  should be on the order of  $0.1 \text{ } \mu\text{A}$  for the spontaneous current onset point to be in the inductance range between the ground plane fully closed and fully open. This is not a problem, since the critical current of an SFS junction can be made very small close to a  $0-\pi$  transition by adjusting the temperature. If the junction in the device is a conventional  $0$  junction, no signal will be observed as the inductance is changed. If the junction is a  $\pi$  junction, a characteristic response shown in Figure 2.4(a) will be observed as a function of the ground plane position. Complications with the obser-

variation of this effect related to the residual magnetic fields present in the cryostat are discussed in the last section of this Chapter.

Bias current  $I$  can be applied to the device through the current leads (Figures 5.2(b) and 5.2(c)). The current-phase relation can then be extracted from the  $I(\Phi)$  characteristics using the Equation (5.1), in which the inductance of the trombone and the flux transformer loops in parallel should be used for  $L$ . The information about the entire CPR is only accessible in the regime  $\beta_L < 1$ , when the rf SQUID is not hysteretic.

Figure 5.3(a) shows the measurements of the rf SQUID characteristics of the trombone sample in the temperature range 3.5 K to 4.2 K. At  $T = 4.2$  K the trombone rf SQUID is hysteretic, suggesting  $\beta_L > 1$ . Comparison to the simulated rf SQUID characteristics in Figure 5.3(b) suggests that  $\beta_L \approx 5$  at  $T = 4.2$  K. In this experiment the inductance of the trombone loop was kept constant, so the average slopes of all curves in Figure 5.3(a) are the same. As the temperature is lowered, the hysteretic portions of the curves become smaller, with the noticeable hysteresis disappearing completely at  $T \approx 3.7$  K. This behavior indicates that  $\beta_L$  and the critical current decrease when the temperature decreases, meaning that the junction is very close to a  $0-\pi$  transition. In fact this junction has a  $T_\pi$  of 3.59 K as will be shown later in the discussion of the CPR data. Note that the flux axis in Figure 5.3(a) is self-calibrating, since each period corresponds to a change in the induced flux by one flux quantum  $\Phi_0 \approx 2 \times 10^{-15}$  Wb. Given this, the inductance  $L$ , which is the average slope of a trombone rf SQUID characteristic, can be estimated at  $\approx 1.28$  nH for this data that was taken with the trombone loop fully covered by the ground plane.

In Figure 5.3(a) one can also notice a spread in the sizes of the hysteresis loops due to the thermal switching of the rf SQUID between the adjacent fluxoid states. Because the critical current of this junction is very small, on the order of  $1.5 \mu\text{A}$  at

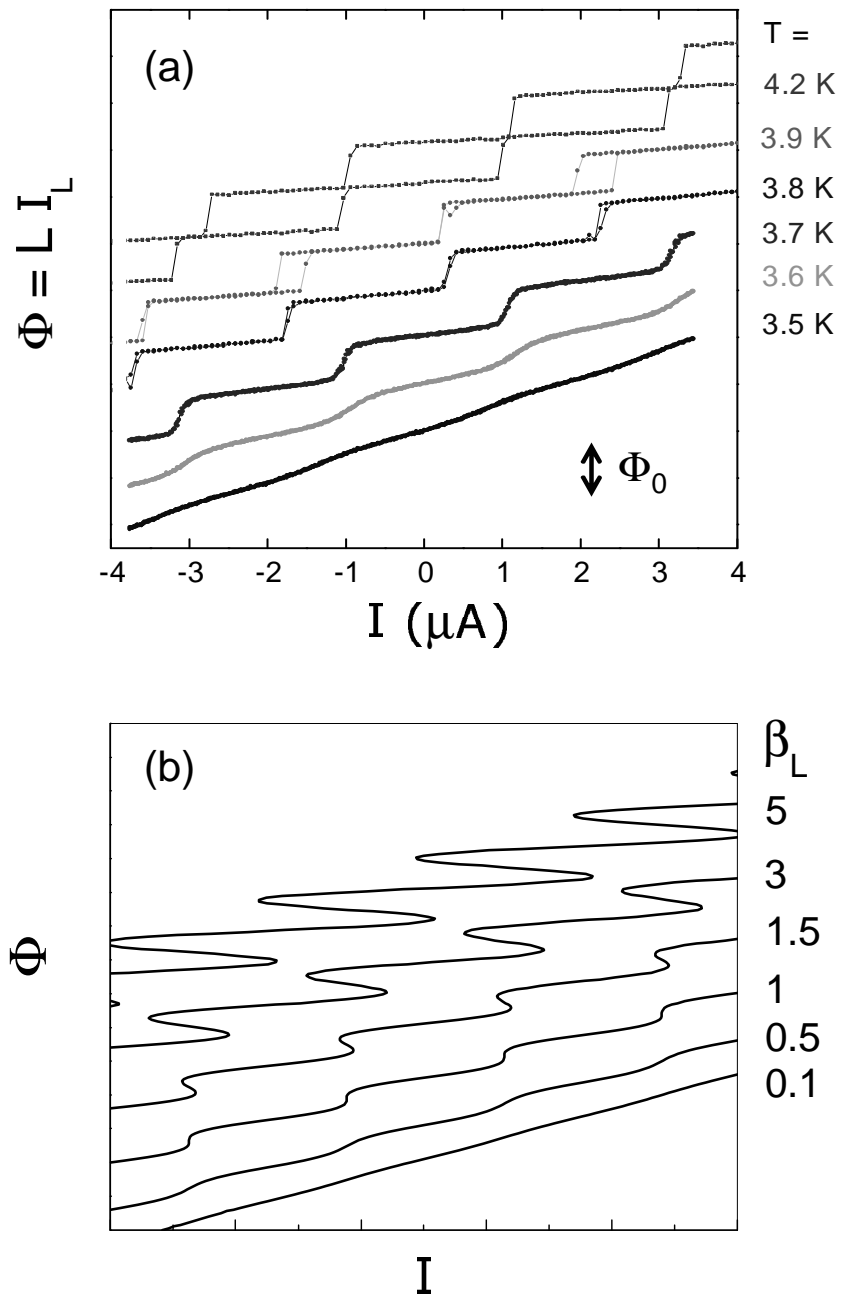


**Figure 5.3:** (a) Measurement of the magnetic flux in the flux transformer  $\Phi$  vs. the bias current  $I$  for the trombone sample at different temperatures (b) Simulations of the rf SQUID characteristics for a range of  $\beta_L$  values.

$T = 4.2$  K, the Josephson energy of the junction is comparable to the thermal energy  $k_B T$ . This allows the Josephson phase to overcome the Josephson potential barrier. Thermal fluctuations in the rf SQUID loop can influence the measurement of the CPR, reducing the measured value of the critical current and changing the shape of the apparent current-phase relation [40; 81; 85]. The shape of the apparent CPR can be altered due to thermal fluctuations because the Josephson potential well is not symmetric at finite bias. In such a well, thermal fluctuations supply random kicks to the phase difference, but the phase difference spends more time on the flatter side of the well. The average phase difference that is measured in any experiment is therefore shifted from the equilibrium phase difference. Due to this effect the position of the phase difference corresponding to the maximal supercurrent  $\phi_{max}$  can be shifted to lower values. In an rf SQUID, the effects of thermal fluctuations in the magnetic flux threading the loop should be taken into account. The magnetic flux fluctuations come from the fluctuations of the superconducting phase and can be estimated from the value of the fluctuation inductance  $L_f = (\Phi_0/2\pi)^2/k_B T$  [40]. If  $L \ll L_f$ , thermal fluctuations in the magnetic flux can be neglected. At  $T = 4.2$  K  $L_f \approx 1.7$ nH. The reduction in the critical current due to magnetic flux fluctuations can be estimated from [40]:

$$I_c \rightarrow I_c \exp\left(-\frac{L}{2L_f}\right). \quad (5.2)$$

In our case, the apparent critical current is  $\approx 3/4$  of the thermodynamic value. Even though the scale of the rf SQUID energy is comparable to thermal energy, the non-linearities in the rf SQUID characteristics can be clearly observed. Thermal fluctuations would not obscure the observation of the sign change in the CPR which corresponds to a phase shift of  $\pi$  in the rf SQUID modulation (see Figure 2.2), neither would they change the period of the CPR which should become one half the regular

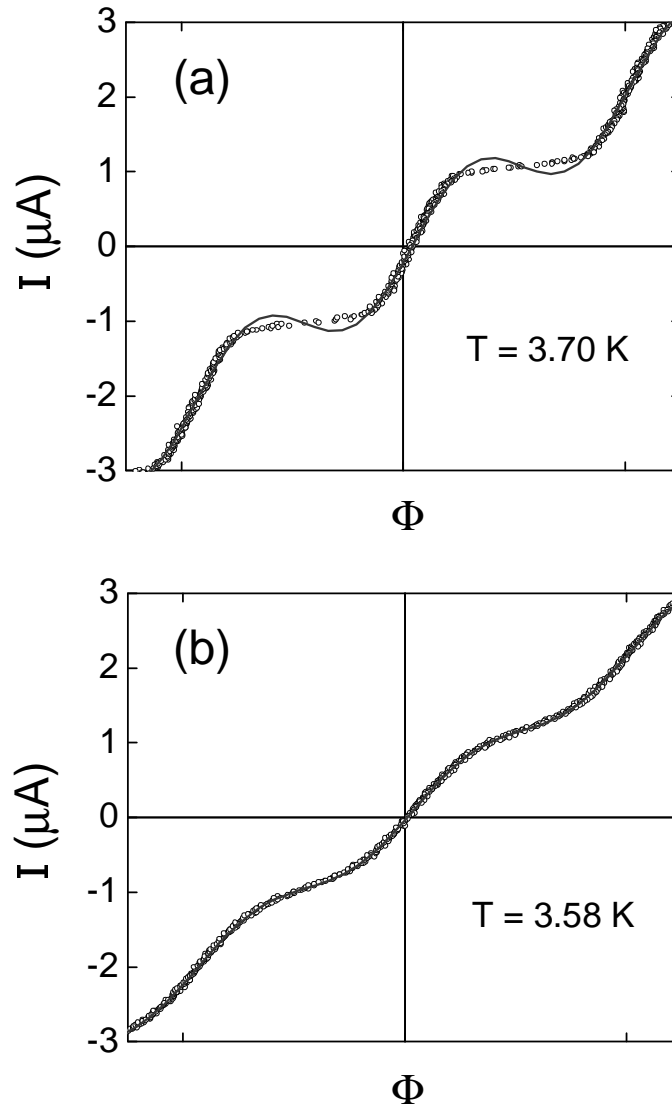


**Figure 5.4:** Data and the best fit of trombone rf SQUID characteristics (a) at  $T = 3.70 \text{ K}$ , where  $\beta_L$  is slightly above 1 (b) at  $T = 3.58 \text{ K}$ , where  $\beta_L$  is much smaller than 1.

period if the CPR is dominated by the  $\sin(2\phi)$  component.

Fits of the rf SQUID characteristics to the form of the Equation (5.1) reveal sinusoidal CPR with no appreciable distortions for  $\beta_L < 1$ . Figure 5.4 shows the fits of the rf SQUID response to the bias current assuming a sinusoidal CPR. As expected, for  $\beta_L > 1$  the sinusoidal fit does not work for the entire curve (Figure 5.4(a)), for  $\beta_L \ll 1$  the sinusoidal fit gives very good agreement. From the fit, the values of the apparent critical current, the inductance of the loop, and the offset phase of the modulation can be extracted. The offset phase can be non-zero due to the magnetic flux induced by the residual magnetic field present in the cryostat, it can also vary due to the offset in the dc SQUID detector, which provides only a relative reading of the magnetic flux.

## 5.2 Current-phase relation data and analysis

In the trombone sample described previously, the temperature range in which  $|\beta_L| < 1$  is 3.50 K - 3.70 K if the trombone loop is fully covered by the superconducting ground plane. In this interval of temperatures, the CPR can be extracted from the rf SQUID characteristics. Figure 5.5 shows a set of the rf SQUID characteristics for the trombone sample in the entire non-hysteretic regime taken with 10 mK steps in temperature. Temperature in the experiment was monitored by reading the helium vapor pressure with an absolute pressure gauge.

This set of data has a number of interesting features. First of all, the amplitudes of the modulations due to the Josephson junction decrease with decreasing temperature. At  $T = 3.59$  K no discernible modulation is observed, indicating that the critical current of the Josephson junction is zero at this temperature. At temperatures below  $T = 3.59$  K the modulation appears again, but the phase of the modulation at tem-

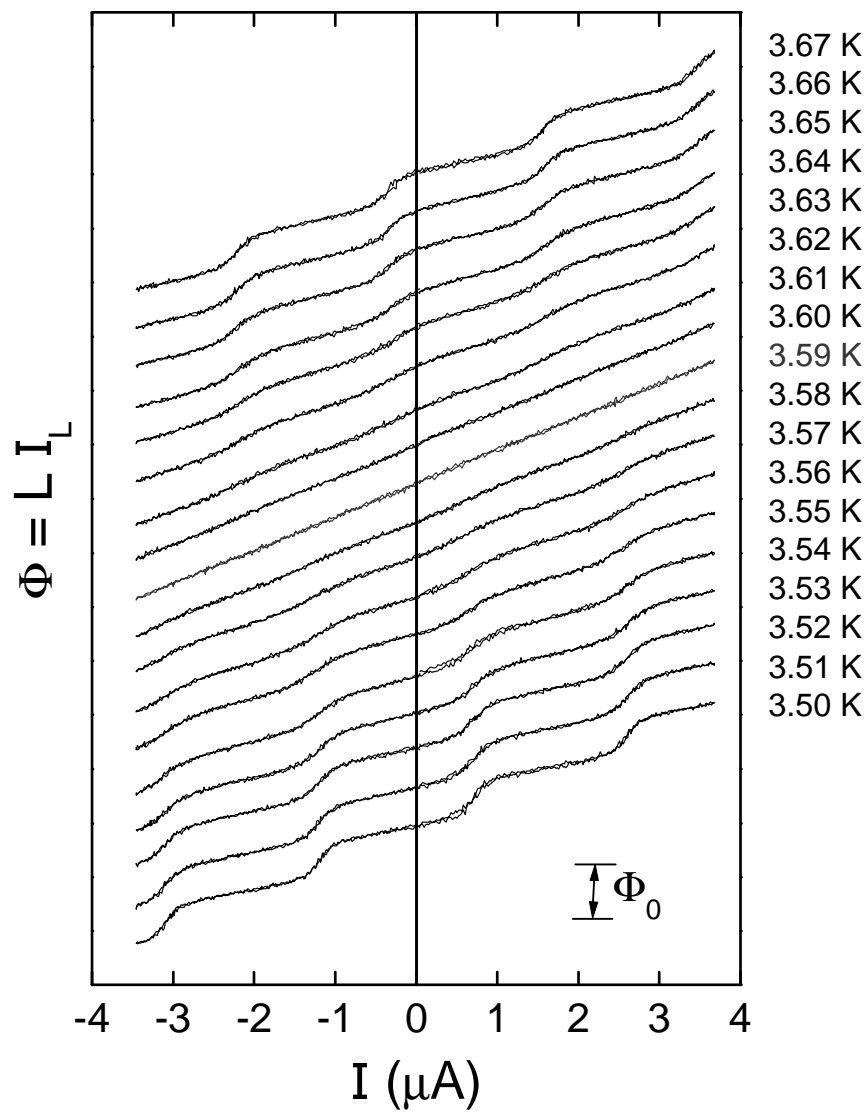


**Figure 5.5:** rf SQUID characteristics of the trombone sample in the temperature range 3.50 - 3.68 K. Curves are offset for clarity.

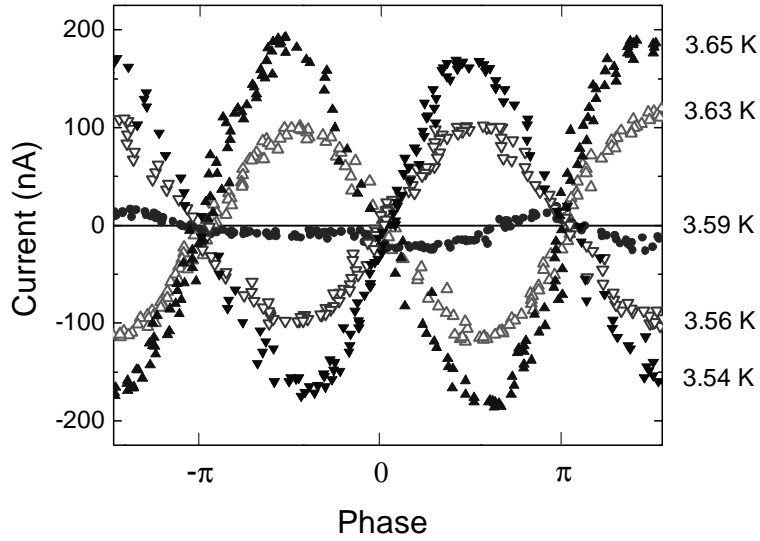


**Figure 5.6:** Current-phase relations extracted from the rf SQUID characteristics of a trombone sample in the  $|\beta_L| < 1$  temperature range.

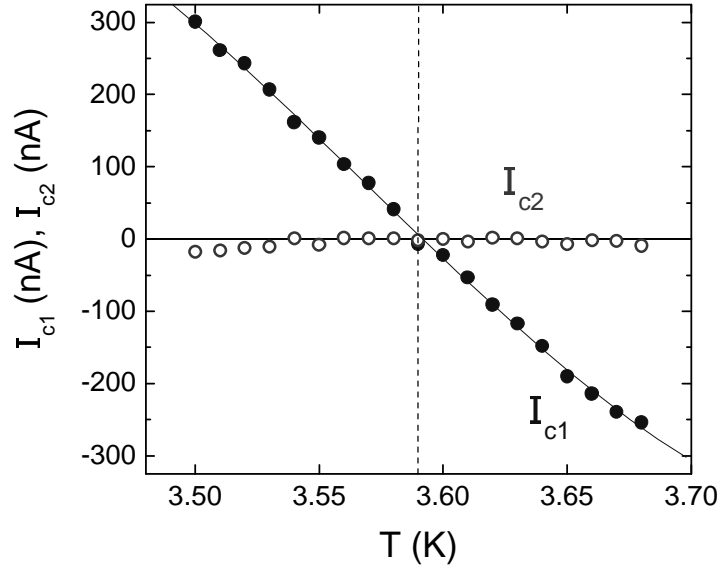
peratures  $T < 3.59$  K is shifted by exactly  $\pi$  from the phase above  $T = 3.59$  K. This behavior indicates that the critical current of the junction changes sign at  $T = 3.59$  K.

Figure 5.6 shows the current-phase relations extracted from the data in Figure 5.5 by subtracting the linear slope due to the inductance of the loop. The current-phase relations above and below  $T = 3.59$  K are out of phase. The extracted CPR at  $T = 3.59$  K has no discernible periodicity, only fluctuations on the order of 10 nA in the current can be seen. These fluctuations limit our critical current resolution. The current-phase relation appears sinusoidal, without noticeable higher-order terms.

The values of the apparent critical current can be obtained from the rf SQUID characteristic fits similar to the ones shown in Figure 5.4. Figure 5.7 demonstrates the amplitudes of the first and the second harmonics in the CPR obtained by fitting the data in Figure 5.5 using the Equation (5.1) and assuming a CPR of the form:

$$CPR(\phi) = I_{c1} \sin(\phi) + I_{c2} \sin(2\phi). \quad (5.3)$$

The amplitude  $I_{c1}$  of the sinusoidal component of the current-phase relation changes



**Figure 5.7:** Amplitudes of the first and second harmonics of the supercurrent obtained by fitting the set of data in Figure 5.5.

sign at  $T_\pi = 3.59$  K. No measurable  $\sin(2\phi)$  component is observed. The amplitude  $I_{c2}$  obtained from our fits is smaller than the resolution of the measurement. This means that the component  $I_{c1}$  corresponds to the critical current of the junction  $I_c$ . Close to  $\beta_L = 1, -1$ , a small amount of  $\sin(2\phi)$  can be picked up in the fit. However, in this regime the trombone rf SQUID is nearly hysteretic, therefore the shape of the apparent CPR is deformed. The critical current of the junction goes to zero completely at  $T_\pi$ , and the change in the sign of the critical current is abrupt.

Theory predicts that the secondary Josephson tunneling, which gives rise to the  $\sin(2\phi)$  component in the current-phase relation, should become observable when the first order  $\sin(\phi)$  tunneling vanishes. Early calculations predicted  $\sin(2\phi)$  to dominate the CPR in the SFS CuNi junctions with  $d = 22$  nm [49]. These estimates were later corrected, when the experimental values for  $\xi_{F1}$  and  $\xi_{F2}$  became available. It was realized, that junctions with  $d = 22$  nm are in the highly diffusive limit, in which  $\sin(2\phi)$  term is averaged out. Historically, no data was initially available from SFS

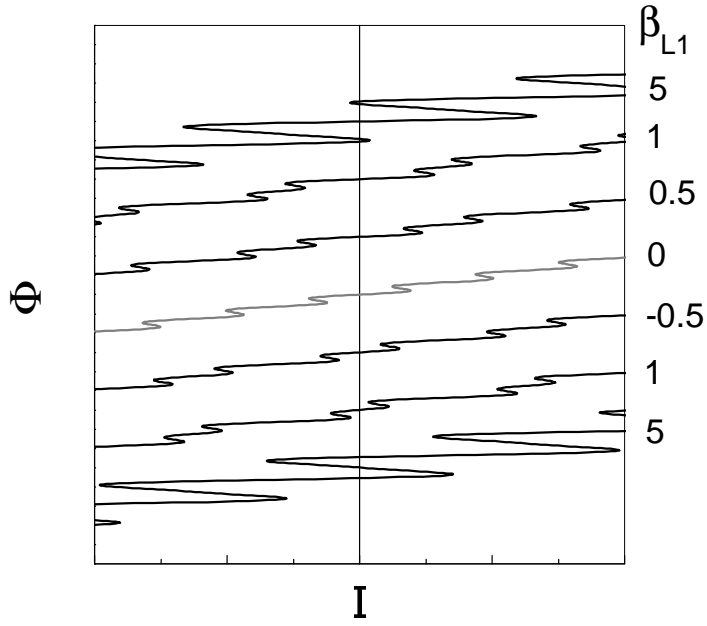


**Figure 5.8:** Simulated rf SQUID characteristics for an rf SQUID with a junction that has a CPR (5.3) in the range  $-5 < \beta_{L1} < 5$ , and with  $\beta_{L2} = 1$ .

junctions with thickness around 10 nm. Experimental and theoretical work was done under the assumption that  $d = 22$  nm is the thickness of the first node of  $I_c(d)$ . New predictions suggest that the  $\sin(2\phi)$  term should become observable near the first node of  $I_c(d)$  around  $d = 11$  nm [53; 54] with the predicted supercurrent density of the second component at  $\approx 10$  A/cm<sup>2</sup>. Experimental studies of the CPR in junctions near the first node of  $I_c(d)$  are currently under way.

Figure 5.8 shows the rf SQUID characteristics simulated for an rf SQUID with a junction described by the CPR (5.3). In this simulation the inductance parameter  $\beta_{L1} = 2\pi I_{c1}L/\Phi_0$  was varied from -5 to 5, and  $\beta_{L2} = 2\pi I_{c2}L/\Phi_0$  was kept at 1. The period of the rf SQUID modulation is two times smaller around  $\beta_{L1} = 1$ . Other interesting effects, like the double hysteretic loops in the rf SQUID modulation, could be observed in the regime  $\beta_{L1}, \beta_{L2} \approx 1$ .

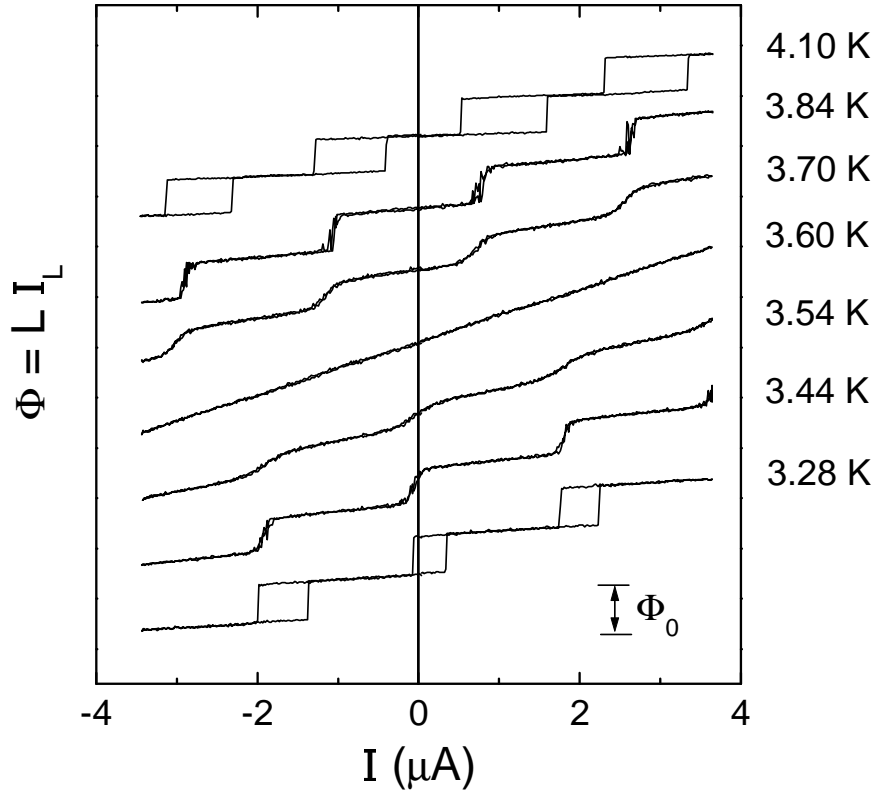


**Figure 5.9:** A set of the rf SQUID characteristics for the trombone sample measured in a different residual field.

### 5.3 Effects of residual magnetic field

Even though the current-phase relation data unambiguously demonstrates the sign change of the critical current at  $T_\pi$ , it turned out to be difficult to determine the absolute sign of the critical current in the trombone geometry due to the external magnetic flux from the residual magnetic field in the dewar. Even though the dewar is enclosed in a  $\mu$ -metal shield with high magnetic permeability, magnetic field on the order of 1-10 mG may still be present near the sample. This results in magnetic flux of 50-500  $\Phi_0$  threading the loop. Magnetic flux of such magnitude may produce an arbitrary offset phase ranging anywhere from 0 to  $2\pi$  in the superconducting loop. The precise determination of the sign of the critical current is, however, dependent on

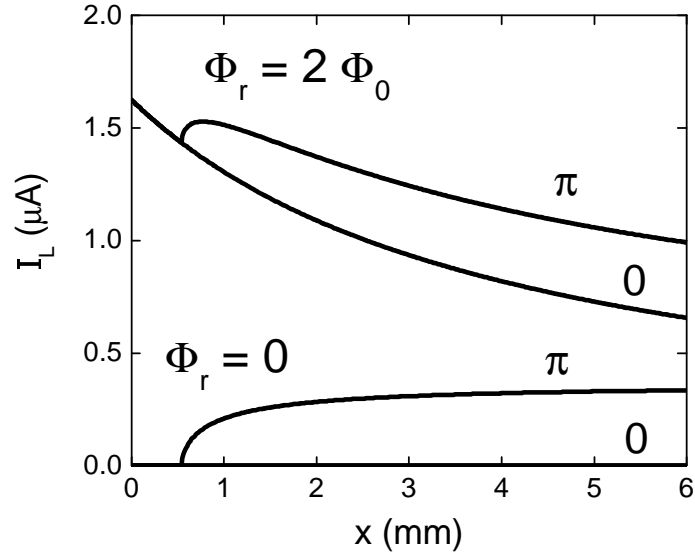
the knowledge of the phase of the rf SQUID modulation. If the rf SQUID modulation is near the phase of  $\pi$  for zero bias current, the sign of the critical current is negative. The sign is positive when the phase of the modulation is near 0. Because at the second node of  $I_c(d)$  the  $\pi$  junction should be above  $T_\pi$  in temperature, the critical current of the junction is plotted as negative in Figure 5.7 at higher temperatures.

Figure 5.9 shows a set of the rf SQUID characteristics of the same sample as in Figure 5.5 on a different cooldown and in slightly different residual magnetic field. Direct interpretation of this data would lead to a conclusion that the  $\pi$  state is the state below  $T_\pi = 3.59$  K in temperature, in contrast to the above arguments. Such conclusion was in fact reached in earlier work [86], in which a phase-sensitive test was done using a two-cell array with a total of 6 SFS junctions near the second 0- $\pi$  transition.

This problem is hard to overcome in any measurement of the current-phase relation and especially using junctions with barriers near a second 0- $\pi$  transition. Given the background field of 1 mG, the dimensions of the rf SQUID loop may only be slightly greater than  $10 \mu\text{m} \times 10 \mu\text{m}$  for the offset flux to be less than  $0.1 \Phi_0$ . But the sizes of the junctions alone should be of order  $50 \mu\text{m} \times 50 \mu\text{m}$  to bring the critical currents up to 1-10  $\mu\text{A}$  range, since the critical current density is low near the second node of the  $I_c(d)$  dependence. In addition, larger loops are required to provide efficient coupling to the measurement dc SQUID.

Besides, the residual magnetic flux hindered the observation of spontaneous magnetic flux in the trombone loop when the geometric inductance was changed by moving the superconducting ground plane. With a change of the trombone loop inductance the current screening the residual magnetic flux was changing. The signal from the screening current was larger than the expected spontaneous current signal.

The exterior contour of the device that includes the trombone loop and the flux



**Figure 5.10:** Simulated average current in the flux transformer loop as a function of the position of the ground plane in a trombone device with a 0 or a  $\pi$  junction with  $I_c = 1 \mu\text{A}$  for zero and finite residual magnetic flux  $\Phi_r$ .

transformer loop forms a large superconducting loop without weak links. The total magnetic flux through such a superconducting loop cannot change. Therefore, a redistribution of background magnetic flux was taking place between the trombone loop and the flux transformer loop depending on the position of the superconducting ground plane, since the ratio of their inductances was changing. This effect was modeled by numerical simulations presented in Figure 5.10. If the residual magnetic flux  $\Phi_r$  is zero, spontaneous currents turn on in a  $\pi$  junction-based trombone at the position of the shield where  $\beta_L = 1$ . In finite  $\Phi_r$ , screening currents add to the spontaneous currents. For  $\Phi_r = 2\Phi_0$  the signature of a spontaneous current can be recovered from the overall response. For example, the data could be taken in the 0 state of the SFS junction, where spontaneous currents are not present and only signal due to screening currents is observed. The experiment could then be repeated in the  $\pi$  junction state, and the screening current background could be subtracted to reveal the spontaneous currents contribution. At higher  $\Phi_r$ , on the order of over

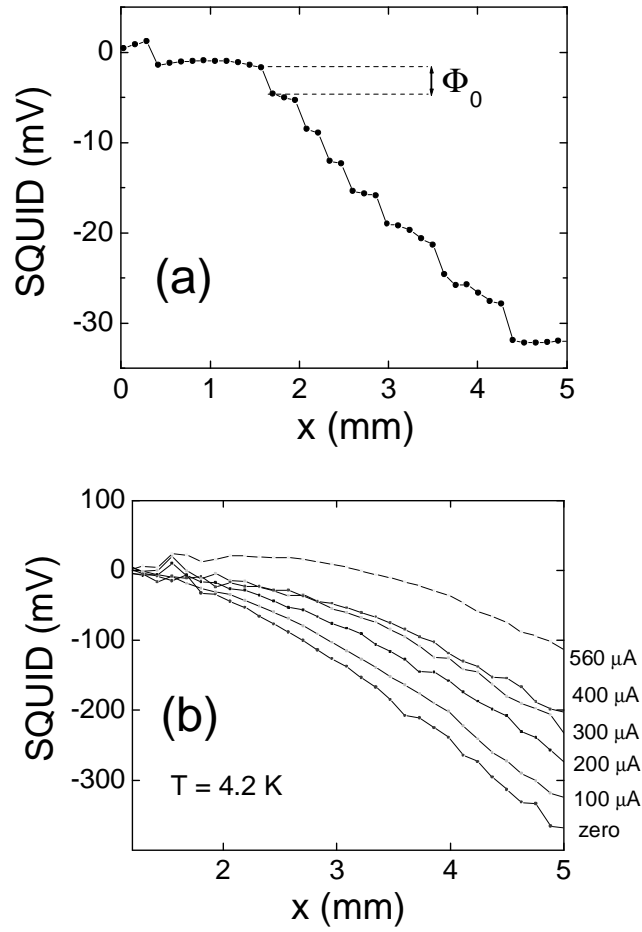


**Figure 5.11:** (a) Trombone experiment data showing transitions between rf SQUID fluxoid states induced by the motion of the superconducting ground plane (b) Applied field dependence of the trombone experiment data for various currents through the field coil.

$10\Phi_0$ , however, the relative magnitude of the spontaneous currents signal becomes much smaller than the screening current background, and the subtraction becomes less accurate.

The actual variable inductance data has several features that are not modeled in the simulation in Figure 5.10. Figure 5.11(a) shows that, in fact, the screening current does not change smoothly as the trombone inductance is changed, instead it changes in discrete jumps. This is explained by the fact that an rf SQUID is in the hysteretic regime and can transition between adjacent fluxoid states. This can also be viewed

as hopping of flux quanta from the trombone loop into the flux transformer loop through the Josephson junction, as the inductance of the trombone loop is increased. Naturally, jumps in the data obscure the observation of spontaneous currents even more.

We have also attempted to apply external magnetic field to the device in order to compensate the residual magnetic field of the cryostat. Figure 5.11(b) shows that it is possible to reduce the signal from the screening currents by “counter-screening” the background magnetic field with the applied magnetic field. However, at fields corresponding to the cancelation of screening and counter-screening currents, such as the field created by a current of  $560 \mu\text{A}$  in the field coil in Figure 5.11(b), the signal becomes non-monotonic, which additionally complicates the observation of spontaneous currents. This behavior is due to a change in the magnetic environment of the sample caused by the motion of the superconducting ground plane. Vortices trapped in the ground plane or spontaneous currents circulating around its edges, can create local fields that couple into the device. The residual background field of the cryostat can also be non-uniform. In the best data that we took, the non-monotonic response was still on the order of 2-5  $\Phi_0$ .

It is clear that a different approach is required in order to achieve the capability of an absolute, rather than relative, measurement of the sign of the critical current, as well as to observe spontaneous currents in superconducting loops with  $\pi$  junctions. In order to achieve both of these goals, we prepared superconducting arrays of  $\pi$  junctions with non-uniform frustration and imaged the spontaneous current distributions in these arrays with a scanning SQUID microscope. The results of these measurements are presented in Chapter 8.

# Chapter 6

## Experiments on Non-Uniform SFS

### 0- $\pi$ Junctions

#### 6.1 Diffraction patterns of 0- $\pi$ junctions

In the vicinity of a 0- $\pi$  transition, one has a unique opportunity to study Josephson junctions with spatial changes in the sign of the critical current density, the so-called 0- $\pi$  junctions. Consider an SFS junction with variations in the barrier thickness. Regions of different thickness will have different 0- $\pi$  transition temperatures. For example, in a junction near the first node of  $I_c(d)$  with a step in the barrier thickness, the thinner part will have a transition temperature  $T_{\pi_1}$ , while the thicker part will have a transition temperature  $T_{\pi_2} > T_{\pi_1}$ . At temperatures below  $T_{\pi_1}$  the entire junction is a  $\pi$  junction, and at temperatures above  $T_{\pi_2}$  the entire junction is a 0 junction. In the temperature range  $T_{\pi_1} < T < T_{\pi_2}$  the thicker part of the junction is in the  $\pi$  state, but the thinner part is still in the 0 state.

The most straightforward way to identify a 0- $\pi$  junction is to measure its critical current vs. applied magnetic flux diffraction patterns. In a uniform Josephson junc-

tion, the diffraction patterns have a characteristic Fraunhofer shape proportional to  $\sin(\pi\Phi_{ex}/\Phi_0)/(\pi\Phi_{ex}/\Phi_0)$  [61]. The critical current is maximal in zero applied magnetic flux. If magnetic flux is present in the junction, the Josephson phase difference changes along the junction width in order to maintain fluxoid quantization. Supercurrents in different cross-sections of the junction interfere, which leads to a suppression of the net critical current. The diffraction patterns of uniform junctions have nodes at integer values of the applied magnetic flux. In  $0-\pi$  junctions, sign changes in the critical current density cause destructive interference of supercurrents even in zero applied magnetic flux. As a result, the diffraction patterns do not necessarily have a maximum at zero field and instead may have a node or a local minimum.

Diffraction patterns can be obtained by extracting critical currents from the IV characteristics measured at a series of applied magnetic flux values. Another way to measure diffraction patterns is to use a Proportional-Integral-Derivative (PID) controller. A PID controller can adjust the junction bias current to maintain a junction voltage or a junction differential resistance threshold. If a voltage threshold is small, the bias current is very close to the critical current. In our experiments, we used a PID software developed for the National Instruments Labview environment.

Figure 6.1 shows two examples of the diffraction patterns measured in uniform SFS junctions. In panel (a), the diffraction pattern of a trilayer junction measured at  $T = 4.2$  K is shown. The barrier thickness of this junction is far from any  $0 - \pi$  transitions, meaning that small non-uniformities in the barrier do not cause sign changes in the critical current density along the junction width. The agreement with the Fraunhofer shape is rather good. Panel (b) shows a diffraction pattern measured at  $T = 5$  K in a junction fabricated in the layer-by-layer process near the second  $0 - \pi$  transition. This data is also in good agreement with the Fraunhofer dependence suggesting uniform critical current density. No deviations from the Fraunhofer shape were found in the

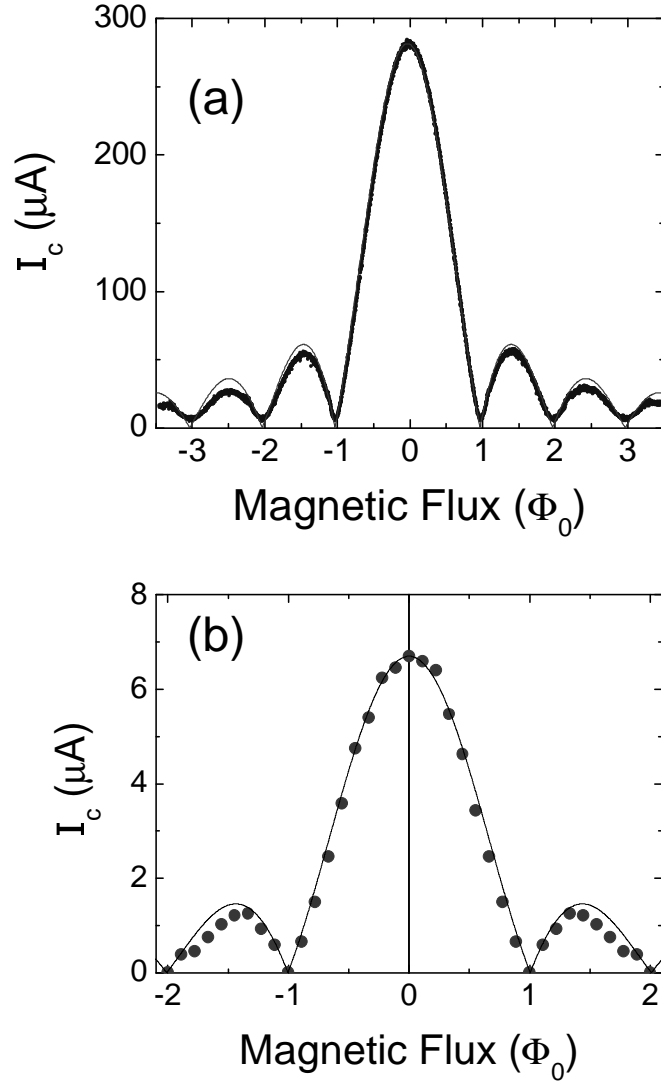


**Figure 6.1:** Diffraction patterns of uniform SFS junctions for (a) a trilayer junction far from the nodes of  $I_c(d)$  and (b) a layer-by-layer junction near the second  $0-\pi$  transition. Both panels show best fits to the Fraunhofer dependence.

diffraction patterns of SFS junctions near the second  $0 - \pi$  transition with  $d \approx 22$  nm even at temperatures very close to  $T_\pi$ .

The situation changes in junctions with  $d \approx 11$  nm close to the first node of the  $I_c(d)$  dependence. Figure 6.2(a) shows a set of diffraction patterns measured at a series of temperatures for sample A, which is an SFS junction with  $d \approx 11$  nm. At  $T = 4.2$  K, the diffraction pattern resembles the Fraunhofer dependence, but there are differences. Namely, the critical current does not vanish to zero in the nodes of  $I_c(\Phi_{ex})$ . In the short junction limit, in which magnetic fields generated by supercurrents flowing through the junctions can be neglected, this behavior is an indication of a non-uniform critical current density [87]. For example, there could be a narrow region of high critical current density in the junction. The non-vanishing critical current does not mean that there are sign changes in the critical current density.

As the temperature is lowered, a peak in the center of the diffraction pattern at zero applied magnetic flux changes into a dip. This means that regions of opposite polarity critical current exist within the junction. At  $T \approx 1.4$  K the dip in the center almost reaches zero, which indicates that around that temperature the net critical currents of  $0$  and  $\pi$  regions in the junction nearly compensate each other. If one were to measure the critical current as a function of temperature in sample A in zero applied field, one would find a dependence similar to the one shown in Figure 4.7. The critical current would reach a minimum at a temperature close to 1.5 K. This temperature cannot, however, be called  $T_\pi$ , because it does not correspond to a local transition between  $0$  and  $\pi$  states. As we noted earlier, in a  $0-\pi$  junction each segment has its own  $T_\pi$ . The temperature at which the critical currents of  $0$  and  $\pi$  regions cancel each other in the short junction limit we call  $T_{\pi 0}$ . At  $T_{\pi 0}$ , the critical current can be made non-zero if magnetic flux is applied to the  $0-\pi$  junction or if the junction

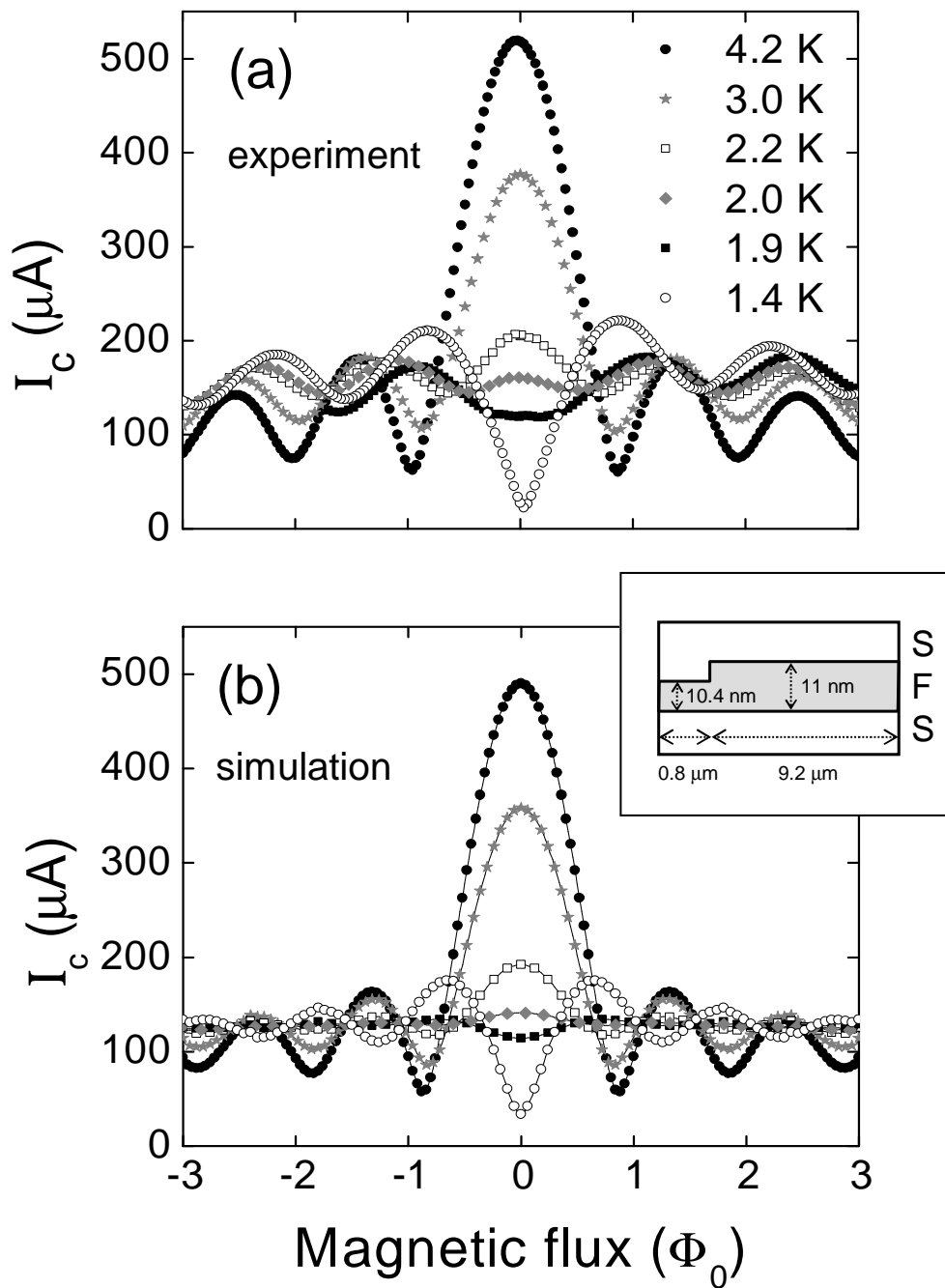


**Figure 6.2:** SAMPLE A. (a) Measured diffraction patterns at a series of temperatures (b) Simulated diffraction patterns for the barrier shape shown in the inset.

is in the long junction limit. In contrast, in uniform SFS junctions the critical current is zero at the true  $0-\pi$  transition temperature  $T_\pi$  in any applied magnetic flux.

The origin of the  $0-\pi$  junction behavior is critical current density non-uniformities. At the moment we do not know the exact physical nature of these non-uniformities. They could be due to variations in the ferromagnetic barrier thickness. It is also possible that the exchange energy is non-uniform within the junction due to variations in the composition of the CuNi films. Changes in the exchange energy lead to changes in the order parameter oscillation length  $\xi_{F2}$ . Finally, the transparencies of the S-F interfaces may vary along the junctions. According to some theories, the transparencies of the SF interfaces in SFS junctions influences the onset of the  $\pi$  state, because the order parameter experiences a phase drop at each interface [88]. These phase drops adds offsets to the winding of phase that occurs due to the exchange field.

We do know that the amount of junction processing after the deposition of the CuNi ferromagnetic layer affects the size and the frequency of occurrence of these non-uniformities. If the sample is not ion-milled too long at the cleaning stage before the deposition of the top wiring electrode, and if the sample is not annealed, the non-uniformities are rather small and observable only in a temperature range of  $\approx 0.1$  K close to  $T_{\pi 0}$ . Otherwise the effects of non-uniformities can be seen in the diffraction patterns over several degrees K, as is the case for the sample A.

In order to quantify the non-uniformities in our samples we used a model that assumes the non-uniformities are due to variations in the barrier thickness. For a given barrier profile  $d(y)$ , where  $y$  is the dimension along the junction width, we can calculate the critical current density  $J(y)$  using the Equation (3.10). We introduce the temperature dependence of  $J(y)$  by assuming that  $\xi_{F1}$  and  $\xi_{F2}$  depend on temperature

in the following way:

$$\frac{\xi_{F1,F2}(T)}{\xi_{F1,F2}(0)} = \left\{ \frac{E_{ex}}{[(\pi k_B T)^2 + E_{ex}^2]^{1/2} \pm \pi k_B T} \right\}^{1/2}, \quad (6.1)$$

where  $\xi_{F1,F2}(0)$  are the values at zero temperature obtained from the fit of the experimental data in Figure 4.6(a). Equation (6.1) is a modification of the Equation (3.8) which makes it convenient to incorporate the experimental values for  $\xi_{F1}$  and  $\xi_{F2}$  into the model.

For a known critical current density, we can simulate the diffraction patterns. In a junction with a sinusoidal CPR, the diffraction pattern turns out to be the absolute value of the Fourier transform of  $J(y)$  [87]. We can adjust the assumed barrier profile that yields  $J(y, T)$  in order to match the set of experimental diffraction patterns to the simulated ones. Simulations were done using Mathcad 2000 software.

Results of the simulations for sample A are shown in Figure 6.2(b). We were able to get good agreement with the experimental data for the barrier profile shown in the inset. The barrier has one 6 Å step 0.8 μm away from the edge. This is the typical size for the non-uniformities we observe, although smaller non-uniformities can be achieved if the sample processing is reduced.

We can now give a simple explanation to why we were not able to detect any non-uniformities in the junctions near the second node of  $I_c(d)$ . Because the critical current density is much smaller at the second node, junctions with larger areas  $\sim 50 \times 50 \mu\text{m}^2$  were used in order to achieve measurable critical currents, as opposed to  $4 \times 4 - 10 \times 10 \mu\text{m}^2$  junctions that can be used at the first node. The non-uniformity of the same size as in sample A would have a very small relative contribution to the diffraction patterns of the junctions with 25-100 times larger areas.

Additional examples of the diffraction pattern data from non-uniform samples B and C with  $d$  close to 11 nm are given in Figures 6.3 and 6.4. Junction B is a

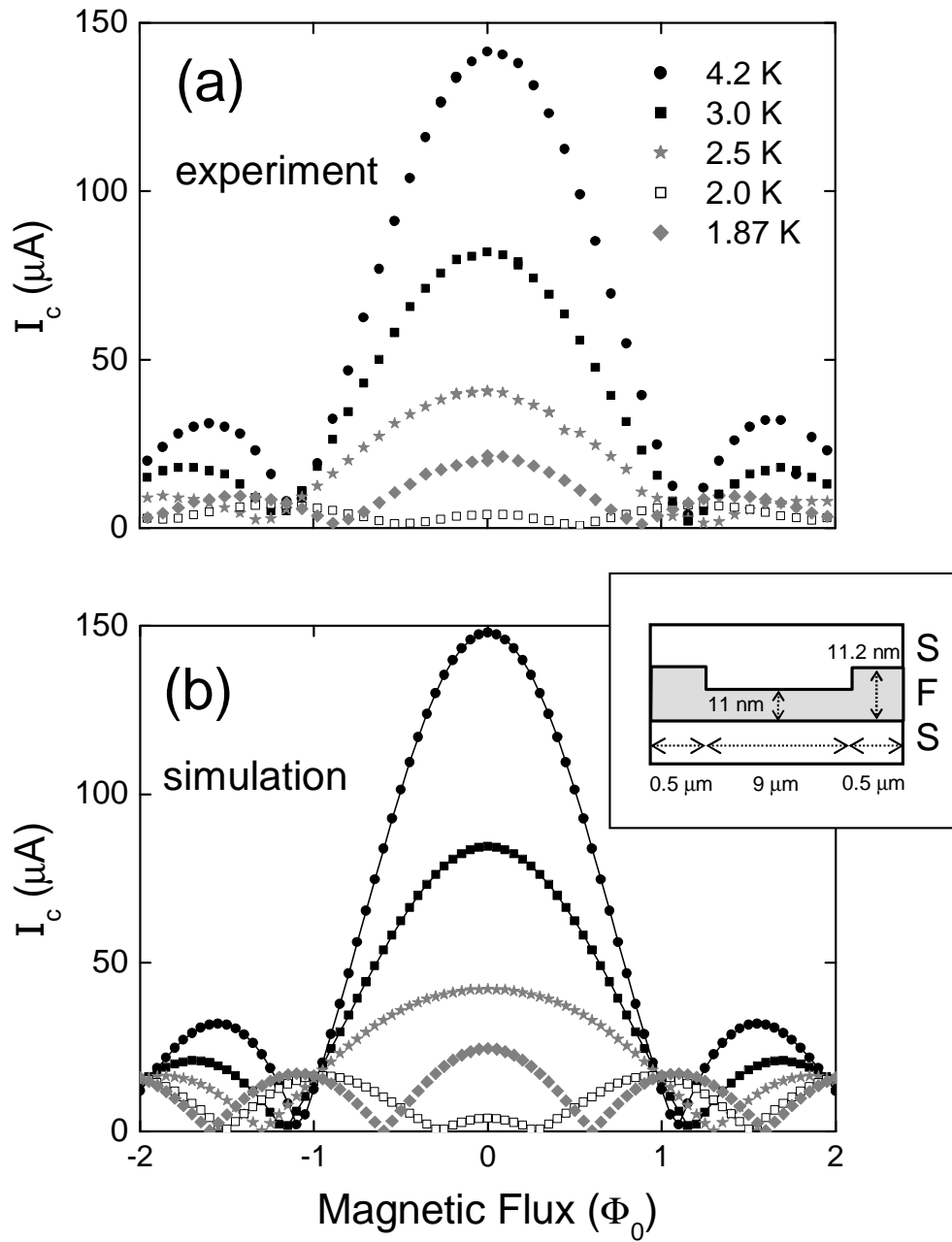


**Figure 6.3:** SAMPLE B. (a) Measured diffraction patterns at a series of temperatures. This data was obtained in the group of Prof. Ryazanov. (b) Simulated diffraction patterns for the barrier shape shown in the inset.

$10 \times 10 \mu\text{m}^2$  SFS junction, the area of junction C is  $4 \times 4 \mu\text{m}^2$ . For these samples, the data is better described if more complicated barrier shapes are assumed. For junction B, we were able to get good qualitative and quantitative fit by assuming a barrier with two symmetric steps (see the inset to Figure 6.3(b)). The step height is  $2 \text{ \AA}$ , smaller than for sample A. The diffraction patterns confirm that sample B is more uniform than sample A. The  $T_{\pi_0}$  of sample B is around 2 K, but the diffraction patterns still look Fraunhofer-like around 3 K. In sample A, with  $T_{\pi_0} \approx 1.5 \text{ K}$ , deviations from the Fraunhofer dependence are noticeable at  $T = 4.2 \text{ K}$ , almost 3 K away from  $T_{\pi_0}$ . If the diffraction patterns of samples B and C were measured in a larger range of the applied magnetic fields, a more complicated structure could emerge corresponding to finer non-uniformities in the barrier. The sweep range of the magnetic flux in these experiments was determined by a maximum field that could be applied using our superconducting solenoid coil.

Sample C is rather interesting, because the third peak in its diffraction patterns is higher than the second (Figure 6.4(a)). By analogy to the diffraction of light, we looked for a barrier shape with three periodically repeated features. We obtained reasonably good agreement with the data by assuming the barrier shape shown in the inset to Figure 6.4(b). The step sizes are  $2 \text{ \AA}$ , same as for junction B. But because the area of junction C is smaller, the effects of non-uniformities are noticeable in the diffraction patterns in the wider temperature range than in junction B. There are, however, features in the data that this fit failed to reproduce. In particular, almost none of the data have nodes around  $1 \Phi_0$  of the applied magnetic flux, while the simulated diffraction patterns do. The reason for this is that we assumed a symmetric barrier for the simulation. In the actual sample, the sizes of different steps were likely not the same. Asymmetry of the barrier causes the critical current not to vanish in the nodes, as in junction A. We have used a symmetric fit because it makes further

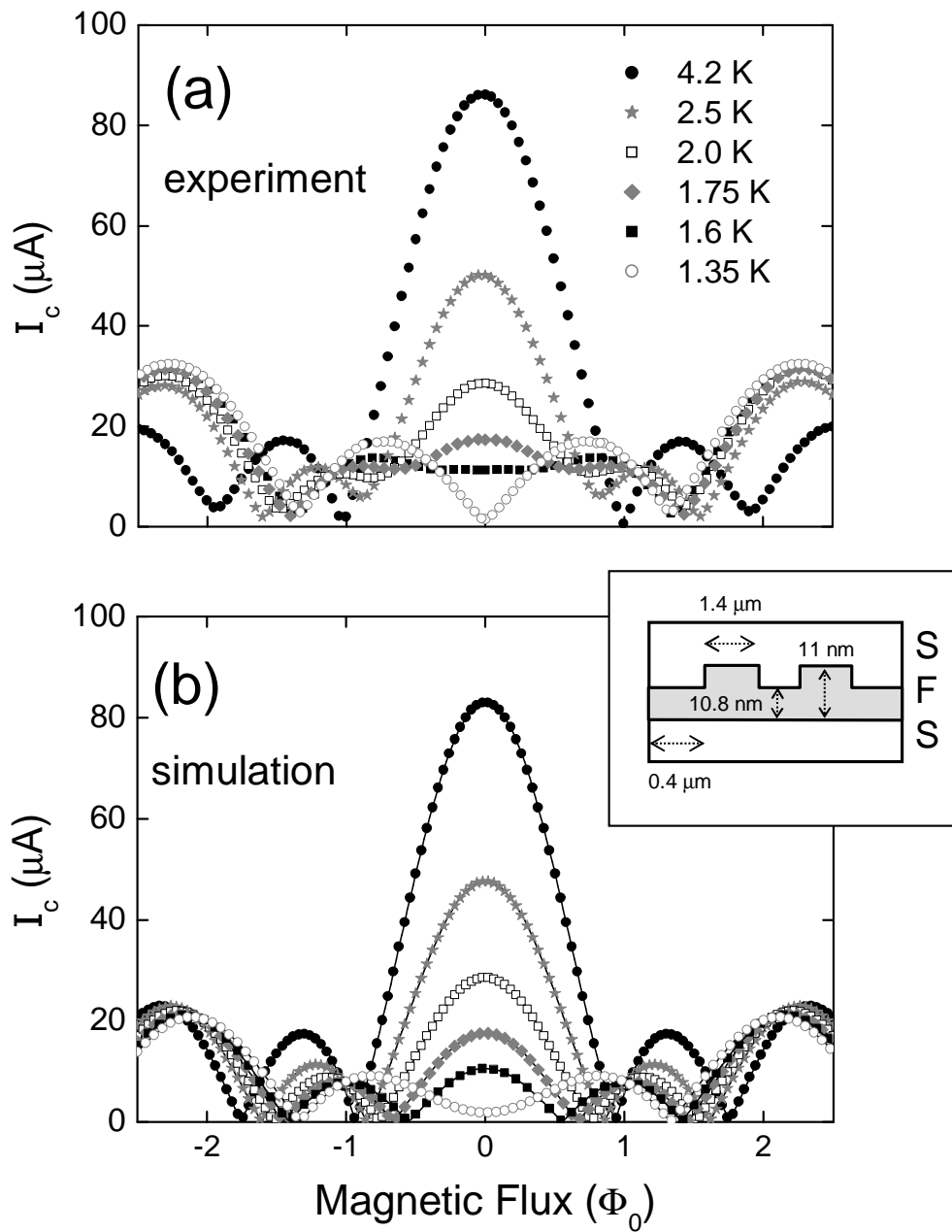


**Figure 6.4:** SAMPLE C. (a) Measured diffraction patterns at a series of temperatures (b) Simulated diffraction patterns for the barrier shape shown in the inset.

analysis of the data more straightforward.

However, the fit for sample C, as well as the fits for samples A and B demonstrate good quantitative agreement with the experiment in terms of the magnitude of the critical current in the entire temperature range of data, which means that heights and widths of the barrier steps are determined with high accuracy.

Within our model, we can understand the behavior of the individual sections of the junction. For known barrier shapes of junctions A, B and C, we can use the Equations (3.10) and (6.1) to calculate the zero field temperature dependences of the critical currents of the thin and thick parts of the junctions  $I_{c1}$  and  $I_{c2}$ , and the net critical current  $I_c = I_{c1} + I_{c2}$ .

The results are shown in Figure 6.5. In this simulation, we multiplied the critical current density of the thick segments by the total area of all thick segments to get  $I_{c2}$ , and  $I_{c1}$  was obtained in the same way for the thin segments. In sample A, the thinner part remains in the 0 state at all temperatures, while the thicker part transitions into  $\pi$  state at  $T \approx 2$  K, which is 0.5 K above  $T_{\pi 0}$  for this sample. In samples B and C both thin and thick parts of the junctions transition into  $\pi$  state, but at temperatures  $\sim 2$  K apart. This illustrates that a 1 Å change in the barrier thickness changes  $T_\pi$  by 1 K.

It should be noted, that the diffraction patterns similar to those in Figures 6.2, 6.3 and 6.4 were measured [89] and simulated [26; 90; 91] for the d-wave corner junctions, in which one superconducting electrode is a corner of a d-wave crystal, and the other superconductor has a conventional s-wave symmetry. Such junctions are often referred to as “0- $\pi$  junctions” in literature. However, neither of the faces of the d-wave corner is in the  $\pi$  junction state characterized by a negative critical current. The difference between the 0- $\pi$  junctions as defined in the beginning of this Chapter and the d-wave corner junctions can be understood if the phase difference

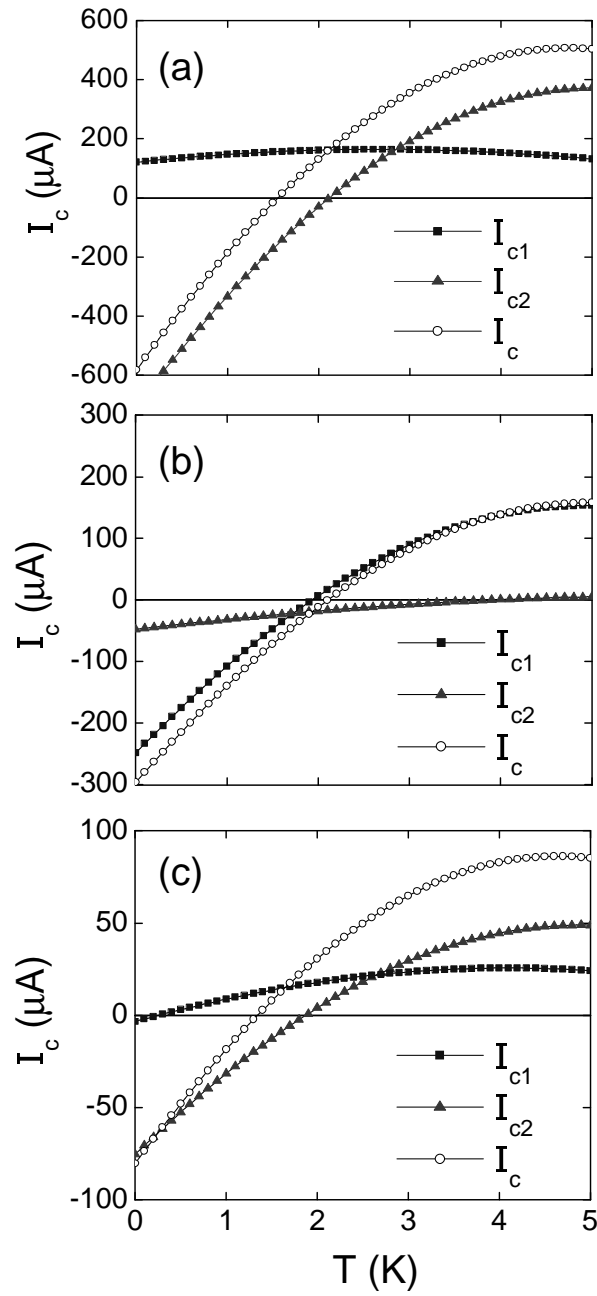


**Figure 6.5:** Simulated zero field temperature dependences of the critical currents of the thin ( $I_{c1}$ ) and thick ( $I_{c2}$ ) regions of the junctions and of the net critical current  $I_c$  (a) for sample A (b) for sample B (c) for sample C.

distributions in both types of junctions are compared. In the absence of spontaneous currents, the phase difference in the true  $0-\pi$  junction is uniform, i.e. it is either 0 or  $\pi$  in the entire junction. In the d-wave corner junction the superconducting phase difference is shifted by  $\pi$  on the opposite faces of the d-wave corner in the absence of spontaneous currents. Spontaneous currents create non-uniform phase difference distributions both in  $0-\pi$  junctions and in d-wave corner junctions.

## 6.2 Spontaneous currents in $0-\pi$ junctions

In  $0-\pi$  Josephson junctions, just like in  $0-\pi$  SQUIDS, part of the system prefers to be in the state with the phase difference of 0, while the other part prefers to be in the state with the phase difference of  $\pi$ . A  $0-\pi$  junction can either be in the uniform state with either  $\phi = 0$  or  $\phi = \pi$ , or in a state with spontaneous currents and, hence, a non-uniform phase difference. Transitions between uniform and non-uniform regimes are governed by energy considerations. The total energy of a  $0-\pi$  junction has two terms: the Josephson energy and the magnetic field energy associated with circulating currents. For a  $0-\pi$  with only one  $0-\pi$  boundary and a step-like distribution of the critical current density, as shown in Figure 6.6, the total energy is equal to [92; 93]:

$$F = \frac{\Phi_0 J_{c0}}{2\pi} \int_{-w_0}^0 \left[ \frac{\lambda_{J0}^2}{2} \left( \frac{d\phi}{dy} \right)^2 + 1 - \cos \phi \right] dy + \frac{\Phi_0 |J_{c\pi}|}{2\pi} \int_0^{w_\pi} \left[ \frac{\lambda_{J\pi}^2}{2} \left( \frac{d\phi}{dy} \right)^2 + 1 + \cos \phi \right] dy. \quad (6.2)$$

where  $J_{c0}$  and  $J_{c\pi}$  are the critical current densities in the 0 and  $\pi$  regions of the junction (see Figure 6.6(b)). The term proportional to the square of the spatial derivative of the phase difference is the magnetic field energy. The coefficients  $\lambda_{J0}$  and  $\lambda_{J\pi}$  are the Josephson penetration depths of 0 and  $\pi$  regions. The Josephson

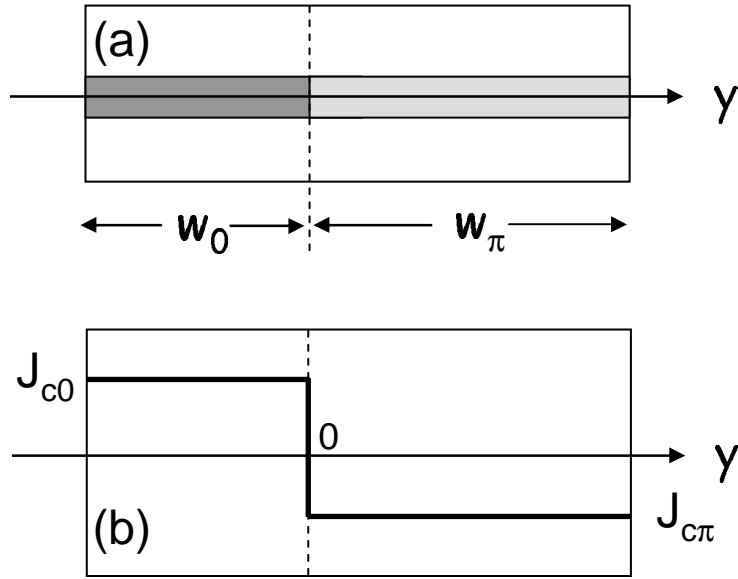


**Figure 6.6:** (a) A 0- $\pi$  Josephson junction with one 0- $\pi$  boundary (b) Critical current density of a 0- $\pi$  junction shown in panel (a) changes sign at  $y=0$ .

penetration depth is given by:

$$\lambda_J = \sqrt{\frac{\hbar}{2\epsilon\mu_0|J_c|d_m}}. \quad (6.3)$$

where  $d_m = 2\lambda + d$  is the thickness up to which magnetic fields penetrate the Josephson junction through the barrier. From the period of the diffraction patterns, we estimated the London penetration depth  $\lambda$  to be 95 nm for the thin niobium films that we use. The magnetic thickness  $d_m$  of our junctions is approximately 220 nm.

The magnitude of  $\lambda_J$  determines whether the magnetic field energy is of importance relative to the Josephson coupling energy in a particular junction. Indeed, if  $\lambda_J$  is very large, it is advantageous to zero the gradient in the phase difference in the Equation (6.2). The limit  $\lambda_J \gg w$ , where  $w$  is the width of the junction is called the *short junction limit*. In the short junction limit, the magnetic self-field energy of currents flowing in the junction is very small, and the distribution of phase difference is uniform along the  $y$ -axis. If  $\lambda_J$  is comparable to or greater than the junction width  $w$ , magnetic self-fields of currents flowing through or circulating in the junction cause

non-uniform distributions of the phase difference. In this regime the junction can be called a *long junction*.

In the long junction regime, minimization of energy given by the Equation (6.2) leads to the following equations for the spatial distribution of the phase difference in a 0- $\pi$  junction shown in Figure 6.6 [92; 93]:

$$\begin{aligned} \frac{d^2\phi}{dy^2} - \frac{1}{\lambda_{J0}^2} \sin\phi &= 0, & -w_0 < y < 0 \\ \frac{d^2\phi}{dy^2} + \frac{1}{\lambda_{J\pi}^2} \sin\phi &= 0, & 0 < y < w_\pi \end{aligned} \quad (6.4)$$

These equations can be solved analytically or numerically. Note that uniform solutions  $\phi(y) = 0$  and  $\phi(y) = \pi$  are allowed, but they are not always the lowest energy solutions. Bulaevskii et al. [92] found conditions for the onset of non-uniform solutions to be the following:

$$\begin{aligned} \lambda_{J\pi} \tanh(w_0/\lambda_{J0}) &= \lambda_{J0} \tan(w_\pi/\lambda_{J\pi}) \\ \lambda_{J0} \tanh(w_\pi/\lambda_{J\pi}) &= \lambda_{J\pi} \tan(w_0/\lambda_{J0}) \end{aligned} \quad (6.5)$$

For fixed  $w_0$  and  $w_\pi$ , the set of Equations (6.5) defines the region in  $\lambda_{J0}$ - $\lambda_{J\pi}$  space in which spontaneous currents circulate in a 0- $\pi$  junction. Outside this region, the phase difference in the entire junction is either 0 or  $\pi$  and the spontaneous current density  $J(y) = 0$ .

The spontaneous current phase diagrams derived from the Equations (6.5) for samples A, B and C are presented in Figure 6.7. The upper parts of the diagrams correspond to the uniform solutions with  $\phi = 0$ , in the lower parts  $\phi = \pi$  throughout the junctions. The two uniform phases are separated by an intermediate region in which spontaneous currents lead to a non-uniform phase difference distribution  $\phi(y)$ . The amplitudes of spontaneous currents are maximal along the middle line of the

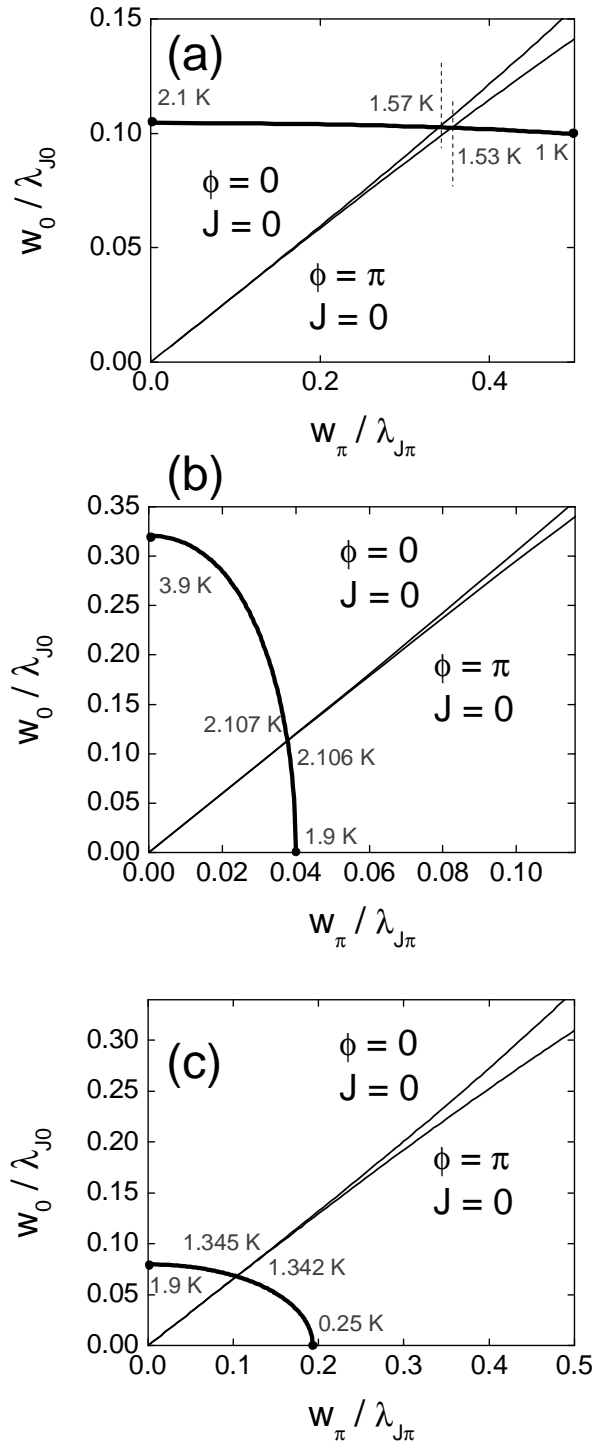


**Figure 6.7:** Diagrams mapping the regions of  $w_0/\lambda_{J0}$  and  $w_\pi/\lambda_{J\pi}$  values for which spontaneous circulating currents flow around the  $0-\pi$  step edges (thin lines) in (a) sample A (b) sample B and (c) sample C. Shown by thick lines are the paths followed by  $0-\pi$  junctions A, B and C in the phase diagram as the temperature is varied.

spontaneous currents region. The diagrams are plotted assuming the barrier shapes deduced from the diffraction patterns. Since there is more than one  $0-\pi$  boundary in samples B and C, true phase diagrams for these junctions are not, strictly speaking, described by the Equations (6.5), which are derived for  $0-\pi$  junctions with a single  $0-\pi$  boundary. Diagrams shown in Figure 6.7 for junctions B and C are therefore approximate. We use the total width of all  $0$  junction segments for  $w_0$  and the total width of all  $\pi$  junction segments for  $w_\pi$  in order to get the upper bound on the width of the spontaneous current region.

Knowledge of the temperature dependence of the critical current density  $J_c(y, T)$  for samples A, B and C allows us to plot the paths these samples follow in the spontaneous current phase diagrams as the temperature is changed. We use the results for the temperature dependences of the critical currents of  $0$  and  $\pi$  segments shown in Figure 6.5 and the barrier shapes from Figures 6.2, 6.3 and 6.4 to calculate the temperature dependences of the Josephson penetration depths  $\lambda_{J0}(T)$  and  $\lambda_{J\pi}(T)$ .

According to our modeling, sample A is a  $0-\pi$  junction in the temperature range  $0 - 2.1$  K. It crosses the spontaneous currents phase when the temperature is between  $1.53$  K and  $1.57$  K (Figure 6.7(a)). Sample B is in the  $0-\pi$  junction state in the temperature interval from  $1.9$  K to  $3.9$  K (Figure 6.7(b)). Because this junction is more uniform, the width of the spontaneous currents region in this junction is only  $1$  mK ( $2.106$  K -  $2.107$  K). Sample C is also more uniform than sample A, and in addition it has smaller area. It is a  $0-\pi$  junction in the range  $0.25$  K -  $1.9$  K (Figure 6.7(c)), and the spontaneous currents interval is also very small - on the order of  $3$  mK ( $1.542$  K -  $1.545$  K). Each sample is in the center of the spontaneous current region at  $T = T_{\pi 0}$ .

Although quite narrow, the temperature range of spontaneous currents in sample A is an order of magnitude larger than in samples B and C. This indicates that one

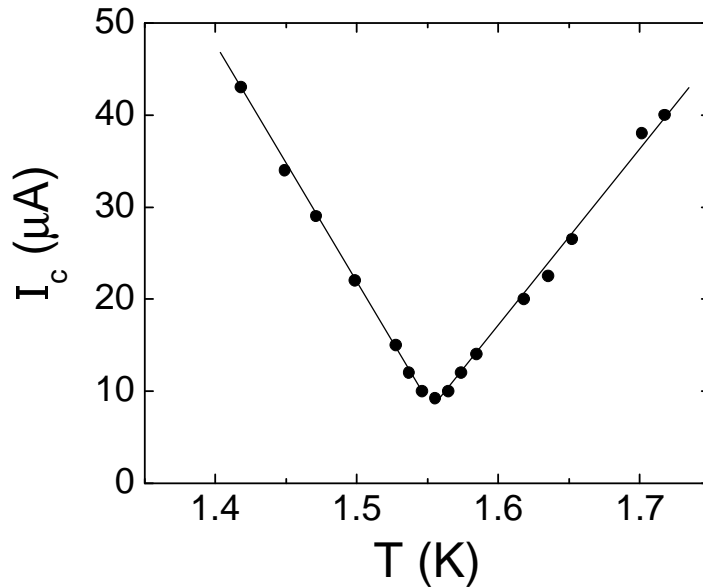


**Figure 6.8:** SAMPLE A. Measured critical current vs. temperature at zero applied magnetic field dips but remains finite.

would have the best chance of observing spontaneous currents in sample A within the temperature range of approximately 50 mK around  $T_{\pi 0}$ .

The most convincing observation of spontaneous currents would be a direct measurement of spontaneous magnetic flux generated in  $0-\pi$  junctions. For example, a scanning SQUID microscope described in the next Chapter can be suitable for this purpose, since it has the proper spatial resolution and the sensitivity to magnetic flux. An interesting technique was recently implemented by Della Rocca et al. [94]. On top of a large SIS junction they fabricated an SFS junction with the superconducting electrodes shorted together. A shorted SFS junction with the SFS part in the  $\pi$  junction state is similar to a  $0-\pi$  Josephson junction. In particular, spontaneous currents may be generated around the short-SFS boundary. The magnetic flux due to spontaneous currents enters the large SIS junction distorting its diffraction pattern, which is measured in the experiment.

In our  $0-\pi$  junctions we have found several effects that can be explained by spon-

taneous currents and can serve as an indirect evidence for their existence. In sample A, we found that the critical current in zero field reaches a minimum at  $T = T_{\pi 0}$  but does not vanish (Figure 6.8). The minimal value of  $I_c$  is  $I_c(T_{\pi 0}) = 10 \mu\text{A}$ . In this experiment, it was important to verify that the background magnetic field is exactly zero. If the temperature dependence of the critical current is measured in finite magnetic field, the critical current does not in general reach zero at  $T = T_{\pi 0}$  (see diffraction patterns in Figure 6.2 for an example). The absence of trapped magnetic flux or background magnetic field was verified by measuring the diffraction patterns which were highly symmetric. Trapped flux can transform the shape of diffraction patterns and, in particular, make the critical current non-vanishing in the nodes. One can usually tell that the trapped flux is present if the diffraction patterns are asymmetric. If a finite background field is present, the diffraction patterns may appear shifted.

In the simulations shown in Figure 6.5 the zero field critical current always reaches zero at  $T_{\pi 0}$ . These simulations were done in the short junction approximation, which assumes a uniform phase difference distribution  $\phi(y) = \text{const}$  in zero applied magnetic field. In the presence of spontaneous currents, the phase difference distribution can be non-uniform if the width of the junction is comparable to the Josephson penetration depth. In this case, supercurrents flowing through different cross-sections of the junction do not exactly compensate each other, and the net critical current is non-zero. In long junctions, the critical currents do not necessarily vanish in the nodes of the diffraction patterns [87]. A simple estimate of the magnitude of the non-vanishing critical currents can be made if our  $0-\pi$  junction A is approximated by a  $0-\pi$  dc SQUID with the loop size of  $10 \mu\text{m} \times 10 \mu\text{m}$  and the critical currents  $I_{c0} = |I_{c\pi}| = 100 \mu\text{A}$ , which are roughly the values of the critical currents of  $0$  and  $\pi$  regions in sample A at  $T_{\pi 0}$ . The inductance parameter of such a SQUID is  $\beta \approx 0.1$ , which means that the

minimum critical current in the node of the diffraction pattern is  $\approx 0.2I_c \approx 20 \mu\text{A}$  (see Figure 12.20 in reference [87]). The order of magnitude of the non-vanishing critical current is in good agreement with the experimental results in Figure 6.8.

### 6.3 Half-integer Shapiro steps in $0-\pi$ junctions

Another effect that can be explained by the presence of spontaneous currents was found in the phase dynamics of the Josephson phase of  $0-\pi$  junctions. At temperatures close to  $T_{\pi 0}$ , we have observed Shapiro steps at half-integer Josephson frequencies [95]. We believe these unusual resonances may arise from phase-locking of spontaneous currents to the applied driving frequency.

In the finite voltage state of a Josephson junction, the phase difference  $\phi$  winds uniformly according to the second Josephson relation (1.10). In other words, the phase difference  $\phi$  makes transitions between the potential wells of the Josephson energy (1.12), which are periodic in phase with a period of  $2\pi$ . The voltage across the junction  $V$  determines the phase winding rate, which we call the Josephson frequency:

$$f_J = \frac{2e}{h} V. \quad (6.6)$$

The time evolution of the Josephson phase changes qualitatively in the presence of an applied ac driving current. The Josephson frequency  $f_J$  locks onto the applied frequency  $f_{rf}$  whenever the resonance condition  $f_J = n f_{rf}$  is satisfied, where  $n = 0, 1, 2, \dots$ . These resonances can be seen in the current-voltage characteristics as sharp steps, which are called Shapiro steps [96].

Figure 6.9(a) shows a set of current-voltage characteristics for sample A measured in the presence of an applied rf current bias  $I_{rf}$  at  $T = 1.26 \text{ K}$ , far from  $T_{\pi 0}$ . Shapiro steps occur at voltages that correspond to Josephson frequencies equal to

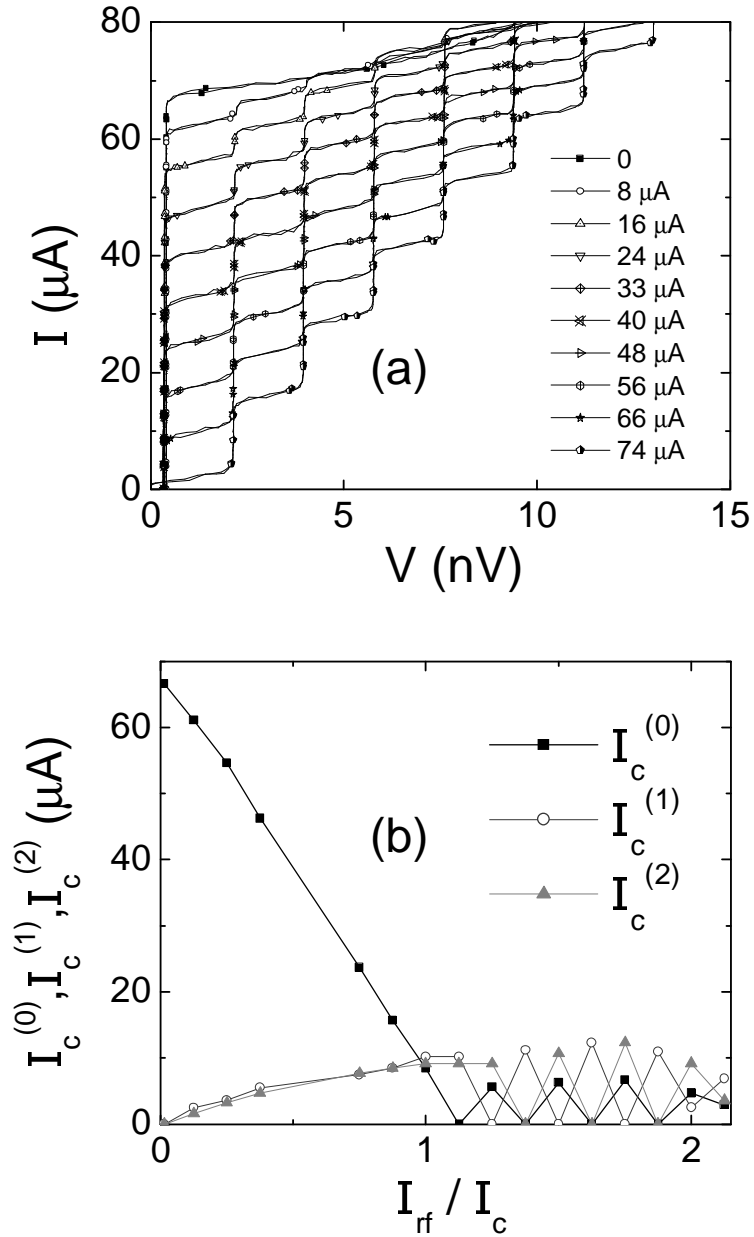


**Figure 6.9:** SAMPLE A. (a) Shapiro steps in the IV characteristics at  $T = 1.26\text{ K}$  for a range of rf currents  $I_{rf}$  0 - 74  $\mu\text{A}$  applied at a frequency of 800 kHz. (b) Amplitudes of the zero voltage critical current  $I_c^{(0)}$ , and of the first and the second Shapiro steps  $I_c^{(1)}, I_c^{(2)}$  as a function of the applied rf amplitude  $I_{rf}$  normalized by the critical current of the junction  $I_c$ .

integer multiples of the applied frequency  $f_{rf} = 800$  kHz. The amplitudes of Shapiro steps plotted in Figure 6.9(b) change with  $I_{rf}$  in a way expected for a current-biased Josephson junction [97].

At temperatures close to  $T_{\pi 0}$ , Shapiro steps at voltages corresponding to half-integer multiples of the applied frequency occur as demonstrated in Figure 6.10(a). Figure 6.10(b) shows the maximal amplitudes of the zero voltage critical current  $I_c^{(0)}$  and of the first integer and half-integer Shapiro steps  $I_c^{(0)}$  and  $I_c^{(1/2)}$  in the temperature interval around  $T_{\pi 0}$  for sample A. The rf bias current  $I_{rf}$  was adjusted in order to find the maximal amplitudes of both integer and half-integer steps at each temperature. The maximal amplitude of the first Shapiro step  $I_c^{(1)}$  follows the behavior of the critical current  $I_c = I_c^{(0)}$ : it reaches a minimum at  $T = T_{\pi 0}$  and increases as the temperature is moved away from  $T_{\pi 0}$ . In contrast, the maximal amplitude of the half-integer Shapiro step  $I_c^{(1/2)}$  peaks at  $T_{\pi 0}$  and vanishes at temperatures  $\approx 35$  mK higher and lower.

The temperature interval in which half-integer Shapiro steps were observed was 1.50 K - 1.57 K, which approximately coincides with the range in which spontaneous currents are expected to exist in sample A according to the model based on the Equations (6.5). From Figure 6.7(a) the range of temperature in which the junction crosses the phase of spontaneous currents is 1.53 K - 1.57 K.

In order to understand how spontaneously circulating currents may lead to half-integer Shapiro steps in  $0-\pi$  junctions we once again consider a  $0-\pi$  SQUID, in which a clear physical picture is easier to illustrate. The described phenomenon has the same nature in both  $0-\pi$  devices. The spontaneously circulating current in a  $0-\pi$  SQUID at zero field is given by:

$$J = \frac{I_c}{\beta} (\phi_0 - \phi_\pi). \quad (6.7)$$

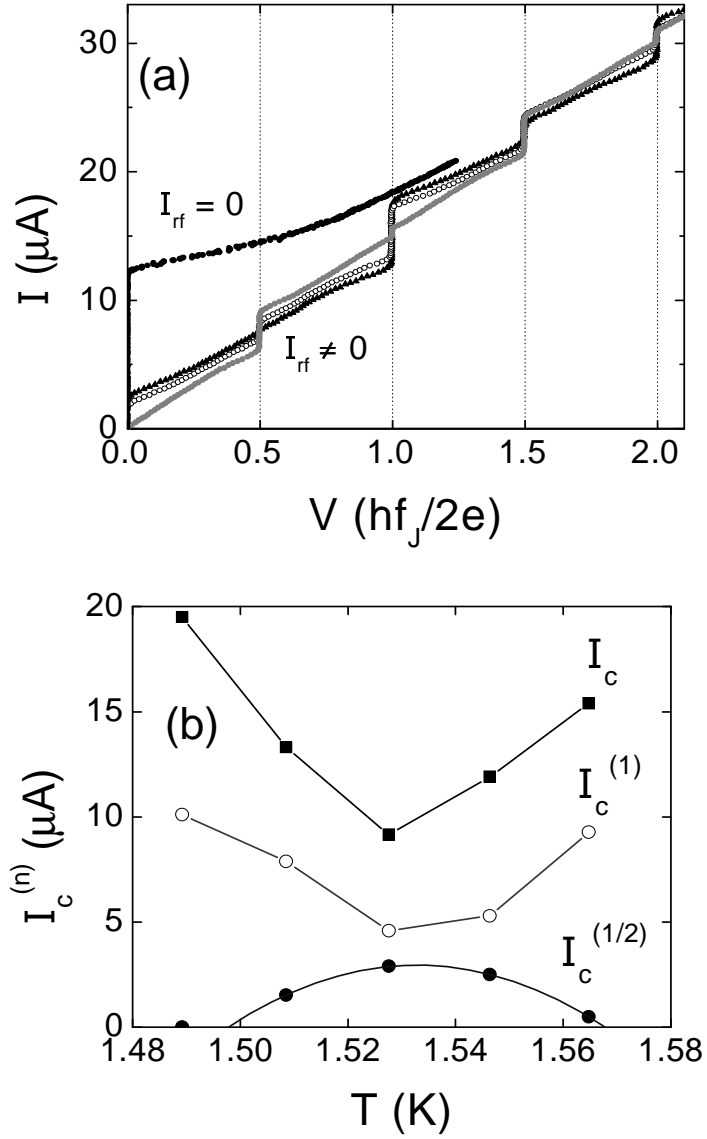


**Figure 6.10:** SAMPLE A. (a) Shapiro steps in the IV characteristics at  $T = 1.52$  K both at the usual voltages  $nhf_{\text{rf}}/2e$  and at half-integer values  $nhf_{\text{rf}}/4e$  for the drive frequency of 1.3 MHz. (b) Temperature dependence of the maximum (power-optimized) critical current steps, showing that the integer steps scale with the junction critical current whereas the half-integer steps only occur at temperatures near the minimum in the critical current.

In the state of uniform phase, in which  $\phi_0 = \phi_\pi = 0$  or  $\phi_0 = \phi_\pi = \pi$ , the spontaneous current  $J = 0$ . The energy landscape of a dc SQUID in the uniform phase regime is shown in Figure 2.6(a) for a 0-0 SQUID. The potential has minima with a period of  $2\pi$ . Under the influence of the applied rf current, the current-biased dc SQUID in a uniform phase state undergoes resonant transitions between the adjacent potential minima, which gives rise to Shapiro steps at voltages corresponding to the integer multiples of the driving frequency. Indeed, at each resonance the Josephson phase changes by integer multiples of  $2\pi$  during each period of the driving signal.

If the circulating current  $J$  is non-zero,  $\phi_\pi \neq \phi_0$ , the Josephson energy looks similar to the one shown in Figure 2.6(b). This potential has two off-diagonal minima in each  $2\pi$  period. Any two adjacent minima correspond to the opposite values of the difference  $\phi_0 - \phi_\pi$ , and hence to the opposite directions of the spontaneous current. In the finite voltage state, the 0- $\pi$  SQUID transitions between these  $\pi$ -periodic minima, and the spontaneous current flips its direction after each transition. When the rf drive is applied, the 0- $\pi$  SQUID junction phases lock onto an integer number of  $\pi$ -jumps during a period of the rf driving current. If in one period of the applied rf drive  $T_{rf}$  the 0- $\pi$  SQUID makes an even number of transitions  $2n$ , the phase across each junction changes by  $2n\pi$ . The voltage across the SQUID is given by

$$V_{even} = \frac{2n\pi}{T_{rf}} \cdot \frac{\hbar}{2e} = n f_{rf} \frac{h}{2e}, \quad (6.8)$$

corresponding to integer Shapiro steps. If the 0- $\pi$  SQUID makes an odd number of transitions  $2n + 1$  during each  $T_{rf}$ , the Josephson voltage corresponds to half-integer Shapiro steps:

$$V_{odd} = \frac{(2n + 1)\pi}{T_{rf}} \cdot \frac{\hbar}{2e} = \left(n + \frac{1}{2}\right) f_{rf} \frac{h}{2e}. \quad (6.9)$$

Half-integer Shapiro steps were observed in 0-0 SQUIDs in the applied magnetic flux of  $(1/2)\Phi_0$  [98], a system equivalent to a 0- $\pi$  SQUID in its energy landscape.

Measurements and simulations of the dc SQUID dynamics revealed that the magnitude of half-integer Shapiro steps increases as the inductance parameter  $\beta$  is increased and the asymmetry parameter  $\alpha$  is decreased. This is also the limit in which spontaneous currents are maximized. The amplitudes of spontaneous currents can therefore serve as a measure of the amplitudes of half-integer Shapiro steps, and *vice versa*, the presence of half-integer Shapiro steps in  $0-\pi$  structures near a symmetry point can be used as an indication of spontaneously circulating currents. No half-integer Shapiro steps were observed in samples B and C close to  $T_{\pi_0}$  in agreement with the assessment that spontaneous currents in these samples exist only in a very narrow temperature range on the order of 1 mK, and as a result do not have very large amplitudes.

The quantitative accuracy of the argument for the connection between the spontaneous currents and the half-integer Shapiro steps can be achieved if the dynamics of a long  $0-\pi$  junction is simulated. In order to accomplish that, Equations (6.4) should be solved numerically in the time domain in the presence of a periodic ac bias. In practice, a discrete model is typically used [63], in which a Josephson junction is represented by a  $1 \times N$  array. Some fraction of the junctions in the array can be  $\pi$  junctions, with the the rest being  $0$  junctions. Both dc and rf bias currents can be applied to the superconducting electrodes of the array and the Josephson equations for the array can be time stepped to find the time dependence of the N-dimensional array phase difference.

# Chapter 7

## Search for $\sin(2\phi)$ Current-Phase Relation

Higher order components of the form  $\sin(n\phi)$  are allowed and may be present in the current-phase relations of Josephson junctions far from  $T_c$ . Under most circumstances the sinusoidal term ( $n = 1$ ) dominates the CPR, but small distortions in the shape of the CPR could be observed due to higher order terms [45; 46].

An excellent opportunity to observe a CPR drastically different from sinusoidal is offered by Josephson junctions that exhibit transitions between 0 and  $\pi$  junction states. At the  $0$ - $\pi$  transition, the amplitude of the first order component in the CPR vanishes, and the second order component proportional to  $\sin(2\phi)$ , if present, may become the leading term. The first order term may go to zero under less exotic circumstances, such as in the nodes of the diffraction patterns. However, higher order terms are also expected to cancel in this case.

The amplitude of the  $\sin(2\phi)$  component is most generally given by the second order term in the expansion of the Josephson tunneling Hamiltonian and therefore corresponds to a coherent transfer of two Cooper pair across the barrier. Shortly after

the experimental demonstration of  $0-\pi$  transitions in SFS [18] and SNS [22] junctions, theoretical models predicting  $\sin(2\phi)$  current-phase relations for clean Josephson junctions in the  $0-\pi$  transition region were proposed [24; 39; 49].

Several important properties of the  $\sin(2\phi)$  CPR are the following. A CPR with a large  $\sin(2\phi)$  component may have an additional zero between  $\phi = 0$  and  $\phi = \pi$ , the Josephson energy in that case has local minima both at  $\phi = 0$  and at  $\phi = \pi$ . For a CPR given by (5.3) the critical current should not vanish completely at the  $0-\pi$  transition. Indeed, the  $\sin(\phi)$  term cannot compensate the  $\sin(2\phi)$  for all values of  $\phi$ . There always exists  $\phi_{max}$  for which  $I_s(\phi_{max}) \neq 0$ .

Measurements suggestive of the non-zero second order Josephson component were performed in quasiballistic SNS junctions with a control voltage channel [33]. The diffraction patterns of a dc SQUID containing two controllable SNS junctions of the type shown in Figure 1.3 were measured in a fixed bias current mode. One of the junctions was tuned through the  $0-\pi$  transition by an applied barrier control voltage  $V_c$ . Close to the  $0-\pi$  transition the period of the diffraction patterns was two times smaller than that far from the transition. Such behavior is a strong indication of a  $\sin(2\phi)$  component in the current-phase relation. However, non-vanishing critical currents were not observed at the  $0-\pi$  transition in experiments on single SNS junctions [19]. In addition, an effective  $\sin(2\phi)$  term may occur in  $0-\pi$  SQUIDs containing Josephson junctions of conventional sinusoidal CPR in the limit  $\beta \ll 1$  [99].

An experiment that involves only a single junction, such as the current-phase relation measurement, could be helpful in clarifying the issue of whether a microscopic  $\sin(2\phi)$  truly was observed in SNS junctions. Note that the measurement of Shapiro steps, which is a standard technique for investigating higher order components in the CPR, could turn out to be not suitable for this purpose. In clean SNS junctions half-integer Shapiro steps arising from phase-locking of the quasiparticle distribution in the

barrier to the driving signal were reported [100]. This non-equilibrium effect cannot be distinguished from an intrinsic  $\sin(2\phi)$  CPR component, which is also expected to produce Shapiro steps at half-integer Josephson voltages.

In SFS junctions, measurements of the current-phase relation near the second node of  $I_c(d)$  described in Chapter 5 provided no evidence for the second order Josephson component. This negative result was attributed to the fact that our samples were in the diffusive regime. Second order tunneling processes vanish more rapidly than the first order processes as the barrier thickness is increased. The first order term decays according to  $\exp(-d/\xi_{F1})$ , while the second order term is expected to decay with an exponentially faster rate proportional to  $\exp(-2d/\xi_{F1})$ .

A series of calculations done for diffusive junctions predicted that a measurable  $\sin(2\phi)$  should exist near the first node of the  $I_c(d)$  dependence [52–54]. The barriers are thinner near the first node, which increases the chances that second order processes may survive. The theoretical work was motivated by the experiments of Sellier et al. [101], who observed half-integer Shapiro steps and non-vanishing critical currents near the temperature minimum of the critical current. This data was closely reproduced in our experiments on non-uniform  $0-\pi$  junctions described in Chapter 6.

Both non-vanishing critical current and half-integer Shapiro steps near the apparent  $0-\pi$  transition are consistent with the  $\sin(2\phi)$  component being the dominant term in the CPR at the  $0-\pi$  transition. However, there are features both in our data and in the data by Sellier et al. which cast doubt on explanations of these effects that involve a local  $\sin(2\phi)$  component. In particular, in the experiments by Sellier et al. half-integer Shapiro steps were observed in a junction with  $d = 17$  nm and  $T_\pi \approx 1.1$  K, but not in the junction with  $d = 18$  nm and  $T_\pi \approx 4.5$  K. The barrier thicknesses in both samples were much larger than the order parameter decay length  $\xi_{F1}$  and the temperatures of the  $0-\pi$  transitions were of comparable value. Accidental

barrier non-uniformity provides a natural explanation for this seeming inconsistency (see Chapter 6). Based on the temperature range of half-integer Shapiro steps, the barrier non-uniformity in the sample with  $d = 17$  nm studied by Sellier et al. should be of the same order as in our sample A. It would be useful to perform careful measurements of the diffraction patterns on samples used by Sellier et al. to check for barrier non-uniformities that may lead to the  $0-\pi$  junction behavior. From our experience, it is difficult to avoid entering the  $0-\pi$  junction regime in junctions near the first node, since the Josephson effect is extremely sensitive to even angstrom-size effective roughness in the barrier thickness.

For a junction with a CPR (5.3), the maximal amplitudes of half-integer Shapiro steps are determined only by the amplitude of the second order component  $I_{c2}$ . The local  $\sin(2\phi)$  component is predicted to remain nearly constant in the wide temperature range far from  $T_c$ , meaning that half-integer Shapiro steps caused by a non-sinusoidal CPR should be observable at temperatures far from  $T_\pi$ . In contrast, experiments from both groups indicate that the half-integer Shapiro steps vanish completely within 50 mK of the temperature at which the minimum of the critical current is observed. Such behavior is, however, expected for  $0-\pi$  junctions that cross the region of spontaneously circulating currents in a narrow temperature in the vicinity of  $T_{\pi 0}$ .

The fact that the half-integer Shapiro steps and the non-vanishing currents were not observed in our experiments on more uniform samples B and C suggests that the observation of the true  $\sin(2\phi)$  component in SFS junctions based on CuNi alloys is challenging. From the measurements on samples B and C, we can estimate the upper bound limit of the critical current density of the  $\sin(2\phi)$  component at  $0.1 \text{ A/cm}^2$ . However, a proper test, which would be the measurement of the current-phase relation in uniform SFS junctions near the first node of  $I_c(d)$ , is still required in order to give the final answer. Measurement of the current-phase relation as described in Chapter

5 also has a higher critical current resolution than the transport measurement of Shapiro steps. At the time of the completion of this thesis, current-phase relation measurements on SFS junctions with  $d = 11$  nm were still ongoing in our research group.

Higher uniformity of tunneling barriers is essential to the correct interpretation of the current-phase relation data. Barrier non-uniformities may mimic the  $\sin(2\phi)$  behavior not only in the dynamic (Shapiro step) measurements, but even in the dc measurements, such as the measurements of the diffraction patterns and of the current-phase relation [93]. In order to evaluate the uniformity of the barrier, diffraction patterns should be measured together with the measurement of the current-phase relation. For that reason we have designed a sample in which the superconducting loop intended for the CPR measurement is initially open, allowing us first to do transport measurements. The loop can then be shorted in a separate superconductor deposition step in order to measure the CPR after the uniformity of the barrier is verified.

The conclusive observation of  $\sin(2\phi)$  is a tricky problem. Many effects can be confused with the microscopic  $\sin(2\phi)$  component. Therefore, careful and critical evaluation of the data is important. One might have better luck with observing  $\sin(2\phi)$  in SFS junctions if a different material is chosen for the barrier. In SFS junctions based on CuNi alloys, the decoherence of superconducting correlations is very high, above that expected for a simple diffusive barrier. The ferromagnetic coherence length  $\xi_{F1}$  is reduced compared to the order parameter oscillation length  $\xi_{F2}$  (see Figure 4.6) either due to inhomogeneous exchange interaction that comes from clustering of Ni ions [54], or due to spin-orbit scattering [53]. At the thickness of the first node of the  $I_c(d)$  dependence, which is set by  $\xi_{F2}$ , rapid decay of the order parameter characterized by  $\xi_{F1}$  suppresses higher order terms in the CPR.

A material such as  $Pd_{0.99}Fe_{0.01}$  appears to be an attractive candidate for the purpose of studying the second order tunneling. Palladium is nearly ferromagnetic, so that only a small percent of iron is required to push  $T_{Curie}$  up to 20-50 K in PdFe alloys. At such concentrations the alloy is more uniform, because Fe ions are dilute and have little chance for clustering. The relevance of spin-orbit scattering to these alloys is still to be considered.

It should be noted that even if the sources of excessive decoherence are removed from the barrier, the first  $0-\pi$  transition will occur at  $d \approx \pi\xi_{F1} \approx 3\xi_{F1}$ , where the decay of the second Josephson component can already be substantial. In the diffusive regime at zero temperature,  $\xi_{F1} = \xi_{F2}$ , but the first  $0-\pi$  transition occurs at thicknesses close to one half the period of the order parameter oscillation, which is  $2\pi\xi_{F2}$ . The first  $0-\pi$  transition thickness may become smaller depending on the condition of the SF interfaces, but it is unclear what would be the effect of finite barrier transparency on the amplitude of the  $\sin(2\phi)$  component.

# Chapter 8

## Experiments on Arrays of SFS

### Junctions

In this Chapter, we present the results of imaging of spontaneous currents in superconducting arrays that incorporate SFS  $\pi$  Josephson junctions. Our imaging tool is a scanning SQUID microscope, which acquires two-dimensional maps of the perpendicular magnetic field component in close proximity to the surface of the sample. In the  $\pi$  junction arrays magnetic fields are generated by spontaneous currents circulating in the array cells. The presence of spontaneous currents may be used as a direct evidence of the  $\pi$  junction state. Information about the distribution of spontaneous currents allows one to study the disorder in the junctions' critical currents, and the knowledge of spontaneous current configurations could be important for testing the predictions of the XY-model with negative bonds [102–104]. Scanning SQUID microscopy was used in the past to image spontaneous currents due to  $\pi$  shifts in superconducting d-wave/s-wave arrays [105]. Data presented in this Chapter was obtained in cooperation with M.J.A. Stoutimore.

## 8.1 Imaging arrays with a scanning SQUID microscope

The scanning SQUID microscope (SSM) is a two-dimensional scanning system with magnetic flux sensitivity of  $10^{-5} \Phi_0$  and spatial resolution of approximately  $10 \mu\text{m}$ . The SSM, which employs a dc SQUID as a sensor, is a perfect magnetic imaging instrument for studying superconducting arrays of Josephson junctions. The typical cell sizes of the arrays made by optical lithography are  $10 - 50 \mu\text{m}$ , and the magnetic flux signal from a single  $2\pi$  phase winding in an array cell can be as small as  $10^{-3} \Phi_0$ , because the maximal circulating current in the superconducting state is limited by the critical current.

The prototype SSM was built by Vu and Van Harlingen [106], and was used to image currents induced by the applied magnetic field in superconducting Nb networks with a cell size of  $20 \mu\text{m} \times 20 \mu\text{m}$  [107]. Based on the early design, M. S. Wistrom developed another scanning SQUID microscope that is currently in use in our research group. Its design is thoroughly described in reference [108]. Originally, imaging was done by scanning the SQUID over the sample. That technique resulted in large gradients in the signal as the SQUID was sampling the spatial variations in the magnetic field that was applied to the sample from a Helmholtz coil. The SSM was modified by W. K. Neils, A. Ruosi and M.P. Stehno to keep the SQUID at a fixed position and move the sample instead.

The diagram in Figure 8.1(a) illustrates the basics of the SSM operation. A sensor consisting of a magnetic flux pickup loop coupled to a dc SQUID via a flux transformer rests on the surface of the sample at a small angle. The sensor is fabricated on a Si wafer, which is connected to a fixed copper arm via a flexible mylar hinge. The sample is placed on a stage that can be scanned both in x and y directions via

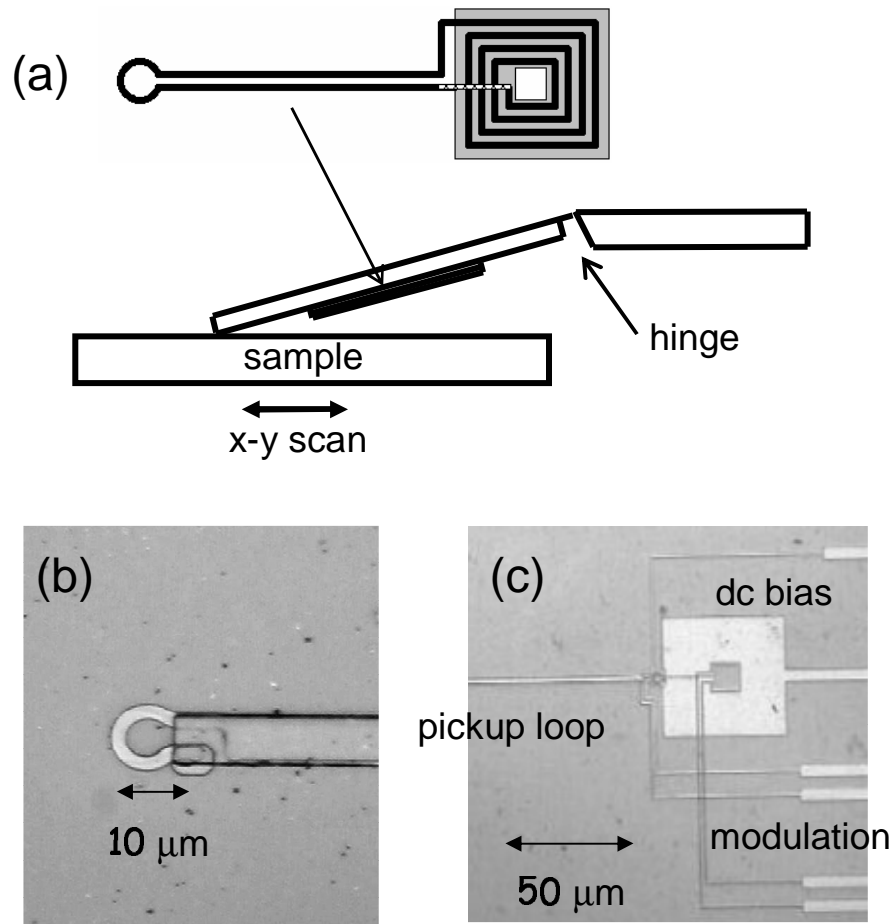


**Figure 8.1:** (a) Diagram of the scanning SQUID microscope operation. (b) Optical micrograph of the magnetic flux pickup loop. (c) Optical micrograph of the SSM dc SQUID sensor with the flux transformer.

stepper motors located at the top of the insert at room temperature. The mechanical gearing system results in a minimum step size of  $0.1 \mu\text{m}$  and a maximum scan window of  $5 \text{ mm} \times 5 \text{ mm}$ . The sample space is enclosed in a vacuum can, and the sample stage can be heated to do measurements at temperatures above the helium bath temperature. The base temperature of the SSM is 1.5 K. The SSM operates in a glass LHe<sup>4</sup> dewar with both  $\mu$ -metal and superconducting shielding. A uniform magnetic field up to 50 G can be applied to the sample from a superconducting Helmholtz coil.

The dc SQUID sensors for our SSM were fabricated by A. Ruosi, C. Granata and M. Russo at the National Institute for the Physics of Matter (INFM), National Research Center (CNR) at Naples, Italy according to the design developed by W. Neils. Optical micrographs of an SSM sensor are presented in Figures 8.1(b) and 8.1(c). A superconducting magnetic flux pickup loop is directly connected to a shunted dc SQUID in the gradiometer configuration via self-screening superconducting leads which are 5 mm long. The superconducting leads are fabricated on top of each other to ensure that the pickup of external magnetic flux occurs predominantly in the pickup loop. For the same reason the pickup loop is removed as far as possible from the dc SQUID. The dc SQUID parameters are chosen in a way that allows the readout via commercially available Quantum Design dc SQUID amplifier electronics.

In order to obtain a measurable signal from the magnetic field generated by the sample, the sensor must be placed within a pickup loop diameter from the sample surface. The edges of the sensor chip are polished at an angle so that the tip of the bevel is within  $100 \mu\text{m}$  of the pickup loop. The sensor rests on the surface of the sample so that the point of contact is at the tip of the bevel. In this configuration, the pickup loop is within approximately  $5 \mu\text{m}$  of the sample.

Optical micrographs of SFS junction arrays are shown in Figure 8.2. These samples were fabricated in the group of Professor Ryazanov in Chernogolovka, Russia

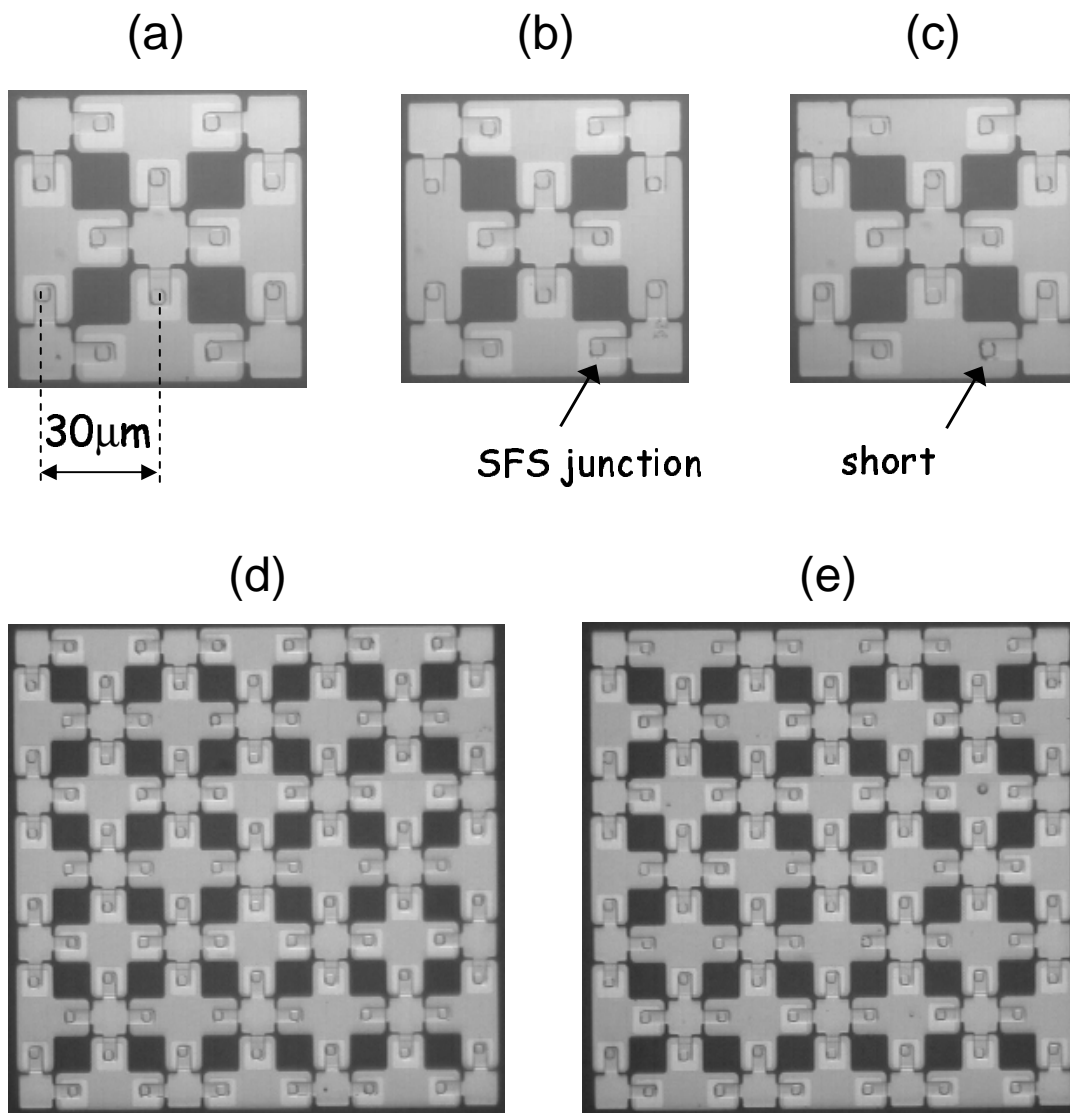


**Figure 8.2:** Superconducting arrays of SFS Josephson junctions (a)  $2 \times 2$  unfrustrated array (b)  $2 \times 2$  fully frustrated array (c)  $2 \times 2$  checkerboard frustrated array (d)  $6 \times 6$  fully frustrated array (e)  $6 \times 6$  checkerboard frustrated array.

in a layer-by-layer process described in Chapter 4. The wide T-shaped base superconducting electrodes in Figures 8.2(a)(b)(c) have the a width of  $15 \mu\text{m}$ , and define the area of each cell to be  $30 \mu\text{m} \times 30 \mu\text{m}$ . The dimensions of one cell are the same for both large and small arrays. Not shown in Figure 8.2 are various types of  $3 \times 3$  arrays and  $1 \times 20$  arrays. The lighter squares that appear in the overlap areas of the base and the top superconducting electrodes are the ferromagnetic CuNi barriers of the junctions. Note that in Figures 8.2(b)-(e) the CuNi squares are not present in every arm of each cell. In SiO windows like the one indicated in Figure 8.2(c), the two superconductors overlap directly, creating a superconducting short instead of an SFS junction. By choosing where to put CuNi barriers, the number of SFS junctions in a cell can be controlled across the array. In the array in Figure 8.2(a) each cell has four SFS junctions, while in the array in Figure 8.2(b) each cell has three SFS junctions.

Following the notation developed in Chapter 2, we call a cell with an even number of SFS junctions *unfrustrated*, and those with an odd number are *frustrated*. The array in Figure 8.2(a) is unfrustrated, (b) is fully frustrated and (c) is checkerboard frustrated, because every other cell in this array has an odd number of SFS junctions. The larger arrays in Figures 8.2(d) and 8.2(e) are fully frustrated and checkerboard frustrated respectively. When SFS junctions are  $\pi$  junctions, spontaneous current will be generated in each frustrated cell, and the unfrustrated cells will contribute no signal.

Figure 8.3 illustrates the measurement of spontaneous currents in a fully frustrated array with SFS junctions in the  $\pi$  state. The scanning SQUID microscope pickup loop is drawn to the correct relative scale. Spontaneous current follows the path around the edges of the superconductor indicated by the dashed line. The magnetic flux threading the pickup loop corresponds to the magnetic field integrated over the

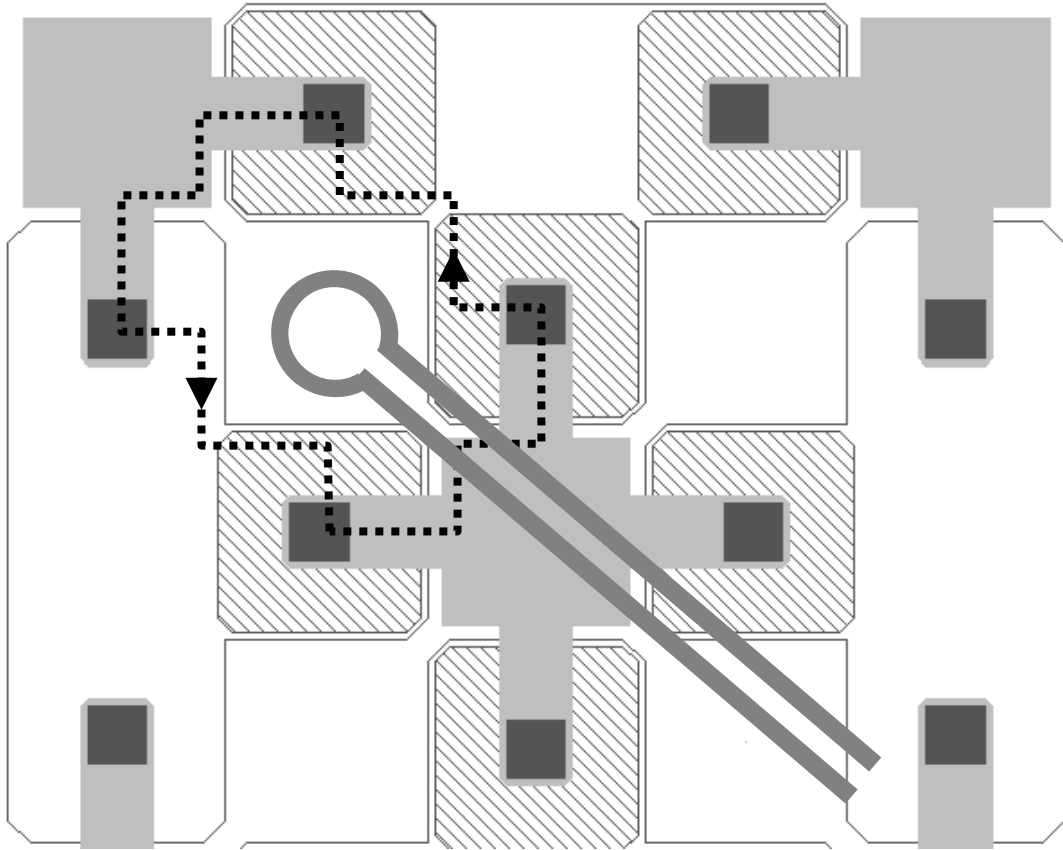


**Figure 8.3:** A sketch view of the scanning SQUID microscope pickup coil positioned over an SFS array of  $\pi$  junctions. The dashed line shows the path of spontaneous current around a frustrated cell of the array.

pickup loop area. Roughly, the signal in the SQUID sensor is a measure of the magnetic field in the center of the pickup loop. However, changes in the magnetic field on a scale smaller than the pickup loop diameter become smeared, so that the true spatial resolution of the microscope is determined by the size of the pickup loop. For our arrays this means that small features in the cell geometry do not appear in the images.

One of the amazing features of a scanning SQUID microscope is its ability to visualize the underlying superconducting structure of the array electrodes. In finite background magnetic field, screening currents circulate in the sensor pickup loop due to the Meissner effect. The proximity of the superconducting material of the array changes the effective inductance of the pickup loop, which changes the screening current. Those variations in the screening current can reproduce the image of the superconducting electrodes of the array.

Figure 8.4(a) shows an image of a  $6 \times 6$  unfrustrated array where the external magnetic field has been zeroed by passing a small current through the Helmholtz coil. As one would expect, the image has no contrast. However, if a small magnetic field is applied, the superconducting structure becomes visible in the data obtained by scanning the same area (Figure 8.4(b)). The absence of contrast in the images of unfrustrated arrays was used to gauge zero field. We also used finite contrast of the superconducting structures to our advantage, as it allowed us to easily identify various types of arrays in the images.

## 8.2 Spontaneous currents in SFS $\pi$ junction arrays

All of the arrays that we imaged were fabricated on the same chip with the Josephson junctions near the first node of the  $I_c(d)$  dependence, where the  $\pi$  junction state is

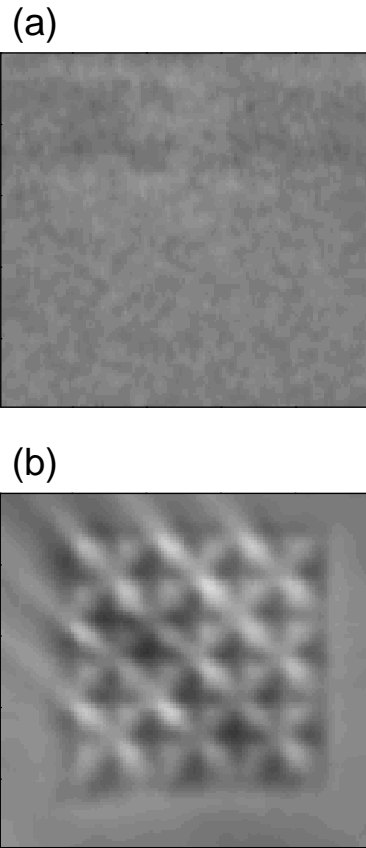


**Figure 8.4:** Scanning SQUID microscope image of a  $6 \times 6$  unfrustrated array (a) in zero field and (b) in a small magnetic field showing finite contrast from the superconductor in the array.

the state below  $T_\pi$ . The single junction fabricated on this chip for testing purposes is sample C described in Chapter 6. This junction is a  $0-\pi$  junction in the wide temperature range of  $\approx 2$  K. However, the temperature region of non-uniform phase distribution around  $T_{\pi 0}$  is only 3 mK wide. Outside this range, the phase difference across the entire junction is zero above  $T_{\pi 0}$  and  $\pi$  below  $T_{\pi 0}$ . We can therefore ignore the effects associated with non-uniformities in the junction barriers when dealing with phase coherence around the array cell. The degree of ferromagnetic barrier nonuniformity should be comparable in all junctions on this chip, because they underwent the same processing steps.

The temperature dependence of the zero-field critical current for sample C measured during the period of SSM experiments is shown in Figure 4.8. This dependence is useful for estimating both the inductance parameter  $\beta$  and the interactions between spontaneous currents in the neighboring cells. The temperature  $T_{\pi 0}$  of sample C was around 2.5 K, but spontaneous currents were observed in the arrays at  $T = 3$  K. This is probably a consequence of small gradients in the ferromagnetic film thickness across the  $15 \text{ mm} \times 15 \text{ mm}$  Si substrate. Overall, the  $0-\pi$  transition temperature varied by approximately 1 K between arrays in the center of the substrate and those closer to the edges.

From the temperature dependence of the critical current of the test sample, we can conclude that the critical currents of the junctions in the arrays are approximately  $70 \mu\text{A}$  at  $T = 1.5$  K, the base temperature of the SSM. The geometric inductance of one array cell is on the order of 100 pH. Based on these numbers, the inductance parameter  $\beta$  of a single array cell is  $\beta \sim 20$ . The arrays are in the highly hysteretic regime at low temperatures, and the spontaneous flux induced in each cell by  $\pi$  junctions should be very close to  $0.5 \Phi_0$  (see Figure 2.4(a)).

We can use the scanning SQUID microscope data at the base temperature to

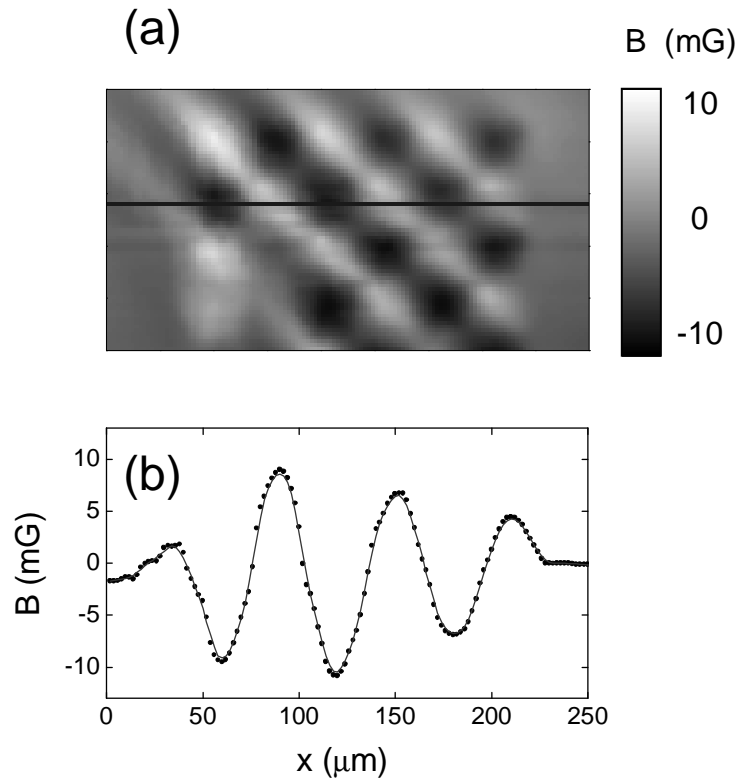


**Figure 8.5:** (a) SSM image of a portion of a  $6 \times 6$  fully-frustrated array with antiferromagnetic arrangement of spontaneous magnetic flux (b) Average magnetic field along a single scan line indicated in panel (a) by a black line.

perform an order of magnitude calibration of the sensor. In a large array, for a cell far from the edges of the array the sensor signal integrated over the cell area is equal to a magnetic flux of half a flux quantum. The magnetic field in the center of a cell should be on the order of 10 mG. A calibration of this kind is rather crude, and certainly is not sufficient to distinguish an integer flux quantum vortex from a half-integer one. Such a degree of precision is not necessary for the purposes of our experiments, because the information about the sign of the critical current is obtained from the symmetry of spontaneous current arrangements, rather than from the magnitude of spontaneous currents.

Figure 8.5(a) shows a scanning SQUID microscope image of a portion of a  $6 \times 6$

fully-frustrated array acquired at  $T = 1.5$  K. The currents circulating in the cells of the array show up as black or white squares in the image, depending on the sign of the magnetic flux they produce. The magnetic flux pattern is antiferromagnetic, with the circulating currents changing directions in the adjacent cells. This is expected for the ground state of a fully-frustrated array. No circulating currents are visible in the two cells in the lower left corner. This is most likely due to fabrication defects, as some of the windows in the insulating SiO do not lift off. This leads to a creation of open cells, in which the base superconductor is not electrically connected to the top superconductor. The spatial dimensions of the image are calibrated by the periodicity of magnetic flux pattern which coincides with the periodicity of the array. We also know the image size independently from the step size of the stepper motors. The two values are in agreement.

The magnetic field profile along the line passing roughly through the centers of the cells in one row of the array is shown in Figure 8.5(b). The peaks of magnetic field are smaller in the edge cells due to the magnetic flux leaking to the outside of the array. The peaks also get smaller in the cells on the right because the scan did not go exactly through the centers of those cells. In other images, we saw scatter in the amplitudes of the magnetic field peaks in different cells. This effect is likely caused by variations in the critical currents of Josephson junctions, which translate into variations in the effective cell inductances.

The antiferromagnetic magnetic flux pattern in Figure 8.5(a) does not constitute a definite proof of the  $\pi$  junction state, because the same pattern can be created by screening currents in an array of 0 junctions in the applied magnetic flux of  $1/2 \Phi_0$  per cell. Arrays with non-uniform frustration are more suitable for the “single-shot” determination of the sign of the critical current.

In Figure 8.6 a scanning SQUID microscope image showing several  $2 \times 2$  arrays is

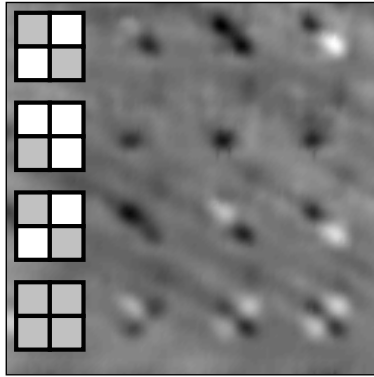


**Figure 8.6:** Scanning SQUID microscope image of a variety of  $2 \times 2$  arrays. The frustration patterns are indicated by the diagrams in the left column. The image is acquired at  $T = 1.5$  K.

presented. Arrays in each row of the image are fabricated with a different frustration pattern, achieved by replacing some of the Josephson junctions in the array arms with superconducting shorts. The types of frustration embedded in the array designs are indicated by the diagrams in the left column. The shaded squares in the diagrams are the frustrated cells with 3 Josephson junctions, the white squares are the unfrustrated cells with either 2 or 4 Josephson junctions. The image reveals that circulating currents appear only in the cells with odd numbers of Josephson junctions. This is only possible if the Josephson junctions are in the  $\pi$  junction state. We have observed no spontaneous magnetic flux in any of the unfrustrated arrays.

This image was taken in zero magnetic field, therefore in many of the arrays the magnetic flux is oriented antiferromagnetically. However, several of the checkerboard frustrated arrays are not in the ground state. In checkerboard frustrated arrays the antiferromagnetic configuration with nearest frustrated cells having opposite spontaneous magnetic flux is the ground state. But the ferromagnetic state, with all magnetic moments pointing in the same direction, is not much higher in energy than the ground state. This is related to the fact that in checkerboard frustrated arrays the mutual inductance of the two nearest frustrated cells is small, because they do

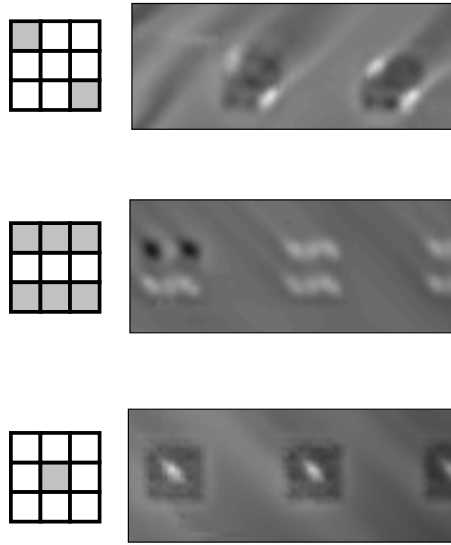


**Figure 8.7:** Scanning SQUID microscope image of a variety of  $3 \times 3$  arrays. The frustration patterns are indicated by the diagrams in the left column. The image is acquired at  $T = 1.5$  K and in a small uniform magnetic field.

not share junctions or inductors. There are two types of coupling between magnetic moments in the nearest frustrated cells of checkerboard frustrated arrays - the direct magnetic coupling of spontaneous currents, and the phase-coherent coupling through the neighboring unfrustrated cells. Both types of coupling are relatively weak in our arrays.

The ferromagnetic arrangement of magnetic flux can also be made the preferred state in finite magnetic field. Figure 8.7 shows several  $3 \times 3$  arrays in the presence of a small magnetic field. Note that the underlying superconducting structure of the arrays can be seen at the same time with the spontaneous magnetic flux. Most of the magnetic moments due to circulating currents are oriented in the positive direction, suggesting that the background field is positive. In this image the designed frustration is also perfectly reproduced in the spontaneous flux patterns.

In Figure 8.7 the white “tails” can be seen extending from every spontaneous vortex at a 45 degree angle. These stray signals are related to the magnetic flux

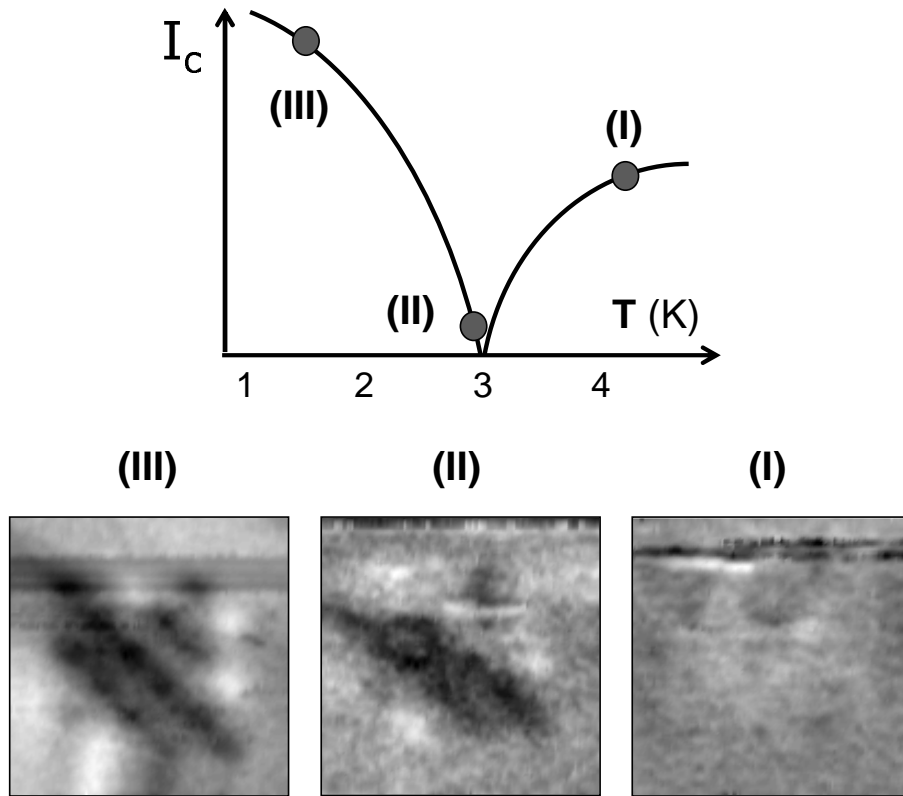


**Figure 8.8:** Scanning SQUID microscope images of a  $6 \times 6$  checkerboard frustrated array taken at temperatures (I)  $T = 4$  K above the  $0-\pi$  transition in the  $0$  junction state (II)  $T = 2.8$  K close to the  $0-\pi$  transition in the  $\pi$  junction state and (III)  $T = 1.5$  K below the  $0-\pi$  transition in the  $\pi$  junction state.

pickup in the leads of the pickup coil. For example, in Figure 8.3 the pickup coil is measuring the magnetic field in the upper left cell of the array, but the pickup coil leads are located at a 45 degree angle over the lower right cell. The total signal in the SQUID sensor in this case has a small contribution from the magnetic flux in the lower right cell. Careful screening of the sensor leads and of the sensor itself may help reduce these “ghost” signals.

Proximity to the  $0-\pi$  transition thickness allows us to monitor how the spontaneous magnetic flux turns on as the arrays are cooled through the  $0-\pi$  transition. Figure 8.8 shows the temperature evolution of the magnetic flux pattern of a  $6 \times 6$  checkerboard frustrated array at temperatures above and below  $T_{\pi 0}$ . At  $T = 4$  K, the image has

zero contrast showing only the magnetic noise in the SQUID sensor. At  $T = 2.8$  K the image is qualitatively different - the dark and light regions appear - however single vortices cannot be distinguished. At this temperature the inductance parameter  $\beta$  of a single array cell is very small, because the critical currents are small. The spontaneous magnetic flux from a single cell is substantially reduced. At the base temperature of the SSM  $T = 1.5$  K the checkerboard magnetic flux pattern is discernible. The magnetic flux configuration is neither ferromagnetic nor antiferromagnetic. In large arrays, excited states form bands of closely spaced energy levels, as was illustrated by the simulation in Figure 2.10. Due to the high degeneracy of states, it is difficult to find an array in any symmetric configuration of spontaneous flux. Because the spontaneous flux signal is very small close to  $T_{\pi_0}$ , imaging of SFS arrays turned out to be not a very accurate way of measuring  $T_{\pi_0}$ . In our arrays, we could roughly estimate  $T_{\pi_0}$  to be close to  $T = 3$  K.

Further experiments involving the dynamics of spontaneous current configurations, the temperature dependence of the spontaneous currents and the magnetic field evolution and statistics of the array states are among the future directions of our work on SFS Josephson junction arrays.

# References

- [1] H. Kamerlingh Onnes, Commun. Phys. Lab. Univ. Leiden **124c**, 1 (1911).
- [2] J. Bardeen, L. N. Cooper, and J. R. Schrieffer, Phys. Rev. **108**, 1175 (1957).
- [3] F. London and H. London, Proc. Roy. Soc. **A141**, 547 (1935).
- [4] V. L. Ginzburg and L. D. Landau, Zh. Eksp. Teor. Fiz. **20**, 1064 (1950).
- [5] L. G. Aslamazov and A. I. Larkin, JETP Lett. **9**, 150 (1969).
- [6] J. R. Waldram, Rep. Prog. Phys. **39**, 751 (1976).
- [7] B. D. Josephson, Phys. Lett. **1**, 251 (1962).
- [8] K. K. Likharev, Rev. Mod. Phys. **51**, 101 (1979).
- [9] L. N. Bulaevskii, V. V. Kuzii, and A. A. Sobyenin, JETP Lett. **25**, 290 (1977).
- [10] I. O. Kulik, Soviet Physics JETP **22**, 841 (1966).
- [11] V. Ambegaokar and A. Baratoff, Phys. Rev. Lett. **10**, 486 (1963).
- [12] A. A. Abrikosov and L. P. Gor'kov, Sov. Phys. JETP **10**, 593 (1960).
- [13] L. I. Glazman and K. A. Matveev, JETP Lett. **49**, 659 (1989).
- [14] F. Siano and R. Egger, Phys. Rev. Lett. **93**, 047002 (2004).
- [15] A. I. Buzdin, L. N. Bulaevskii, and S. V. Panjukov, JETP Lett. **35**, 178 (1982).
- [16] A. I. Larkin and Y. N. Ovchinnikov, Sov. Phys. JETP **20**, 762 (1965).
- [17] P. Fulde and R. Ferrell, Phys. Rev. **135**, A550 (1964).
- [18] V. V. Ryazanov, V. A. Oboznov, A. Y. Rusanov, A. V. Veretennikov, A. A. Golubov, and J. Aarts, Phys. Rev. Lett. **86**, 2427 (2001).
- [19] J. J. A. Baselmans, B. J. van Wees, and T. M. Klapwijk, Phys. Rev. B **65**, 22413 (2002).

- [20] A. F. Volkov, Phys. Rev. Lett. **74**, 4730 (1995).
- [21] A. F. Andreev, Sov. Phys. JETP **19**, 1228 (1964).
- [22] J. J. A. Baselmans, A. F. Morpurgo, B. J. van Wees, and T. M. Klapwijk, Nature **397**, 43 (1999).
- [23] J. Huang, F. Pierre, T. T. Heikkilä, F. K. Wilhelm, and N. O. Birge, Phys. Rev. B **66**, 020507(R) (2002).
- [24] T. T. Heikkilä, F. K. Wilhelm, and G. Schön, Europhys. Lett. **51**, 434 (2000).
- [25] J. G. Bednorz and K. A. Müller, Z. Phys. **64**, 189 (1986).
- [26] D. J. Van Harlingen, Rev. Mod. Phys. **67**, 515 (1995).
- [27] C. C. Tsuei and J. R. Kirtley, Rev. Mod. Phys. **72**, 969 (2000).
- [28] Y. S. Barash, H. Burkhardt, and D. Rainer, Phys. Rev. Lett. **77**, 4070 (1996).
- [29] T. Löfwander, V. S. Shumeiko, and G. Wendin, Supercond. Sci. Technol. **14**, R53 (2001).
- [30] E. Il'ichev, M. Grajcar, R. Hlubina, R. P. J. IJsselsteijn, H. E. Hoenig, H. Meyer, A. Golubov, M. H. S. Amin, A. M. Zagorskin, A. N. Omelyanchouk, et al., Phys. Rev. Lett. **86**, 5369 (2001).
- [31] G. Testa, E. Sarnelli, A. Monaco, E. Esposito, M. Ejrnaes, D.-J. Kang, S. Menema, E. Tarte, and M. Blamire, Phys. Rev. B **71**, 134520 (2005).
- [32] H. Hilgenkamp and J. Mannhart, Rev. Mod. Phys. **74**, 486 (2002).
- [33] J. J. A. Baselmans, T. T. Heikkilä, B. J. van Wees, and T. M. Klapwijk, Phys. Rev. Lett. **89**, 207002 (2002).
- [34] D. A. Wollman, D. J. Van Harlingen, W. C. Lee, D. M. Ginsberg, and A. J. Leggett, Phys. Rev. Lett. **71**, 2134 (1993).
- [35] J. C. Davis and R. E. Packard, Rev. Mod. Phys. **74**, 741 (2002).
- [36] O. Avenel, Y. Mukharsky, and E. Varoquaux, Physica B **280**, 130 (2000).
- [37] S. Backhaus, S. Pereverzev, R. W. Simmonds, A. Loshak, J. C. Davis, and R. E. Packard, Nature **392**, 687 (1998).
- [38] A. Marchenkov, R. W. Simmonds, S. Backhaus, A. Loshak, J. C. Davis, and R. E. Packard, Phys. Rev. Lett. **83**, 3860 (1999).

- [39] Z. Radovic, L. Dobrosavljevic-Grujic, and B. Vujicic, *Phys. Rev. B* **63**, 214512 (2001).
- [40] A. A. Golubov, M. Y. Kupriyanov, and E. Il'ichev, *Rev. Mod. Phys.* **76**, 411 (2004).
- [41] I. O. Kulik, *Soviet Physics JETP* **30**, 944 (1969).
- [42] C. Ishii, *Progr. Theoret. Phys.* **44**, 1525 (1970).
- [43] J. Bardeen and J. L. Johnson, *Phys. Rev. B* **5**, 72 (1972).
- [44] W. Haberkorn, H. Knauer, and J. Richter, *Phys. Status Solidi A* **47**, K161 (1978).
- [45] R. Rifkin and B. S. Deaver, *Phys. Rev. B* **13**, 3894 (1976).
- [46] M. C. Kooops, G. V. van Duyneveldt, and R. de Bruyn Ouboter, *Phys. Rev. Lett.* **77**, 2542 (1996).
- [47] A. A. Zubkov and M. Y. Kupriyanov, *Sov. J. Low Temp. Phys.* **9**, 279 (1983).
- [48] Y. S. Barash and I. V. Bobkova, *Phys. Rev. B* **65**, 144502 (2002).
- [49] N. M. Chtchelkatchev, W. Belzig, Y. Y. Nazarov, and C. Bruder, *JETP Lett.* **74**, 323 (2001).
- [50] Z. Radovic, N. Lazarides, and N. Flytzanis, *Phys. Rev. B* **68**, 014501 (2003).
- [51] A. A. Golubov, M. Y. Kupriyanov, and Y. V. Fominov, *JETP Lett.* **75**, 588 (2002).
- [52] R. Mélin, *Europhys. Lett.* **69**, 121 (2005).
- [53] A. I. Buzdin, *cond-mat/0505549* (2005).
- [54] M. Houzet, V. Vinokur, and F. Pistolesi, *cond-mat/0505514* (2005).
- [55] S. M. Frolov, D. J. Van Harlingen, V. A. Oboznov, V. V. Bolginov, and V. V. Ryazanov, *Phys. Rev. B* **70**, 144505 (2004).
- [56] A. Bauer, J. Bentner, M. Aprili, M. L. Della Rocca, M. Reinwald, W. Wegscheider, and C. Strunk, *Phys. Rev. Lett.* **92**, 217001 (2004).
- [57] L. B. Ioffe, V. B. Geshkenbein, M. V. Feigelman, A. L. Fauchere, and G. Blatter, *Nature* **398**, 679 (1999).
- [58] E. Terzioglu and M. R. Beasley, *IEEE Trans. Appl. Supercond.* **8**, 48 (1998).

- [59] G. Blatter, V. B. Geshkenbein, and L. B. Ioffe, *Phys. Rev. B* **62**, 174511 (2001).
- [60] A. V. Ustinov and V. K. Kaplunenko, *J. Appl. Phys.* **94**, 5405 (2001).
- [61] M. Tinkham, *Introduction to Superconductivity, 2nd Edition* (McGraw-Hill, 1996).
- [62] W. Guichard, M. Aprili, O. Bourgeois, T. Kontos, J. Lesueur, and P. Gandit, *Phys. Rev. Lett.* **90**, 167001 (2003).
- [63] K. N. Springer, Ph.D. thesis, University of Illinois (1988).
- [64] E. A. Demler, G. Arnold, and M. R. Beasley, *Phys. Rev. B* **55**, 15174 (1997).
- [65] A. Buzdin, *Phys. Rev. B* **62**, 11377 (2000).
- [66] T. Kontos, M. Aprili, J. Lesueur, and X. Grison, *Phys. Rev. Lett.* **86**, 304 (2001).
- [67] T. Kontos, M. Aprili, J. Lesueur, X. Grison, and L. Dumoulin, *Phys. Rev. Lett.* **93**, 137001 (2004).
- [68] A. I. Buzdin and M. Y. Kupriyanov, *JETP Lett.* **52**, 487 (1990).
- [69] J. S. Jiang, D. Davidovic, D. H. Reich, and C. L. Chien, *Phys. Rev. Lett.* **74**, 314 (1995).
- [70] V. V. Ryazanov, V. A. Oboznov, A. S. Prokofiev, V. V. Bolginov, and A. K. Feofanov, *J. Low Temp. Phys.* **136**, 385 (2004).
- [71] V. V. Ryazanov et al. (unpublished).
- [72] T. Kontos, M. Aprili, J. Lesueur, F. Genet, B. Stephanidis, and R. Boursier, *Phys. Rev. Lett.* **89**, 173007 (2002).
- [73] H. Sellier, C. Baraduc, F. Lefloch, and R. Calemczuk, *Phys. Rev. B* **68**, 054531 (2003).
- [74] G. Eilenberger, *Z. Phys.* **214**, 196 (1968).
- [75] K. D. Usadel, *Phys. Rev. Lett.* **25**, 507 (1970).
- [76] A. I. Buzdin and M. Y. Kupriyanov, *JETP Lett.* **53**, 321 (1991).
- [77] A. I. Buzdin, *Rev. Mod. Phys.* (2005).
- [78] V. V. Ryazanov, V. A. Oboznov, A. Y. Rusanov, A. V. Veretennikov, A. A. Golubov, and J. Aarts, *Usp. Fiz. Nauk (Suppl.)* **171**, 81 (2001).

- [79] Y. Blum, A. Tsukernik, M. Karpovski, and A. Palevski, *Phys. Rev. Lett.* **89**, 187004 (2002).
- [80] C. Bell, R. Loloee, G. Burnell, and M. G. Blamire, *Phys. Rev. B* **71**, 180501(R) (2005).
- [81] L. D. Jackel, R. A. Buhrman, and W. W. Webb, *Phys. Rev. B* **10**, 2782 (1974).
- [82] J. R. Waldram and J. M. Lumley, *Rev. Phys. Appl.* **10**, 7 (1975).
- [83] A. H. Silver and J. E. Zimmerman, *Phys. Rev.* **157**, 317 (1967).
- [84] D. J. Van Harlingen, J. E. Hilliard, B. L. T. Plourde, and B. D. Yanoff, *Physica C* **317-318**, 410 (1999).
- [85] R. de Bruyn Ouboter and A. N. Omelyanchouk, *Physica B* **216**, 37 (1995).
- [86] V. V. Ryazanov, V. A. Oboznov, A. V. Veretennikov, and A. Y. Rusanov, *Phys. Rev. B.* **65**, 020501(R) (2001).
- [87] A. Barone and G. Paterno, *Physics and Applications of the Josephson effect* (Wiley, 1982).
- [88] A. Buzdin and I. Baladie, *Phys. Rev. B* **62**, 184519 (2000).
- [89] D. A. Wollman, D. J. Van Harlingen, J. Giapintzakis, and D. M. Ginsberg, *Phys. Rev. Lett.* **74**, 797 (1995).
- [90] J. H. Xu, J. H. Miller, and C. S. Ting, *Phys. Rev. B* **51**, 11985 (1995).
- [91] J. R. Kirtley, K. A. Moler, and D. J. Scalapino, *Phys. Rev. B* **56**, 886 (1997).
- [92] L. N. Bulaevskii, V. V. Kuzii, and A. A. Sobyenin, *Solid State Commun.* **25**, 1053 (1978).
- [93] A. Buzdin and A. E. Koshelev, *Phys. Rev. B* **67**, 220504(R) (2003).
- [94] M. L. Della Rocca, M. Aprili, T. Kontos, A. Gomez, and P. Spathis, *Phys. Rev. Lett.* **94**, 197003 (2005).
- [95] S. M. Frolov, D. J. Van Harlingen, V. V. Bolginov, V. A. Oboznov, and V. V. Ryazanov, *cond-mat/0506003* (2005).
- [96] S. Shapiro, *Phys. Rev. Lett.* **11**, 80 (1963).
- [97] P. Russer, *J. Appl. Phys.* **43**, 2008 (1972).
- [98] C. Vanneste, C. C. Chi, W. J. Gallagher, A. W. Kleinsasser, S. I. Raider, and R. L. Sandstrom, *J. Appl. Phys.* **64**, 242 (1988).

- [99] F. Romeo and R. De Luca, *Phys. Lett. A* **328**, 330 (2004).
- [100] K. Lehnert, N. Argaman, H. Blank, K. C. Wong, S. J. Allen, E. L. Hu, and H. Kroemer, *Phys. Rev. Lett.* **82**, 1256 (1999).
- [101] H. Sellier, C. Baraduc, F. Lefloch, and R. Calemczuk, *Phys. Rev. Lett.* **92**, 257005 (2004).
- [102] B. S. Shastry, *J. Phys. C: Solid State Phys.* **12**, L405 (1979).
- [103] R. V. Kulkarni, E. Almaas, K. D. Fisher, and D. Stroud, *Phys. Rev. B* **62**, 12119 (2000).
- [104] S. E. Korshunov, *Phys. Rev. B* **62**, 054416 (2002).
- [105] H. Hilgenkamp, Ariando, H. H. Smilde, D. H. A. Blank, G. Rijnders, H. Rogalla, J. R. Kirtley, and C. C. Tsuei, *Nature* **442**, 50 (2003).
- [106] L. N. Vu and D. J. Van Harlingen, *IEEE Trans. Appl. Supercond.* **3**, 1918 (1993).
- [107] L. N. Vu, M. S. Wistrom, and D. J. Van Harlingen, *Appl. Phys. Lett.* **63**, 1693 (1993).
- [108] B. L. T. Plourde, Ph.D. thesis, University of Illinois (2000).

# Author's Biography

Sergey Frolov was born on June 9, 1980 in the city of Zaporozhye, Ukraine. His interest in science and particularly in physics was stimulated by parents and by friends, many of whom can be described with an American word “geek”, which was unknown to Sergey at the time. In 1996 Sergey became a student of Moscow Institute of Physics and Technology. At Phystech, Sergey specialized in solid state physics in the lab of Valery Ryazanov, and earned a bachelor's degree in 2000. Same year he became a graduate student at UIUC, where he worked in the group of Dale Van Harlingen studying Superconductor-Ferromagnet-Superconductor junctions. That resulted in this PhD thesis and a number of other publications. Sergey was recognized by the John Bardeen Award from the Department of Physics at the University of Illinois, an honor that will forever warm his heart, accompanied by a hefty plaque that will forever warm the bottom of his desk drawer. In September 2005 Sergey starts as a postdoc at the University of British Columbia, where he will work with Josh Folk on spin physics in quantum dots.